الجمهورية الجزائرية الديموقراطية الشعبية
République Algérienne Démocrtaique et Populaire
وزارة التعليم العالي و البحث العلمي
Ministère de l'Enseignement Supérieur et de la Recherche Scientfiique

Université Badji Mokhtar - Annaba
Faculté des Sciences
Département de Physique

جامعة باجي مختار عنابة
كلية العلوم - قسم الفيزياء

THÈSE

Présentée en vue de l'obtention du diplôme de

DOCTORAT

DOMAINE : Sciences de la Matière
FILIÈRE : Physique
SPÉCIALITÉ : Physique Théorique

Probing High-Energy Cosmic Rays with the KM3NeT/ARCA Neutrino Telescope

par

BOUASLA Amani Besma

Jury de soutenance

TALAI Mohamed Chérif	Président	Prof.	Univ. Annaba
ATTALLAH Reda	Encadrant	Prof.	Univ. Annaba
BRUIJN Ronald	Examinateur	Prof.	Univ. Amsterdam
BOULDJEDRI Abdelhamid	Examinateur	Prof.	Univ. Batna
DJEMIL Taoufik	Examinateur	Prof.	Univ. Annaba

2025

Dedication

To my beloved parents, Abdelaziz and Moufida, for their endless love and sacrifices. To my dear brothers, Souheil and Rami, for their constant support and encouragement. And to my wonderful friends for always believing in me. This achievement is as much yours as it is mine.

Acknowledgements

I would like to express my sincere gratitude to my supervisor, Prof. Reda ATTALLAH, for guiding me through my whole academic journey, from my bachelor's and master's studies to this PhD. I am deeply thankful for the many discussions we had, for his advice when things became difficult, and for his encouragement when I doubted myself. I also appreciate the time and care he took to carefully read and correct this thesis, improving it in every possible way. This work would not have been the same without his guidance and support.

I would also like to express my heartfelt thanks to Prof. Ronald BRUIJN. His guidance, kindness, and support made this experience very special. He gave me the opportunity to work at NIKHEF and to discover what life in a research laboratory is really like. Working at NIKHEF was one of the most meaningful experiences of my PhD. It allowed me to grow as a researcher, to learn how to collaborate with others, and to understand the spirit of teamwork that drives large scientific experiments like KM3NeT. I also thank him for accepting to be a member of the jury.

I would also like to express my sincere gratitude to the members of the jury: Prof. Mohamed Chérif TALAI from the University of Annaba, President of the jury, and Prof. Abdelhamid BOULDJEDRI from the University of Batna 1 and Prof. Taoufik DJEMIL from the University of Annaba, as examiners, for kindly agreeing to evaluate this thesis. I am truly grateful for the time and care they dedicated to reviewing my work.

My warm thanks also go to Prof. Dorothea SAMTLEBEN, whose support and kindness during my visits to NIKHEF were always deeply appreciated. She was always available to listen and to give thoughtful advice. Her encouragement and help were invaluable, and I am very thankful for the time she dedicated to guiding me during this period.

Special thanks to Clara, for all the good times we shared both inside and outside the lab. Our long discussions, laughter, and shared experiences made my stay in Amsterdam so much more enjoyable. The memories we created together will always stay with me. I am also very grateful to Jihilik, Paco, Thijs, and Brian, for their help, and support

throughout this journey.

I would also like to thank my dear friends Noussa and Amina for being such strong sources of encouragement and for always supporting me, even from afar. Thank you for your patience when I kept talking about cosmic rays and data analysis even though those topics were probably not your favorite! Your friendship has been a precious part of this journey, and I am deeply grateful to have you both in my life.

Finally, and most importantly, I want to express my deepest gratitude to my beloved parents. Your endless love, sacrifices, and encouragement have made everything possible. You have always believed in me, even when I doubted myself. Your strength, wisdom, and constant support have been my greatest source of motivation. Everything I have achieved is because of your guidance and unconditional love. Thank you for teaching me the values of hard work, honesty, and perseverance.

To my brothers, Souheil and Rami, thank you for always being there for me, for your love, patience, and support at every step of my life. You have always found ways to make me smile, even during the most stressful moments. Your big sister finally made it, so no more lights left on throughout the night!

Abstract

Cosmic rays are charged particles, primarily protons and atomic nuclei, that strike the Earth from all directions with very high energies. When they enter the atmosphere, they interact with air atoms and generate cascades of secondary particles known as extensive air showers. Among these, muons play a particularly important role: they carry information about the primary cosmic ray and are able to penetrate deep underground or underwater, reaching detectors such as the KM3NeT/ARCA neutrino telescope. Located in the Mediterranean Sea, ARCA is a very large-volume neutrino detector capable of probing cosmic rays in the TeV-PeV energy range through the detection of atmospheric muons, which constitute the majority of events it records. The goal of this thesis is to study high-energy cosmic rays using atmospheric muons observed with KM3NeT/ARCA, with a primary focus on investigating the anisotropy in their arrival directions in the TeV-PeV range.

Keywords: Cosmic rays – Anisotropy – KM3NeT – ARCA

ملخـــص

الأشعة الكونية هي جسيمات مشحونة، تتكوّن أساسًا من البروتونات والنوى الذرية، تصل إلى الأرض من جميع الاتجاهات بطاقة فائقة الارتفاع. وعند دخولها الغلاف الجوي، تتفاعل مع ذرات الهواء وتُنتج شلالات من الجسيمات الثانوية تُعرف باسم "الزخات الجوية الممتدة". ويُعد الميون مكوّنًا رئيسيًا في هذه الزخات، إذ يحتفظ بمعلومات حول الأشعة الكونية الأولية، كما يتمكّن من النفاذ عميقًا تحت سطح الأرض أو في أعماق البحار، ليصل إلى كواشف مثل مرصد النيوترينو KM3NeT/ARCA . يقع كاشف ARCA في البحر الأبيض المتوسط، وهو مرصد نيوترينو ضخم قادر على استكشاف مجال الطاقات الممتد من تيرا إلكترون فولت (TeV) إلى بيتا إلكترون فولت (PeV) ، من خلال رصد الميونات الجوية التي تُشكّل الغالبية العظمى من الأحداث المسجَّلة. وتهدف هذه الأطروحة إلى دراسة الأشعة الكونية عالية الطاقة اعتمادًا على الميونات الجوية المرصودة بواسطة KM3NeT/ARCA ، مع تركيز خاص على اللاتناحي في توزيعات وصولها ضمن مجال الطاقات TeV-PeV .

الكلمـات المفتاحيـة : الأشعة الكونيـة - لاتنـاحي - ARCA - KM3NeT

Résumé

Les rayons cosmiques sont des particules chargées, principalement des protons et des noyaux atomiques, qui atteignent la Terre depuis toutes les directions avec des énergies extrêmement élevées. En traversant l'atmosphère, ils interagissent avec les atomes de l'air et produisent des cascades de particules secondaires, appelées gerbes atmosphériques étendues. Les muons issus de ces gerbes constituent une composante essentielle : ils conservent les informations sur les rayons cosmiques primaires et peuvent pénétrer profondément sous terre ou sous l'eau, jusqu'à des détecteurs comme le télescope à neutrinos KM3NeT/ARCA. Installé en Méditerranée, ARCA est un détecteur de très grand volume capable d'explorer la gamme d'énergie TeV-PeV des rayons cosmiques grâce à la détection des muons atmosphériques, qui représentent la majorité des événements enregistrés. Cette thèse a pour objectif l'étude des rayons cosmiques de haute énergie à partir des muons atmosphériques observés par KM3NeT/ARCA, avec un accent particulier sur l'anisotropie de leurs directions d'arrivée dans la gamme TeV-PeV.

Mots clés : Rayons cosmiques – Anisotropie – KM3NeT – ARCA

Contents

List of Figures

Introduction

Cosmic rays are charged particles, mainly protons and heavier nuclei that constantly bombard the Earth with extremely high energies. Since their first discovery, they have unlocked the door to a new discipline in physics, the astroparticle physics, and remains until now the heart of some of its biggest questions. Their origin is still not fully understood even after more than a century of research. Their energy spectrum spans across many orders of magnitude and shows distinctive features such as, the so called "knee" and "ankle" which give us a hint about their sources and their propagation in the interstellar medium.

One way to explore the origin on cosmic rays is by studying the anisotropy in their arrival direction. Although cosmic rays reach the Earth isotropically, small deviation at the level of 10^{-3} to 10^{-4} have been observed by several ground based experiments in both the Northern and Southern hemispheres. These small patters provide key information about how cosmic ray diffuse through magnetic fields and the presence of nearby sources.

This is where KM3NeT/ARCA comes in, to provide complementary measurements of cosmic ray anisotropy in the TeV-PeV range. ARCA is a neutrino telescope located deeep in the Mediterranean sea designed to observe high-energy cosmic neutrinos. At the same time, the detector constantly records atmospheric muons coming from the interaction of cosmic rays with the atmosphere. These muons are usually considered as a background with respect to the detector, nevertheless they can be used to probe high energy cosmic rays.

The main goal of this thesis is to use the atmospheric muons detected by ARCA to probe high-energy cosmic rays with a focus the reconstruction and analysis of cosmic ray anisotropy. The results presented here shows how KM3NeT can contribute to cosmic ray physics in addition to its primary mission of neutrinos astronomy.

The first chapter of this thesis gives an overview of cosmic rays, their discovery, possible sources and how they propagate through space. Chapter 2 focuses on cosmic ray anisotropy and summarises key results from previous experiments. Chapter 3 introduces

the KM3NeT detector and its design. Chapter 4 explains the analysis software used in this work and the processing chain in KM3NeT. Finally, chapter 5 presents the atmospheric muons properties at sea level as well as the first measurement of cosmic ray anisotropy with the KM3NeT/ARCA detector.

Chapter 1

Cosmic rays

Since the discovery of cosmic rays (CRs) in the 20th century, they have been a key probe for understanding high energy phenomena in the universe. CRs consist mainly of protons and heavier nuclei that strike the Earth constantly from outer space. Their study include a wide range of energies, mass compositions and acceleration scenarios from extreme astrophysical environment. After their acceleration, these particles propagate through the interstellar medium and interact with magnetic fields before reaching our planet. In this chapter, an overview of cosmic rays, their potential sources, and their propagation through space is presented.

1.1 Historical background

The discovery of cosmic rays was made in 1912 by Austrian physicist Victor Hess [1] during a hot-air balloon ascent equipped with electroscopes (Fig. 1.1). Observing ionizing flux increasing regularly with altitude, he deduced the radiation's cosmic origin, challenging the prevailing belief in terrestrial radioactivity. Hess received the Nobel Prize in Physics in 1936. The American physicist Robert Millikan coined the term "cosmic rays" in 1925. In 1938, the French scientists Pierre Auger and Roland Maze identified temporal coincidences in cosmic rays, naming the phenomenon "air shower" [2]. Using Geiger-Müller counters spaced 300 m apart, they recorded coincidences revealing secondary particles initiated by atmospheric interactions. The exploration of high-energy cosmic ray physics gained momentum in 1963 when the American scientist John Linsley observed extensive air showers with an unprecedented energy of about 10^{20} eV, suggesting an extragalactic source. Subsequent experiments, such as SUGAR in Australia, AGASA in Japan, and the Pierre Auger Observatory in Argentina, investigated this exceptional radiation.

Fig. 1.1: Victor Hess setting off on his balloon flights. Taken from [3].

In 1965, Penzias and Wilson discovered the cosmic microwave background (CMB), leading Greisen, Zatsepin, and Kuz'min (GZK) researchers to explore its impact on cosmic rays. By 1966, they revealed the GZK effect, indicating that cosmic rays, above 4×10^{19} eV for protons, interact with the CMB photons, resulting in significant energy loss [4], [5].

In 1967, Greisen proposed the air fluorescence technique to detect large air showers from cosmic rays with ultra high energies [4]. This method uses the atmosphere as a calorimeter, detecting fluorescence emitted as cosmic rays interact with air atoms. The first detection occurred at Volcano Ranch in New Mexico by physicists from the University of Utah [6]. Subsequently, experiments like Fly's Eye [7], Pierre Auger Observatory [8], and Telescope array [9] continued using this technique, combining air fluorescence and ground-based detection methods to cover the skies of both the southern and northern hemispheres.

1.2 Primary energy spectrum

Fig. 1.2 illustrates the primary energy spectrum of high-energy cosmic rays, showcasing how particle rates change with energy. The rate decreases rapidly with energy, following a power-law:

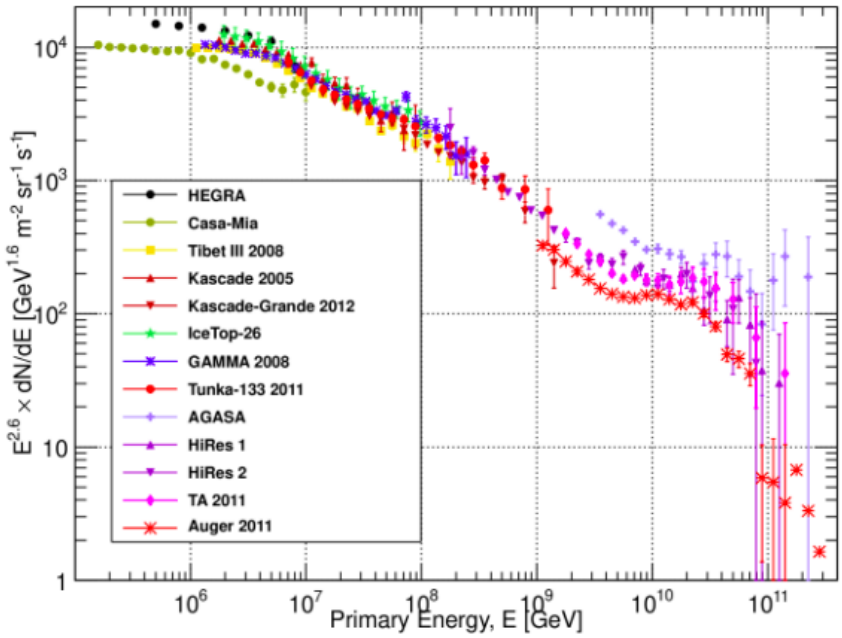

Fig. 1.2: All particle energy spectrum. Taken from [10].

$$\frac{dN}{dE} \sim E^{-\gamma} \tag{1.1}$$

where γ is the spectral index. Breakpoints in the slope indicate transitions between different cosmic ray behaviors. Cosmic rays with energies below a few GeV are affected by solar winds, leading to their expulsion from the solar system.

- Around 5×10^{15} eV, a breakpoint known as the "knee" occurs, marking the transition to cosmic rays believed to be accelerated by supernovae within our galaxy. The first knee corresponds to particles with the lowest charge.
- At 10^{17} eV, a shift from $\gamma = 3$ to $\gamma = 3.3$ represents the "second knee". Between the knees, the spectrum structures appear in ascending order of electric charge, with the second knee corresponding to cosmic rays with the highest electric charge, specifically iron nuclei.
- Around 5×10^{18} eV, a shift from $\gamma = 3.3$ to $\gamma = 2.7$, called the "ankle", represents the transition from Galactic origin to extragalactic origin. This transition suggests a change in the cosmic-ray source beyond our galaxy. Indeed, at such energies, cosmic rays cannot be confined within our galaxy as their Larmor radii (RL) would exceed the width of the Galactic disk. For a particle with momentum p and charge Ze gyrating in a magnetic field B, the RL is given by:

$$R_L = \frac{p}{ZeB} \times \left(\frac{1.8\,\text{Mpc}}{Z}\right) \times \left(\frac{1\,\text{EeV}}{E}\right) \times \left(\frac{B}{1\,\text{nG}}\right)^{-1}$$

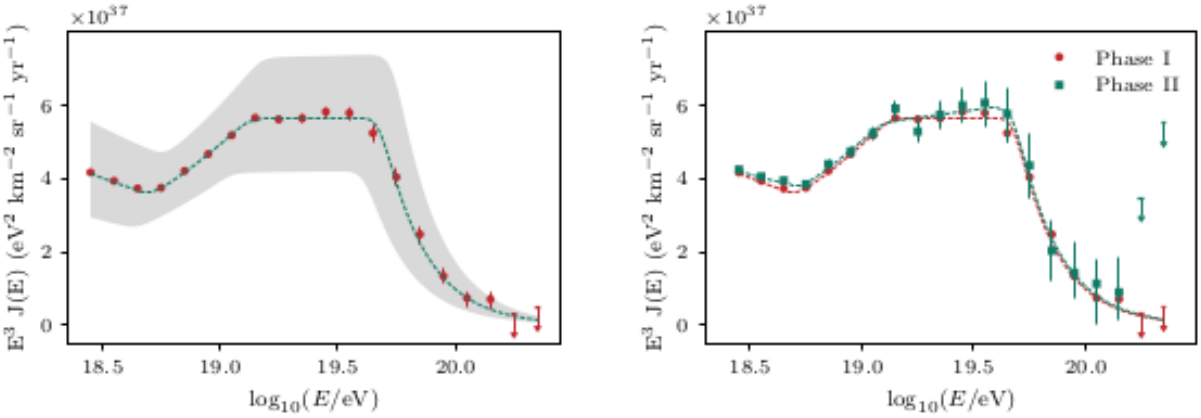

Fig. 1.3: Energy spectra of cosmic rays measured by the Pierre Auger Observatory. **Left**: Combined spectrum using events with zenith angles up to80°covering declinations from the south celestial pole to +44.8° with systematic flux uncertainties indicated by the shaded band. **Right**: Preliminary spectrum for zenith angles up to 60° from Phase II of Auger, compared with Phase I results. Taken from [11].

For example, for a cosmic proton ($Z = 1$) with energy $E = 10^{18}$ eV propagating in an intergalactic magnetic field $B \approx 1$ nG, RL is calculated to be 1.08 Mpc, significantly larger than the estimated diameter of the Milky Way, which is 20 kpc (equivalent to 0.02 Mpc).

- At the high-energy end of the spectrum, around 4×10^{20} eV, the uncertainty bars associated with measurement points in this region reveal a conspicuous lack of experimental data (Fig. 1.2). The observed cutoff aligns with the GZK cutoff, but it cannot be ruled out that it might instead signify that the sources of cosmic rays have reached their limit in terms of acceleration power.

The Pierre Auger Observatory found a new feature in the ultra-high-energy cosmic ray (UHECR) spectrum: the "instep", at about 13 EeV (Fig. 1.3). This spectral feature, which lies between the well-known ankle (about 5.1 EeV) and the flux suppression (about 48 EeV), shows a small but statistically significant change in the spectral slope. After 19 years of data and more than 104,000 km^2 sr yr of exposure, the instep has now been seen with a significance greater than 5σ, confirming that it is a real structure in the UHECR energy spectrum. After the ankle ($\gamma_2 = 2.51$), the spectral index gets harder and steeper again after the instep ($\gamma_3 = 2.99$). This could mean that the composition, the source class, or the propagation regime of cosmic rays changes. This finding gives us a new observational limit for theoretical models of how cosmic rays are made and how they speed up, and it shows how important it is to improve our understanding of how UHECRs are made and move in space outside of our galaxy.

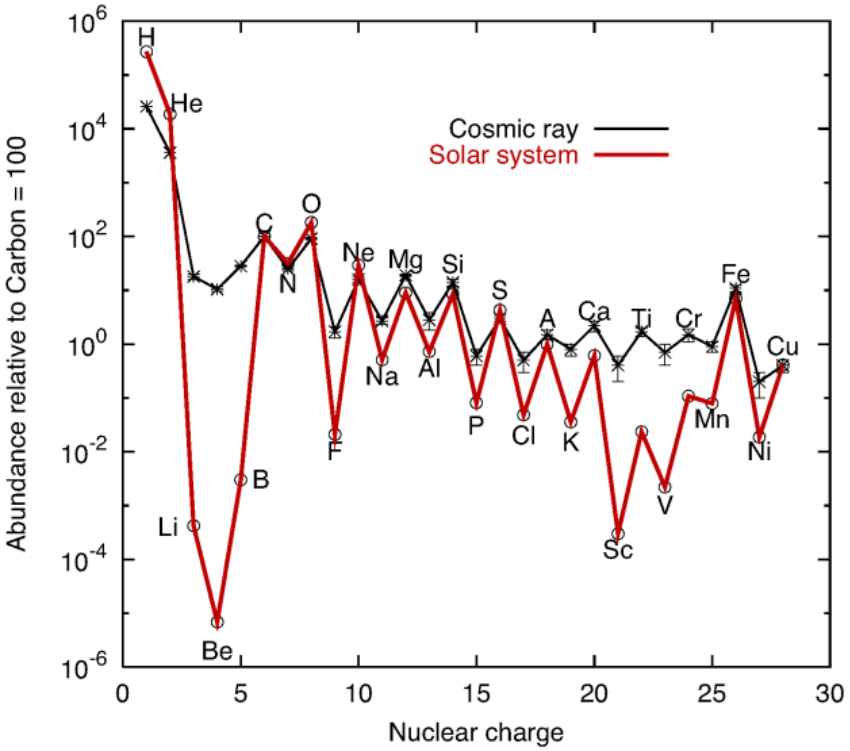

Fig. 1.4: Nuclear abundance of cosmic rays compared to the solar system. Taken from reference [12].

1.3 Mass composition

The experimental measurement of the primary cosmic ray composition is feasible only for energies below 10^{14} eV, using detectors on stratospheric balloons or satellites. Fig. 1.4 compares the relative abundance of cosmic rays with the elemental abundance in the solar system. The primary cosmic rays share many characteristics with the solar system composition, but there are two notable differences.

Indeed, atomic nuclei with atomic number $Z = 2$–4 (Li, Be, B) and the iron sub-group (Sc, Ti, V, Cr, and Mn) are more abundant in cosmic rays than in the solar system. The prevailing explanation is that cosmic rays initially have the same chemical composition as the solar matter. However, during their journey through space, interactions with interstellar gases and dust particles lead to spallation, causing heavy nuclei to break into lighter ones. The overabundance of the (Li, Be, B) group is attributed to carbon (C) and oxygen (O) spallation, while iron (Fe) contributes to the iron sub-group.

For most cosmic rays, the average amount of matter (X) traversed between production and observation at Earth is 5 to 10 g/cm^2. This estimate is derived from the spallation cross-section measured by particle accelerators. Additionally, the matter density (ρ_N) of the Galactic disk is estimated at 1 proton/cm^3. With these data, the average free path

(l) of cosmic rays is estimated as:

$$l = \frac{X}{m_p \rho_N} = 3 \times 10^{24}\,\mathrm{cm} \approx 1\,\mathrm{Mpc} \tag{1.2}$$

where $m_p = 1.67 \times 10^{-24}$ g is the proton mass. Considering the Galactic plane diameter of approximately 30 kpc, it suggests that low-energy cosmic rays propagate in a highly tortuous path through our galaxy. The resulting lifetime for cosmic rays is:

$$\tau = \frac{l}{v} \approx 3 \times 10^6 \text{ years} \tag{1.3}$$

This implies that cosmic ray nuclei spend a considerable time diffusing in the Galactic halo before escaping into the intergalactic space.

1.4 Extensive air showers

When a cosmic particle of very high energy enters the Earth's atmosphere, it interacts with the atomic nuclei in the air, generating other particles known as secondary cosmic rays. Depending on their energy, these secondary particles either interact further with the air or undergo decay, and the newly produced particles follow the same fate. This process repeats throughout the atmosphere until the particles reach the ground, leading to the formation of what is commonly referred to as air showers (Fig. 1.5).

The interaction of the primary particle mainly produces pions $\pi^{\pm}, \pi^0$, around 10% of kaons ($K^{\pm}, K^0$), and nuclear fragments. They form the hadronic component of the air shower. Initially, the charged pions ($\pi^{\pm}$) and charged kaons ($K^{\pm}$) have high energy, making them more prone to interacting with the medium and causing nuclear reactions. However, as the shower develops, their energy decreases, and they eventually decay:

$$\pi^{\pm} \rightarrow \mu^{\pm} + \nu_{\mu}(\bar{\nu}_{\mu})$$
$$K^{\pm} \rightarrow \mu^{\pm} + \nu_{\mu}(\bar{\nu}_{\mu})$$

These muons constitute the muonic component of the shower. As for the neutral pion (π^0), due to its extremely short lifetime ($\sim 10^{-16}$ s), it mainly decays into a pair of photons. These photons generate electron-positron pairs (e^-, e^+), which, in turn, create photons through Bremsstrahlung. These successive creations give rise to the so-called electromagnetic component of the shower.

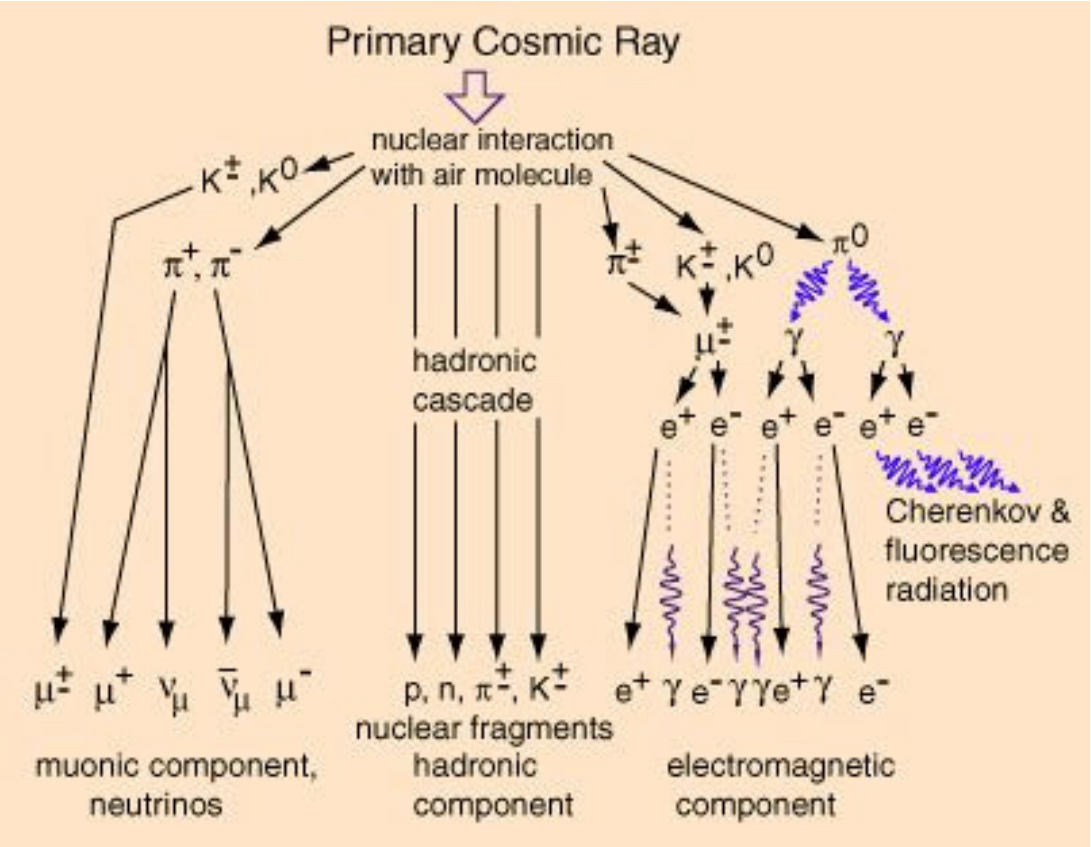

Fig. 1.5: Schematic illustration of a cosmic-ray air shower. Taken from [13].

At sea level, cosmic rays consist of approximately 80% muons ($\mu^{\pm}$), 20% electrons ($e^{\pm}$), and a small percentage of hadrons. This composition emphasizes the predominant role of muons in the cosmic ray flux reaching the Earth's surface. Understanding the behavior and characteristics of muons at sea level is essential not only for deciphering the composition of cosmic rays but also for unraveling the complexities of extensive air showers, where muons play a central role in shower development and propagation. Therefore, by examining muon properties at sea level, we gain invaluable insights into the dynamics of cosmic ray interactions and their manifestations in atmospheric phenomena (see section 4.1).

1.5 Acceleration mechanism

Cosmic ray particles are believed to undergo acceleration through two mechanisms. The first involves direct acceleration by significant electric fields associated with the rapid rotation of objects or active galactic nuclei. However, this is not favored due to high-energy density and theoretical limitations. The second, proposed by Fermi in 1949, relies on stochastic acceleration of charged particles, with two variants: first-order and second-order acceleration.

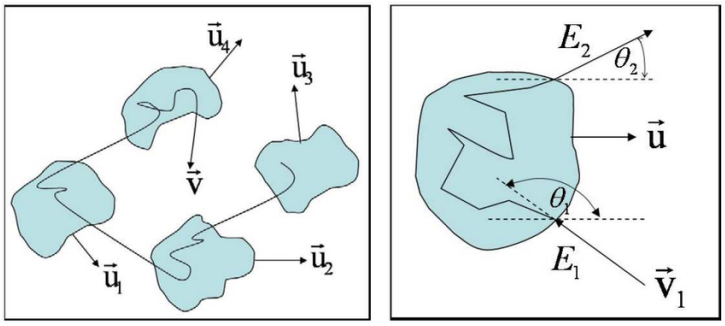

Fig. 1.6: Illustartion of the second-order Fermi acceleration. Taken from [14].

1.5.1 Second-order Fermi acceleration

The basic idea is that a charged particle can be accelerated when scattered by a moving magnetized gas cloud (magnetic mirror) [15]. The probability of a head-on collision is higher than that of a rearward collision. In other words, particles gain energy, resulting in acceleration. Let E_i be the energy of an incident charged particle entering a magnetized cloud with momentum p_i and an angle of incidence θ_i with the cloud's direction of motion (Fig. 1.6). After several scatterings, the particle exits the magnetized cloud with energy E_f, momentum p_f, and angle θ_f. By applying Lorentz transformations between the laboratory frame (R) and the cloud frame (R'), we have:

$$E_0 = \gamma E_i(1 - \beta \cos\theta_i) \tag{1.4}$$

$$E_f = \gamma E_0(1 + \beta \cos\theta_f) = \gamma^2 E_i(1 - \beta \cos\theta_i)(1 + \beta \cos\theta_f) \tag{1.5}$$

with $\beta = \mathrm{V/c}$, where V is the cloud's speed, and γ is the Lorentz factor. In the cloud's frame, we have an elastic collision, so $E_{0i} = E_{0f}$. The relative energy gain is:

$$\xi = \frac{\Delta E}{E} = \gamma \left(\frac{1 + \beta^2 \cos\theta_i \cos\theta_f - \beta \cos\theta_i + \beta \cos\theta_f}{2} - 1 \right) \tag{1.6}$$

Moreover, $\langle \cos\theta_f \rangle = 0$. As the particle experiences repeated scatterings within the cloud, its exit direction becomes random. The average value of $\cos\theta_i$ depends on the relative velocity between the cloud and the particle, namely $v - V\cos\theta_i$. We find:

$$\langle \cos\theta_i \rangle = -\frac{\beta}{3} \tag{1.7}$$

This yields $\langle \Delta E/E \rangle \sim 4\beta^2/3$. Here, the overall energy gain is not significant, especially in the classical limit (non-relativistic) where $\beta \ll 1$.

1.5.2 First-order Fermi acceleration

The second-order Fermi acceleration process is very slow, which is a significant drawback. Therefore, a more efficient mechanism was proposed, based on the idea of diffusive acceleration at a shock wave generated, for example, by a supernova remnant (SNR), a gamma-ray burst (GRB), etc [14]. A particle that crosses the shock front from upstream to downstream and back again (i.e., between the shocked and unshocked regions) gains energy. This energy increases with every round trip due to magnetic reflection effects.

Let V_s be the shock speed and V_p the velocity of the charged particle. One can show that the average cosine of the entry angle over upstream crossings is

$$\langle \cos \theta_{\mathrm{i}} \rangle = -\frac{2}{3} \tag{1.8}$$

and that the average cosine of the exit angle over downstream crossings is

$$\langle \cos \theta_{\mathrm{f}} \rangle = +\frac{2}{3} \tag{1.9}$$

This assumes that the angular distributions before and after crossing the shock are isotropic. From these, it follows that

$$\frac{\Delta E}{E} \sim \frac{4}{3}\,\beta \tag{1.10}$$

where $\beta = V_s/c$. Note that the energy gain is proportional to β. If E_0 is the injected energy of the particle, then after n shock cycles:

$$E = E_0 \left(1 + \frac{4}{3}\beta\right)^n \tag{1.11}$$

Thus,

$$n = \frac{\ln(E/E_0)}{\ln\left(1 + \frac{4}{3}\beta\right)} \tag{1.12}$$

Let P_{escape} be the probability that a particle escapes the acceleration region during one cycle. The probability that it remains is $(1 - P_{\mathrm{escape}})$, and after n cycles it's $(1 - P_{\mathrm{escape}})^n$. Hence the number of particles remaining is:

$$N = N_0\,(1 - P_{\mathrm{escape}})^n \tag{1.13}$$

Substituting n from (1.11), we get:

$$N = N_0 \left(\frac{E}{E_0}\right)^{\ln(1-P_{\mathrm{escape}})/\ln\left(1+\frac{4}{3}\beta\right)} \tag{1.14}$$

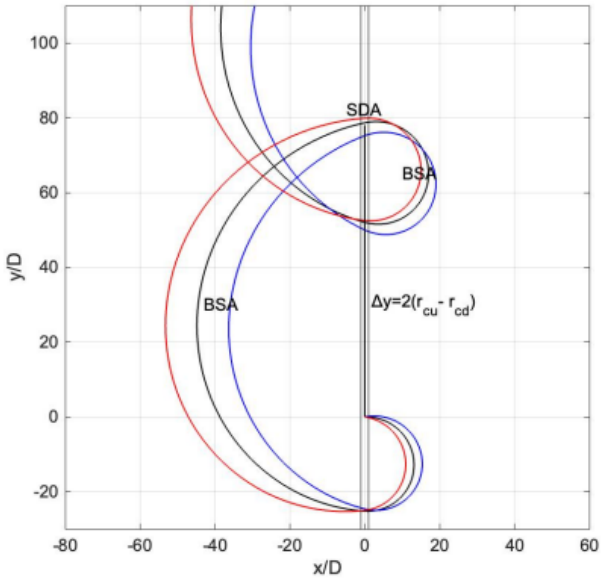

Fig. 1.7: Ballistic surfing acceleration of three ions injected into a perpendicular shock at different incident angles. Taken from [16].

This corresponds to a power-law energy spectrum. In the case of a non-relativistic shock propagating through a monoatomic gas with a compression ratio of $r = 4$, the spectral index γ (or p) is approximately 2. For a relativistic shock, γ is typically in the range 2.0 to 2.3. For ultra-relativistic shocks, the index is usually between 2.2 and 2.3, depending on the specific model you consider.

1.5.3 Ballistic surfing acceleration

Another acceleration mechanism is introduced as an alternative to the traditional first-order Fermi acceleration. The model referred to as Ballistic Surfing Acceleration (BSA) suggests that particles acquire energy beyond the shock front, by interacting with the upstream convection electric field, instead of through multiple shock crossings (Fig. 1.7). In contrast to the Fermi model, which associates the spectral index with density compression, BSA indicates that it is actually determined by magnetic field compression. The analysis indicates a projected spectral index of –2.5 beneath the "knee" and –3 above it, which aligns closely with observed data. The knee's position can be understood as the energy level where a particle's gyroradius matches the dimensions of a supernova shock. The estimated time for the necessary acceleration is approximately 300 years, indicating that fewer shock encounters are needed. This model underscores that the observed alignment between Fermi/DSA predictions and actual observations is merely coincidental, as BSA provides a more coherent and physically consistent interpretation of the cosmic-ray spectrum [16].

1.6 Potential sources of cosmic rays

1.6.1 Galactic sources

- **Supernova Remnants (SRNs)**
  A supernova remnant is the expanding shell of gaz and plasma left behind after the core collapse of a massive star. These remnants are among the most energetic astrophysical objects in the Galaxy, with shock fronts expanding at several thousand km/s and compressing the surrounding interstellar medium. Because of their strong shocks and large spatial extent, SRNs are considered the primary accelerators of CRs up to at least the knee region [17]. They can not accelerate cosmic rays to energies higher than the knee energy region due to the size of the shock front and the strength of the magnetic field.

- **Pulsars**
  Pulsars are neutron stars that rotate rapidly and emit beams of electromagnetic radiations including radio waves due to their strong magnetic field. Specifically, pulsars generate strong winds of positrons and electrons that end in shocks, creating pulsar wind nebulae (PWNe), which are places where additional acceleration takes place. These systems may account for observed excesses in CR positrons and are thought to be significant contributors to the Galactic CR population, particularly at high energies [18].

1.6.2 Extragalactic sources

- **Active Galactic Nuclei (AGNs)**
  The most luminous objects in the universe are Active Galactic Nuclei (AGNs), which have power outputs ranging from 10^{41} to erg s^{-1}. There are primarily two types of AGN: radio-weak sources and radio-loud sources. Some examples of radio-weak sources include radio-quiet quasars, Seyfert galaxies, and LINERs; these objects do not emit much radio energy and do not release relativistic jets. Blazars, radio-loud quasars, and Fanaroff-Riley radio galaxies are examples of radio-loud sources. The latter are further broken down into four distinct morphological kinds, two of which being the famous FR I and FR II. The universe's largest dissipative (non-thermal) sources are FR II galaxies. The lobes of these galaxies contain regions of extremely high synchrotron radiation, called hotspots, which form relativistic particles and turbulent magnetic fields, transforming most of the kinetic energy carried by the jets emanating from the central engine, which consists of a supermassive black hole

and its accretion disc. Acceleration of particles in these regions is mostly due to first-order Fermi processes. Radio-galaxies like as Centaurus A, Hercules A, Cygnus A, and 3C 75 are famous examples.

- **Gamma-Ray Bursts (GRBs)**
  Gamma-ray bursts (GRBs) are short, intense flashes of high-energy radiation produced by powerful explosions in distant galaxies, and are regarded as the most luminous electromagnetic events in the universe. Various theoretical models place the acceleration site at either internal or external shocks, as described in the fireball model [19], [20]. Two main classes of GRBs are distinguished: (i) long GRBs, typically lasting more than 2 s, which are thought to be associated with certain types of supernova explosions; and (ii) short GRBs, with durations shorter than 2 s, which are believed to originate from the final stages of binary systems composed of compact objects.

1.6.3 Hillas criterion

The Hillas criteria is defined as the ratio of an accelerated particle's Larmor radius (r_L) to the size (L) of the astrophysical source [21]. A logical condition is that $r_L \leq L$ for acceleration to occur. Recall that:

$$r_L = \frac{E}{ZeB} \tag{1.15}$$

where B is the magnetic field present at the astrophysical site and E is the energy that the particle can acquire in the source (confinement energy). According to the Hillas criterion, the maximum energy reachable is:

$$\mathrm{E} \leq \mathrm{E}_{\max} = \Gamma_s \beta Z e L \tag{1.16}$$

where Γ_s represents the Lorentz factor of the site and Z the charge number of the particle. According to the Hillas criterion, one can select among astrophysical objects those capable of accelerating cosmic rays up to ultra-high energies (UHE), by plotting their sizes as a function of their magnetic fields. This results in what is known as the Hillas diagram (Fig. 1.8). Sources capable of accelerating protons up to 10^{20} eV are located above the dotted line. These include, for example, gamma-ray bursts (GRBs), some of active galactic nuclei (AGN), neutron stars, etc. Sites capable of accelerating protons up to 10^{21} eV are located above the blue line, as shown in the figure. The green line is for iron nuclei, since $Z = 26$, the product $B \times L$ is smaller than for protons at the same energy. This means

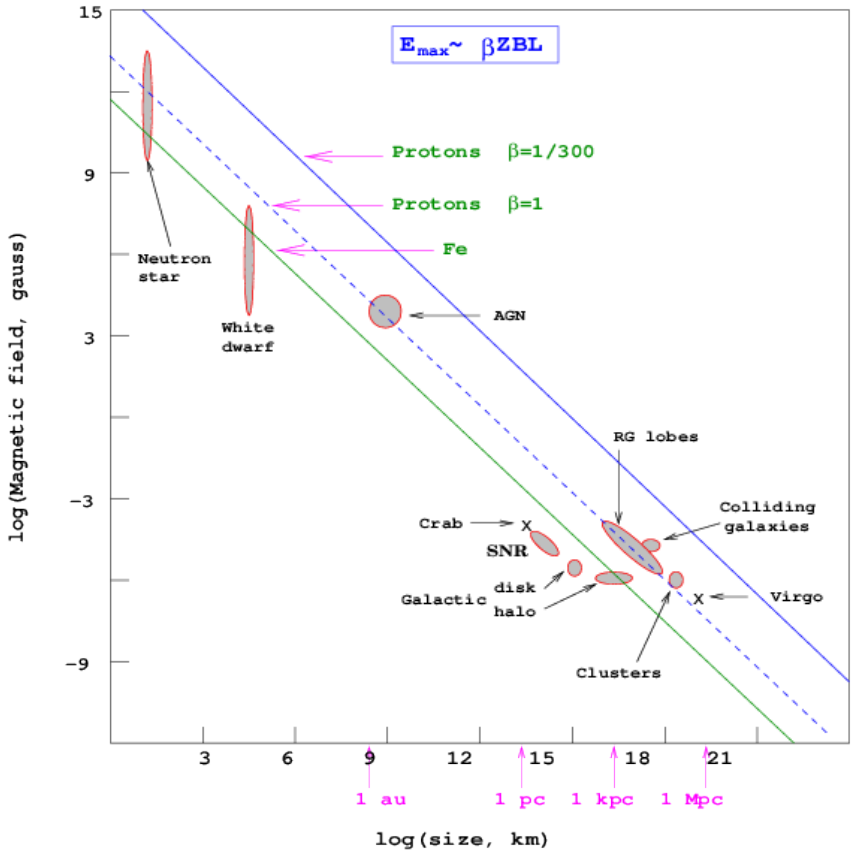

Fig. 1.8: Hillas diagram. Taken from [21]

sources below the proton line but above the iron line could still accelerate iron to 10^{20}eV even if they can't accelerate protons that high. It should be noted that energy losses are not taken into account in this diagram.

1.7 Propagation in the Galaxy

Our galaxy, the Milky Way, exhibits a flattened disc shape with a radius of 15 kpc, and a thickness of 300 pc (Fig. 1.9). One of the spiral arms of the Galaxy contains the solar system. The latter is located approximately 8 kpc from the Galactic center. Observations of Zeeman splitting, starlight polarization and Faraday rotation reveal the presence of a large-scale magnetic field throughout the galaxy. Precisely, the disc and halo are permeated by a coherent magnetic field of order $B_0 \approx 3$–$5\,\mu$G in the plane, decreasing to $\sim 1\,\mu$G at heights of several kiloparsecs above the mid-plane. Upon this regular component, a turbulent magnetic field component is superimposed with nearly the same strength, but with a characteristic scale of 10–100 pc. A magnetohydrodynamic fluid (MHD) is formed by the ionized gas and the magnetic field. Alfven waves can propagate through that fluid and since the streaming of cosmic rays particles can generate these waves, the latter can act as scattering sources for cosmic rays.

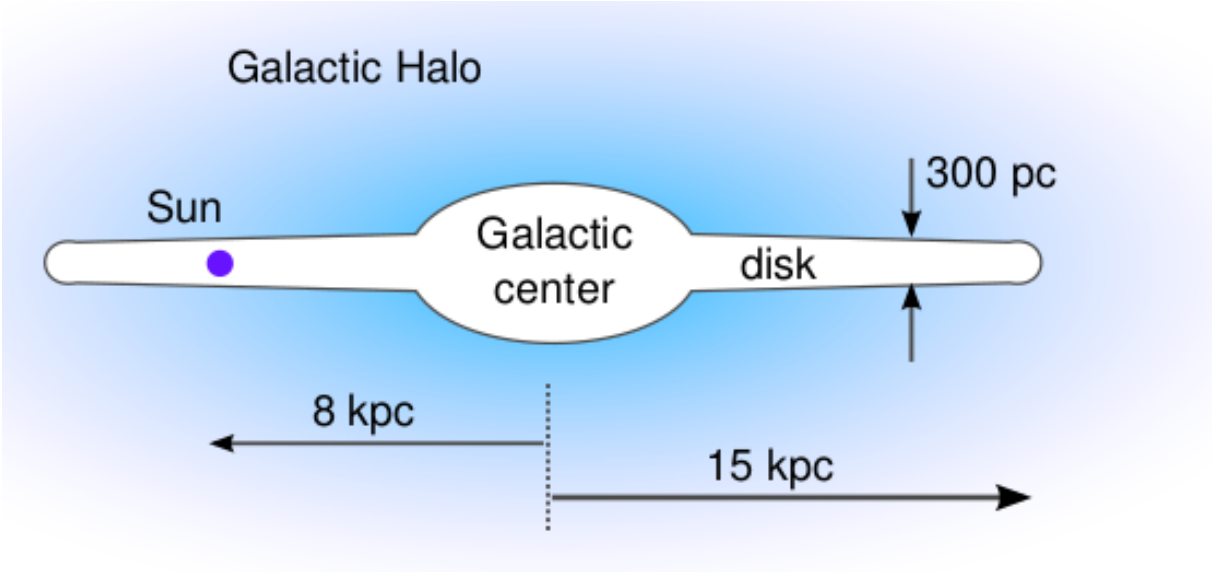

Fig. 1.9: Schematic view of the Milky Way Galaxy. Taken from [22].

The current knowledge of the cosmic ray propagation through the galaxy relies on their chemical abundance observed on Earth. With the use of the spallation cross section, one can find an estimate of the interstellar matter traversed by the primary cosmic ray. More precisely, by measuring the boron to carbon ratio (B/C). On average, cosmic rays in the GeV energy range cross 5–10 g/cm^2 of matter. However, the amount of matter along the Galaxy plane is about 10^{-3} g/cm^2. Thus, the particles are trapped by the Galactic magnetic field leading to a confinement time of several millions of years. As a result, Galactic cosmic rays arrive isotropically to Earth (see the next chapter for more details). At higher energies, cosmic rays produce fewer secondaries before arriving (the B/C ratio decreases). This implies that they escape the Galaxy faster because their high rigidity makes them harder to trap with magnetic fields (shorter confinement times) and propagation and acceleration happen in different places (if acceleration and propagation happened in the same site, the B/C ratio wouldn't depend on energy). In order to model the transport of cosmic-ray particles throughout the inter stellar medium (ISM), several propagation models have been postulated.

1.7.1 Leaky-box model

The leaky-box model is one of the early models that explains the particle propagation in the magnetic field but considered, nowadays, outdated. This model treats the Galaxy as a homogeneous reservoir bounded by an absorbing three dimensional wall. Cosmic rays are injected at a rate $Q(E,t)$ and escape with a timescale $\tau_{\text{esc}}(E) \propto E^{-\delta}$. The particles are assumed to be instantaneously and uniformly mixed within the volume and are lost only by escape through the boundary, by spallation, or by radioactive decay. The leaky-box

transport equation for species i can therefore be written as:

$$\frac{\partial N_i(E,t)}{\partial t} = Q_i(E,t) - \frac{N_i(E,t)}{\tau_{\rm esc}(E)} - \frac{\beta c \rho}{\lambda_i(E)} N_i(E,t) - \frac{N_i(E,t)}{\gamma \tau_i} + \sum_{k>i} \beta c \rho \, \sigma_{i \leftarrow k}(E) \, N_k(E,t) \tag{1.17}$$

where $N(E,t)$ represents the differential number density, λ_i the mean free path length, $\tau_{\rm esc}(E)$ the energy dependent escape time, $\gamma\tau_i$ the Lorentz-dilated lifetime for unstable nuclei, ρ the ISM mass density, βc the particle speed, and $\sigma_{i \leftarrow k}$ the spallation cross section for production of i from a heavier parent k. Neglecting secondary production and decay for a stable primary gives the steady-state density:

$$N(E) = Q(E) \, \tau_{\rm esc}(E), \tag{1.18}$$

The escape time $\tau_{\rm esc} \propto R^{-\delta}$ is often expressed in terms of the escape grammage, $\lambda_{\rm esc} = \rho\beta c\tau_{\rm esc}$ (amount of matter the particle passes through before escaping). For a simple analytic connection between the source spectrum and the observed spectrum at Earth $\delta \propto 0.6$ [23].

1.7.2 Diffusion model

The diffusion model is one of the most common ways to describe how cosmic rays move through the Galaxy. In this model, CRs scatter repeatedly on irregularities in the Galactic magnetic field performing a random walk in space. This process can be represented as spatial diffusion, with a mean free path defined by the magnitude and intensity of magnetic turbulence. In contrast to the leaky-box model, which assumes a perfectly mixed reservoir, the diffusion model accounts for spatial variations in the CR density, which allows the modeling of gradients between the Galactic disk and halo and along the radial direction. The steady-state transport equation for the simplest isotropic diffusion model is

$$\nabla \cdot D(E) \nabla N(E,\vec{r}) + Q(E,\vec{r}) - \frac{N(E,\vec{r})}{\tau_{\rm esc}(E)} = 0 \tag{1.19}$$

where $Q(E, \vec{r})$ is the source term, $N(E, \vec{r})$ is the differential CR density and $D(E) = D_0(E/E_0)^\delta$ is the diffusion coefficient, with $\delta \simeq 0.3$–0.6 depending on the turbulence spectrum.

At energies above a few GeV/nucleon, the diffusion model explains effectively the power

law dependence of secondary to primary ratios such as B/C observed on Earth. Moreover, the model naturally incorporates spatial gradients, allowing consistency checks with gamma-ray emissivity profiles. However, the simplest version of the diffusion model neglects convection, energy losses, and reacceleration, which limits its accuracy at low energies and in regions with strong Galactic winds [24].

1.7.3 Diffusion-convection model

In addition to the scattering induced diffusion, CRs can be transported by convection, i.e by large scale Galactic winds. The diffusion-convection model extends the basic diffusion equation by adding a term representing this bulk motion. The steady-state equation becomes

$$\nabla \cdot [D(E)\,\nabla N] - \nabla \cdot \left[\vec{V}_c\, N\right] + Q(E,\vec{r}) - \frac{N}{\tau_{\rm esc}} = 0 \tag{1.20}$$

where $\vec{V}_c$ is the convection velocity which is directed perpendicular to the Galactic disk and increasing with height: $\vec{V}_c = \pm V_0\,\vec{z}$. This term removes CRs more efficiently at low energies, where diffusion is slow, thereby affecting the spectral shape and secondary to primary ratios.

Physically, convection reduces the amount of spallation and shortens the residence time of CRs by sweeping them into the halo from the disc. Consequently, radioactive isotope abundances like ^{10}Be can be decreased, and B/C ratios are typically lower at low energies. Because of this, the model can be used to constrain the wind speed and the halo size from observational data. Even though the diffusion-convection model takes into account Galactic outflows, it still has trouble reproducing all of the observed CR data, especially the low-energy flattening of B/C, unless other processes like reacceleration are taken into account [25].

1.7.4 Diffusion-reacceleration model

According to this model, CRs are accelerated stochastically (second-order Fermi acceleration). Here, CRs gain or lose momentum through the interactions with moving magnetic irregularities such as Alfvén waves in the turbulent ISM. The steady state equation (neglecting strong convection) is then given by:

$$\frac{\partial}{\partial p}\left[p^2 D_{pp}(p)\frac{\partial}{\partial p}\frac{N}{p^2}\right] + Q(E,r) - \frac{N}{\tau_{\rm esc}} = 0 \tag{1.21}$$

where $D_x(E)$ represents the spatial diffusion coefficient, $D_{pp}(p)$ is the momentum space diffusion coefficient, and $Q(E, r)$ is the source term. The relationship between the coefficients is described by the following equation in quasi-linear theory:

$$D_{pp} \approx \frac{4}{3\delta(4-\delta^2)}\, v_A^2\, \frac{p^2}{D_x} \tag{1.22}$$

where v_A is the Alfvén speed and δ is the rigidity dependence of diffusion. The observed flattening of secondary-to-primary ratios, such as B/C, is most effectively caused by reacceleration at low to intermediate energies (∼0.1–10 GeV/nucleon). Models that include reacceleration, such as those developed by Strong & Moskalenko [25] and Maurin et al. [26], fit a wide range of CR data better than pure diffusion or convection models. The best-fitting values suggest that v_A ranging from 20 to 40 km s^{-1} and Galactic halo heights between 4 and 12 kpc. The reacceleration model s used as baseline in recent numerical propagation algorithms like GALPROP [27] and DRAGON [28] despite the fact that it introduces more parameters and relies on turbulence assumptions [26].

1.7.5 UHE cosmic-ray propagation

CRs with energies above 10^{18} eV propagate through the Galactic and extragalactic space in a nearly rectilinear motion. The Larmor radius of these particles exceeds the typical size of the Galactic halo making diffusion-based models inapplicable [29]. A critical effect in this regime is the GZK effect (discussed in section 1.2). The mean free path of these particles is few tens of megaparsecs (Mpc). As a result, the observable UHECR population is expected to originate from sources within the so-called GZK horizon. UHECRs can in principle be used to search for their astrophysical sources since their trajectories are less affected by magnetic fields unlike low energy CRs. For example, a proton from the direction of the radio galaxy Centaurus A (at 3–5 Mpc, within the GZK radius) would be deflected by the regular component of the Galactic magnetic field by an angle

$$\Delta\theta_{\rm Gal} \approx (2.3^\circ \pm 0.24^\circ)\, \frac{Z}{E_{20}} \tag{1.23}$$

where E_{20} is the cosmic ray energy in units 10^{20} eV and Z is its charge. The uncertainty reflects our incomplete knowledge of the Galactic magnetic field structure [30].

Moreover, a deflection occurs in the extragalactic space due to turbulent intergalactic

magnetic fields, estimated as

$$\delta\theta_{\rm XGal} \approx 0.15^\circ \left(\frac{D}{3.8\ {\rm Mpc}} \cdot \frac{\lambda_{\rm XGal}}{100\ {\rm kpc}}\right)^{1/2} \left(\frac{B_{\rm XGal}}{1\ {\rm nG}}\right) \frac{Z}{E_{20}} \tag{1.24}$$

where D is the source distance, $\lambda_{\rm XGal}$ the field coherence length, and $B_{\rm XGal}$ its rms strength [31]. For light primaries (protons or helium nuclei), deflections remain small enough ($< 10^\circ$) allowing a positional correlations with candidate sources. However, for heavier particles, such as that inferred by the Pierre Auger Observatory at the highest energies, would cause larger deflections, complicating source identification. If neutrons contribute significantly to the UHECR flux, the magnetic field would not affect their propagation. However, their finite rest frame lifetime of $\sim$ 15 minutes limits their range: a neutron with $E \approx 10^{20}$ eV (Lorentz factor $\Gamma \sim 10^{11}$) can travel only ~ 1 Mpc before decaying.

References

[1] V. F. Hess, *Physikalische Zeitschrift*, vol. 13, pp. 1084–1091, 1912.

[2] P. Auger and R. Maze, *C. R. Acad. Sci. (Paris)*, vol. 207 B, p. 288, 1938.

[3] CERN Timeline. "Victor hess discovers cosmic rays." (), [Online]. Available: `https://timeline.web.cern.ch/victor-hess-discovers-cosmic-rays-0`.

[4] K. Greisen, *Phys. Rev. Lett.*, vol. 16, p. 748, 1966. DOI: `10.1103/PhysRevLett.16.748`.

[5] G. T. Zatsepin and V. A. Kuz'min, *J. Exp. Theor. Phys. Lett.*, vol. 4, p. 78, 1966.

[6] M. H. Bergeson *et al.*, *Int. Cosmic Ray. Conf. Plovdiv, Bulgaria*, 1977.

[7] D. B. et al., *Astrophys. J.*, vol. 424, p. 491, 1994. DOI: `10.1086/173906`.

[8] *Nucl. Instrum. Meth. Phys. Res. A*, vol. 523, p. 50, 2004. DOI: `10.1016/j.nima.2003.12.012`.

[9] T. A. Collaboration, *University of Utah news release*, 2004.

[10] G. Karagöz, "Measurement of Helium Flux and Variability in Low Earth Orbit with the Alpha Magnetic Spectrometer," Graduate School of Natural and Applied Sciences, M.S. thesis, Middle East Technical University, 2022.

[11] D. Ravignani *et al.*, *Proc. 39th Int. Cosmic Ray. Conf.*, 2025. [Online]. Available: `https://arxiv.org/abs/2507.08573`.

[12] F. Mehrez, "Design and test of a readout asic for a sipm-based camera: Alps (asic de lecture pour un photodétecteur sipm)," Thèse de doctorat, Université Grenoble Alpes (ComUE), 2015.

[13] P. Travnicek, "Detection of high-energy muons in cosmic ray showers," Ph.D. thesis, Charles University, Faculty of Mathematics and Physics, 2004.

[14] A. R. Bell, *Mon. Not. R. Astron. Soc.*, vol. 182, p. 147, 1978. DOI: 10.1093/mnras/182.2.147.

[15] E. Fermi, *Phys. Rev.*, vol. 75, p. 1169, 1949. DOI: 10.1103/PhysRev.75.1169.

[16] K. Stasiewicz, *arXiv preprint arXiv:2407.15767*, 2024. [Online]. Available: https://arxiv.org/abs/2407.15767.

[17] T. K. Gaisser, R. Engel, and E. Resconi, *Cosmic Rays and Particle Physics*. Cambridge University Press, 2016. DOI: 10.1017/CBO9781139192194.

[18] B. M. Gaensler and P. O. Slane, *Annu. Rev. Astron. Astrophys.*, vol. 44, p. 17, 2006. DOI: 10.1146/annurev.astro.44.051905.092528.

[19] E. Waxman, *Astrophys. J. Lett.*, vol. 452, p. L1, 1995. DOI: 10.1086/309715.

[20] M. Vietri, *Astrophys. J.*, vol. 453, p. 883, 1995. DOI: 10.1086/176448.

[21] A. M. Hillas, *Annu. Rev. Astron. Astrophys.*, vol. 22, p. 425, 1984. DOI: 10.1146/annurev.aa.22.090184.002233.

[22] J. M. Santander, "Observation of cosmic-ray anisotropy at tev and pev energies in the southern sky," Doctoral dissertation, University of Wisconsin–Madison, 2013.

[23] T. K. Gaisser, *Cosmic Rays Particle Physics*. Cambridge University Press, 1990.

[24] J. C. Carvalho and D. ter Haar, *Astrophys. Space Sci.*, vol. 61, p. 49, 1979. DOI: 10.1007/BF00645789.

[25] A. W. Strong and I. V. Moskalenko, *Astrophys. J.*, vol. 509, p. 212, 1998. DOI: 10.1086/306470.

[26] D. Maurin *et al.*, *Astrophys. J.*, vol. 555, p. 585, 2001. DOI: 10.1086/321496.

[27] A. W. Strong *et al.*, *Annu. Rev. Nucl. Part. Sci.*, vol. 57, no. 1, p. 285, 2007. DOI: 10.1146/annurev.nucl.57.090506.123011.

[28] C. Evoli *et al.*, *J. Cosmol. Astropart. Phys.*, vol. 2008, no. 10, p. 018, 2008. DOI: 10.1088/1475-7516/2008/10/018.

[29] S. Hackstein *et al.*, *Mon. Not. R. Astron. Soc.*, vol. 462, p. 3660, 2016. DOI: 10.1093/mnras/stw1903.

[30] A. Keivani *et al.*, *Astropart. Phys.*, vol. 61, p. 47, 2014. DOI: 10.1016/j.astropartphys.2014.07.001.

[31] A. Batista *et al.*, *Phys. Rev. D*, vol. 104, no. 8, p. 083 017, 2021. DOI: 10.1103/PhysRevD.104.083017.

Chapter 2

Cosmic-ray anisotropy

A logical approach to search for the origin of cosmic rays is to examine their arrival directions on earth and identify regions of significant excess that might coincide with the location of known astrophysical objects. Nevertheless, the truth is much more intricate. In contrast to neutral particles, like photons or neutrinos, cosmic rays are charged, and their trajectory is significantly affected by the galactic magnetic field. While propagating in the interstellar medium, cosmic rays undergo several deflections due to the combination of large-scale coherent magnetic fields and small-scale turbulent structures (as discussed in the previous section). These deflections randomize their trajectories, especially at low energies (in the GeV–TeV range), resulting in an isotropic distribution in the arrival direction of cosmic rays. This diffusion process effectively erases the majority of the directional information that may associate a cosmic ray with its astrophysical origin. This section discusses the anisotropy of cosmic rays for different energy ranges.

2.1 Introduction

The deflection of cosmic rays by the Galactic magnetic field (GMF) is characterized by the gyroradius (also known as the Larmor radius)

$$r_{\mathrm{L}} \approx \frac{1}{Z}\left(\frac{E}{10^6\ \mathrm{GeV}}\right)\left(\frac{B}{\mu\mathrm{G}}\right)^{-1} \qquad (\text{in pc}) \tag{2.1}$$

where Z is the electric charge (in units of e) of the incoming particle and E is its energy. B is the strength of the GMF, typically 0.5-2.5 μG [1]. Anisotropy is commonly classified as *small-scale* ($\lesssim 10^\circ$), *medium-scale* (10–45°), or *large-scale* ($\gtrsim 45^\circ$), depending on the value of E and, thus, the value of r_{L}. For cosmic rays with $E > 10^9$ GeV, the gyroradius r_{L} ($\gtrsim$ kpc) is quite higher than the largest scale of the turbulent component of the GMF

($\sim$ a few hundred pc). In this case, the trajectories of incoming particles are scarcely affected by the GMF, and one can explore local structures with angular sizes $\lesssim 10°$. However, for $E < 10^6$ GeV, the gyroradius $r_{\rm L}$ ($\lesssim$ pc) is much smaller than the largest scale of the turbulent component of the GMF. Cosmic rays are hence significantly deflected by the GMF and their propagation becomes diffusive. It is likely that only large structures with angular sizes $\gtrsim 45°$ can be investigated in this energy region. Nevertheless, there is nothing wrong in searching for small-scale anisotropy below 10^6 GeV. Such studies, quite challenging, do not seek to identify the sources of cosmic rays, but rather to constrain propagation models and probe the structure of the local interstellar environment. In the intermediate energy range (10^6–10^9 GeV), the trajectories of cosmic rays and the largest scale of the GMF turbulent component are of the same order of magnitude and one can explore structures with an angular size of about 10–45°.

2.2 Anisotropy of TeV cosmic rays

2.2.1 Large-scale anisotropy

Cosmic rays with TeV energies move through the galaxy diffusively. Although it is not possible to directly search for cosmic ray point sources using their arrival directions, their distribution in the sky exhibits some degree of anisotropy, which is at the per-mille level. In 1935, Compton & Getting published a model to explain the early anisotropy claims made by Hess [2]. This model emphasizes the fact that the rotation of the solar system around the galaxy together with the the earth relative motion with respect to the unknown frame of galactic cosmic rays has a measurable effect on cosmic ray intensity. The soloar system is moving towards a point in the sky with the following coordinates $(\alpha, \delta) = (315°, +49°)$ and with a velocity of 200–300 km/s according to the type of Galactic objects taken as rest frame [3]. This predicted Compton-Getting anisotropy is expected to appear as a dipolar structure, with its maximum aligned with the Sun's direction of motion, and a relative intensity variation expressed as:

$$\frac{\Delta I}{\langle I \rangle} = (\gamma + 2)\,\frac{v}{c}\,\cos\rho \tag{2.2}$$

where I represents the cosmic ray intensity, γ is the spectral index of the comsic ray energy spectrum, v is the velocity of the Earth which results from the motion of the solar system, ρ is the opening angle between the cosmic-ray direction and the velocity vector and c is the speed of light [4]. Replacing the parameters values in the above equation gives a dipole with an amplitude of $\sim 3.5 \times 10^{-3}$. There is currently no observable evidence of this effect.

Due to the Earth rotation around the sun, a similar anisotropy is expected; it is known as Solar Compton-Getting or solar dipole. The Earth orbits the sun at a velocity of ~ 30 km, this will produce a solar dipole with an amplitude of 4.7×10^{-4}. The dipole excess aligns with the velocity vector of the Earth pointing to a position of roughly 90° from the sun along the ecliptic plane. This feature has been observed by several cosmic ray experiments.

Another source of anisotropy arises from the diffusion of cosmic rays in the Galaxy. In the diffusion mechanism of CR propagation, the rate at which particles scatter and spread throughout the Galaxy is described by the diffusion coefficient $D(E)$, as discussed in Section 1.7. Higher-energy cosmic rays diffuse more rapidly and escape the Galaxy on time scales of millions of years. The diffusion coefficient follows a power-law scaling, $D(E) \propto R^{\delta}$, with $\delta \approx 0.3$–0.6, as determined by the turbulence spectrum of the interstellar medium. Unlike the leaky box model, the diffusion theory predicts spatial gradients in the cosmic ray density $n(E)$ as a function of distance from the sources and time since injection. In the presence of the large-scale Galactic magnetic field, these gradients lead to a net drift of particles, producing a dipole anisotropy in the arrival directions. The amplitude of this anisotropy is then given by:

$$\delta(E) = \frac{3D(E)\,\nabla n(E)}{c\,n(E)} \tag{2.3}$$

Here, $\nabla n(E)$ points toward regions of higher cosmic ray density. Since $D(E) \propto E^{\alpha}$, with $\alpha \approx 0.3$–0.6, the anisotropy amplitude is expected to scale as $\delta(E) \propto E^{\alpha}$, with typical values in the range from 10^{-3} to 10^{-2}. This framework naturally explains the small but measurable deviations from isotropy observed in the cosmic-ray sky.

2.2.2 Experimental observations

Nagachima et al. [5] investigated the origin of large-scale CR anisotropies in the multi-TeV energy range based on data collected by underground muon detectors located in Japan. They claimed that the observed sidereal anisotropy can be decomposed into a Galactic component, reflecting diffusion and drift of cosmic rays in the Galaxy, and a helio-tail component associated with the solar wind outflow and the downstream structure of the heliosphere. The helio-tail anisotropy manifests as an excess of cosmic rays near the right ascension RA $\approx$ 6 h (90°) and declination Dec $\approx -24°$, which is roughly opposite the direction of the solar system's motion through the local interstellar medium (Fig. 2.1). The excess is referred to as "tail-in" anisotropy, while the deficit region which follows the direction (RA$\approx$ 12h (180°), Dec $\approx$ 20°) is called the "loss cone". Moreover, their study

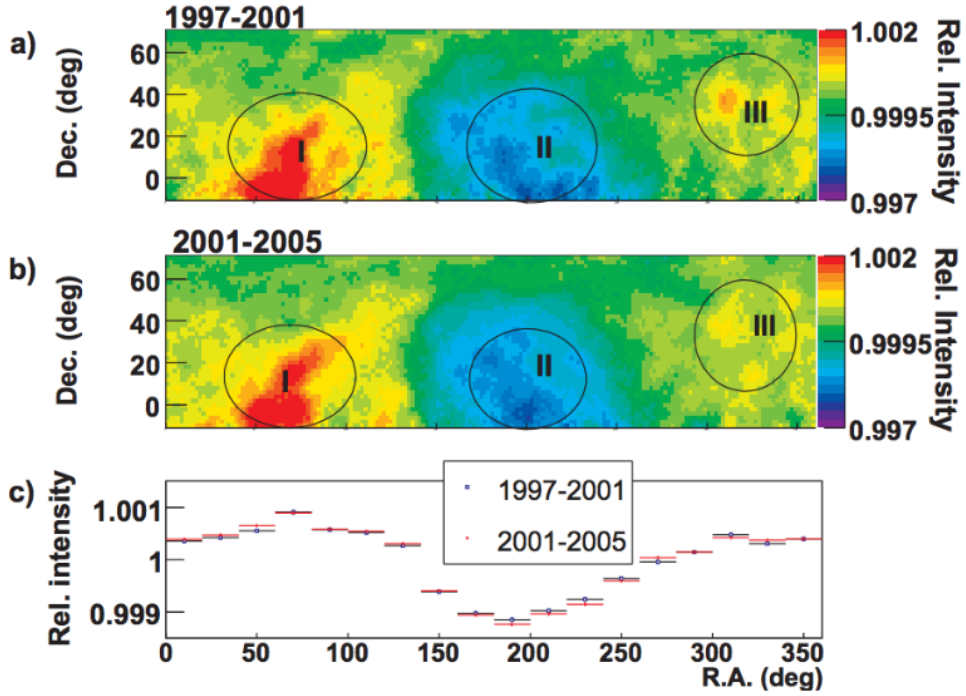

Fig. 2.1: Anisotropy sky map derived by the Tibet-ASγ collaboration [6] highlighting the tail in excess (I) and the loss cone (II) regions and the board excess (III) interpreted to be linked with the Galactic region Cygnus. The observed anisotropy pattern remains stable over time, as shown in panels (a) and (b). Additionally, panel (c) provides a one-dimensional projection of the anisotropy.

demonstrated that the helio-tail anisotropy exhibits seasonal variation: its amplitude is stronger in December when the Earth is aligned closest to the heliotail direction and weaker in June. In contrast, the Galactic anisotropy remains constant in both the amplitude and orientation which reflects the propagation of Galactic CRs through the ISM [6].

Investigating higher energies, the Tibet Air Shower Array [6] located in Yangbajing reported a dipolar anisotropy in the arrival distribution of cosmic rays with respect to the Sun's position, using a dataset of 37 billion events with energies ranging from 4 TeV to 300 TeV collected between 1997 and 2005. The amplitude of the dipole, $\sim 4 \times 10^{-4}$, is consistent with the known solar Compton–Getting effect. Moreover, a significant excess was observed in the sidereal time distribution at energies of about 3 TeV, which can be described as a dipole structure representing the large-scale anisotropy of cosmic rays. They also confirmed the "tail-in" excess and "loss-cone" deficit features discussed earlier. In addition, they demonstrated that the expected Galactic Compton–Getting effect, arising from the solar system's orbital motion around the Galactic center, was absent. This null detection, with a sensitivity of $\sim 0.03\%$, provides strong evidence that Galactic cosmic rays are not stationary in the Galactic rest frame but corotate with the local Galactic magnetic field.

Observations from other experiments located in the northern hemisphere, such as Milagro [7], Super kamiokande [8] and AGRO-YBJ [9] are in agreement with those previously reported by the Tibet experiment.

The large-scale pattern is commonly described either by a single dipole or by a superposition of dipole and quadrupole terms, each defined by its amplitude and phase. For the ARGO-YBJ data, the variation of the relative intensity δI with right ascension α was fitted using the function:

$$\delta I(\alpha) = A_1 \cos(\alpha - \phi_1) + A_2 \cos\Big(2(\alpha - \phi_2)\Big). \tag{2.4}$$

The fit yielded amplitudes $A_1 = 6.8 \times 10^{-4}$ and $A_2 = 4.9 \times 10^{-4}$, with phases $\phi_1 = 39.1°$ and $\phi_2 = 281°$.

Building on these earlier measurements, more recent experiments such as HAWC [10] and LHAASO [11] observatories have provided complementary results with improved precision. The analysis of 2 years of data provided by the HAWC Observatory, located in Mexico, reveals an energy-dependent anisotropy in cosmic rays, primarily characterized by a dipole moment with a phase in right ascension at approximately 40°. The amplitude of this dipole slowly rises from $8{\times}10^{-4}$ at 2 TeV to $14{\times}10^{-4}$ around 30 TeV, after which it decreases. To estimate cosmic-ray energies and to account for observational limitations, a maximum likelihood-based estimator was employed (details in the next section). This technique helps to compensate for the attenuation of the dipole strength that occurs with mid-latitude detectors like HAWC, which only observe a fraction of the full sky at any given time. The results are presented in Fig. 2.2. These results contribute to improving constraints on local cosmic-ray accelerators and the structure of intervening magnetic fields.

More recently, the LHAASO experiment has measured the large-scale cosmic-ray anisotropy with high statistics using its Water Cherenkov Detector Array (WCDA) in an energy range from about 1 TeV to 150 TeV, based on two years of data including roughly 230 billion events (Fig. 2.3). At lower energies, a distinct sidereal dipole structure was detected with an amplitude and phase that agree with past experiments like ARGO-YBJ and HAWC. Beyond 30 TeV, the signal amplitude starts to drop, suggesting a potential energy-dependent change in the distribution or propagation of Galactic cosmic rays, but the anisotropy remains largely consistent up to that point. Furthermore, the analysis method was confirmed by the detection of the anticipated solar Compton-Getting dipole with the proper amplitude and phase (Fig. 2.4). These findings greatly enhance our understanding of the energy development of cosmic-ray anisotropy and serve as a benchmark for comparison with other detectors [11].

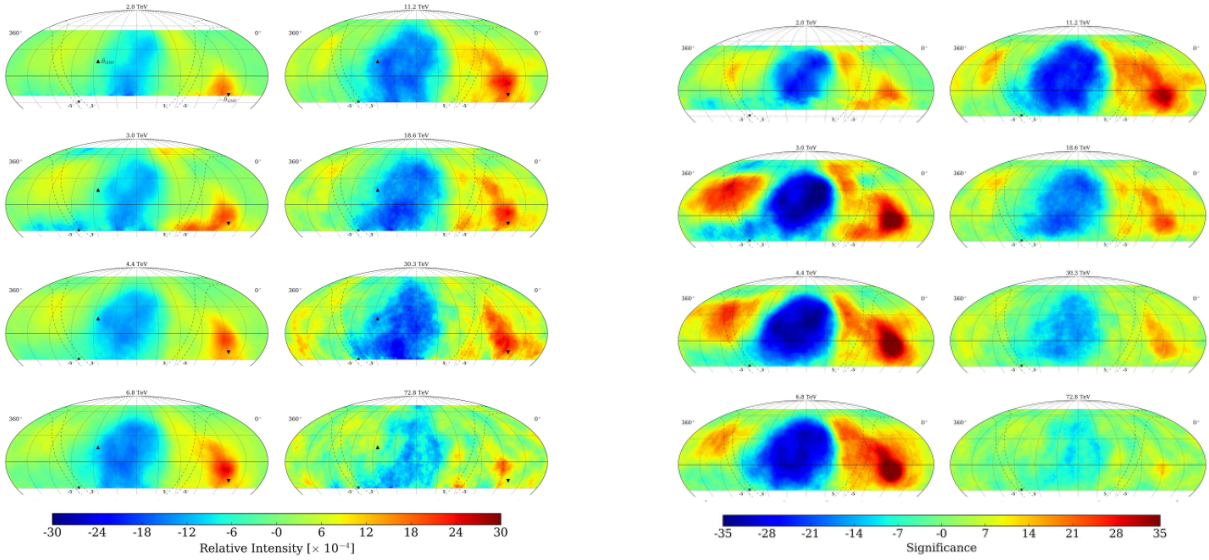

Fig. 2.2: Relative intensity δI (left) and statistical significance anisotropy maps produced by HAWC experiment showing a clear dipolar structure. Taken from [10].

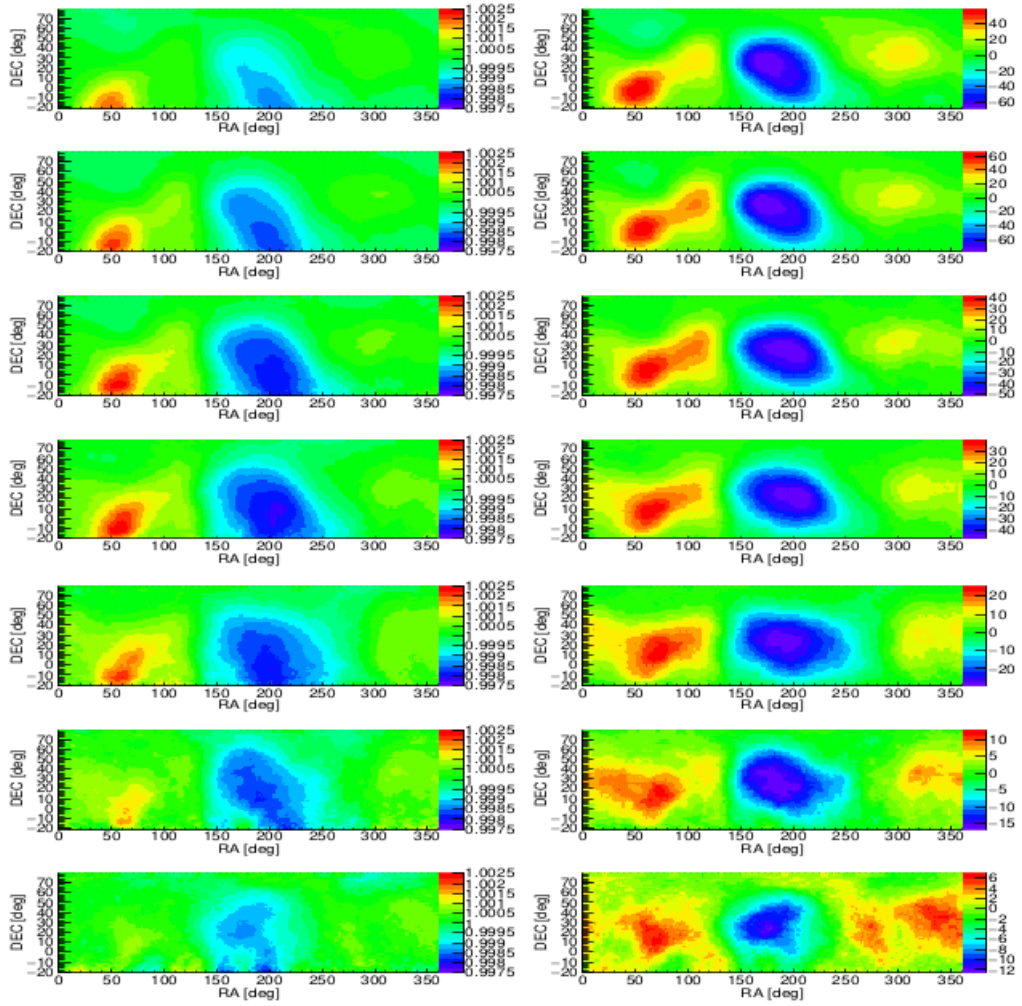

Fig. 2.3: 2D maps of anisotropy intensity in the sidereal time frame at different energies produced by the LHAASO collaboration. Taken from [11].

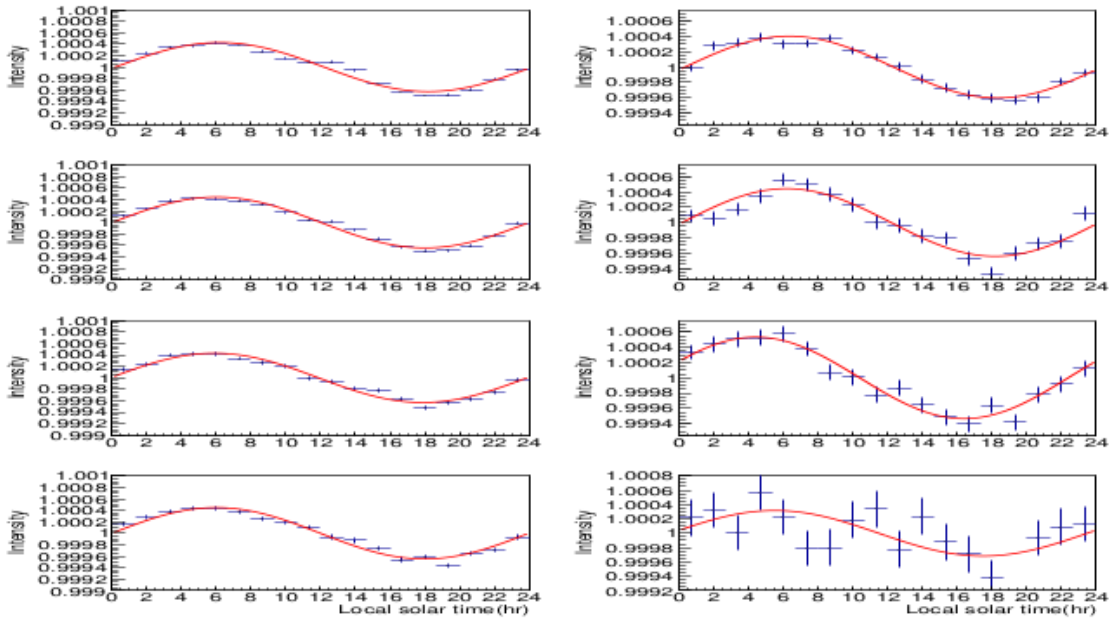

Fig. 2.4: 1D projection of the solar CG dipole. Taken from [11].

As for observations from the Southern Hemisphere, IceCube [12], a cubic-kilometer neutrino telescope at the South Pole, has recently reported an updated measurement of cosmic-ray anisotropy based on 12 years of data. The analysis spans energies from about 13 TeV up to 5.3 PeV and reveals a pronounced dipole component in the arrival direction distribution. The dipole amplitude decreases with energy, reaching a minimum of order 10^{-3} near 100 TeV, before increasing again up to the PeV scale (Fig. 2.5). In addition to this change in strength, the orientation of the dipole evolves with energy: at $\sim$ 13 TeV the dipole maximum is located near right ascension (RA) $\simeq 50°$, while by $\sim$ 100 TeV the dipole direction has shifted by roughly 180°, pointing instead toward RA $\simeq 230°$. This flip in phase, together with the reduction of amplitude above the PeV range, confirms that the anisotropy is not static but exhibits a marked energy dependence, which is likely tied to the transition between local and large-scale propagation effects in the Galactic magnetic field.

The combined analysis of HAWC and IceCube data [13] showed a full sky measurement of cosmic-ray anisotropy at 10 TeV (Fig. 2.6). By merging the complementary fields of view of both observatories HAWC in the northern hemisphere and IceCube in the southern hemisphere, the study resolved the anisotropy patterns across the entire sky with unprecedented sensitivity. The horizontal dipole components were measured to be equal to $\delta_{0h} = 9.16 \times 10^{-4}$ and $\delta_{6h} = (7.25 \pm 0.04) \times 10^{-4}$, which represent the orthogonal projections of the dipole onto the equatorial plane, corresponding to an overall dipole amplitude of $A \simeq 1.2 \times 10^{-3}$ with a phase $\alpha = 38.4°$. Moreover, the study inferred the direction of the local interstellar magnetic field from the boundary between excess and deficit regions at R.A. $229.2° \pm 3.5°$ and decl. $11.4° \pm 3.0°$.

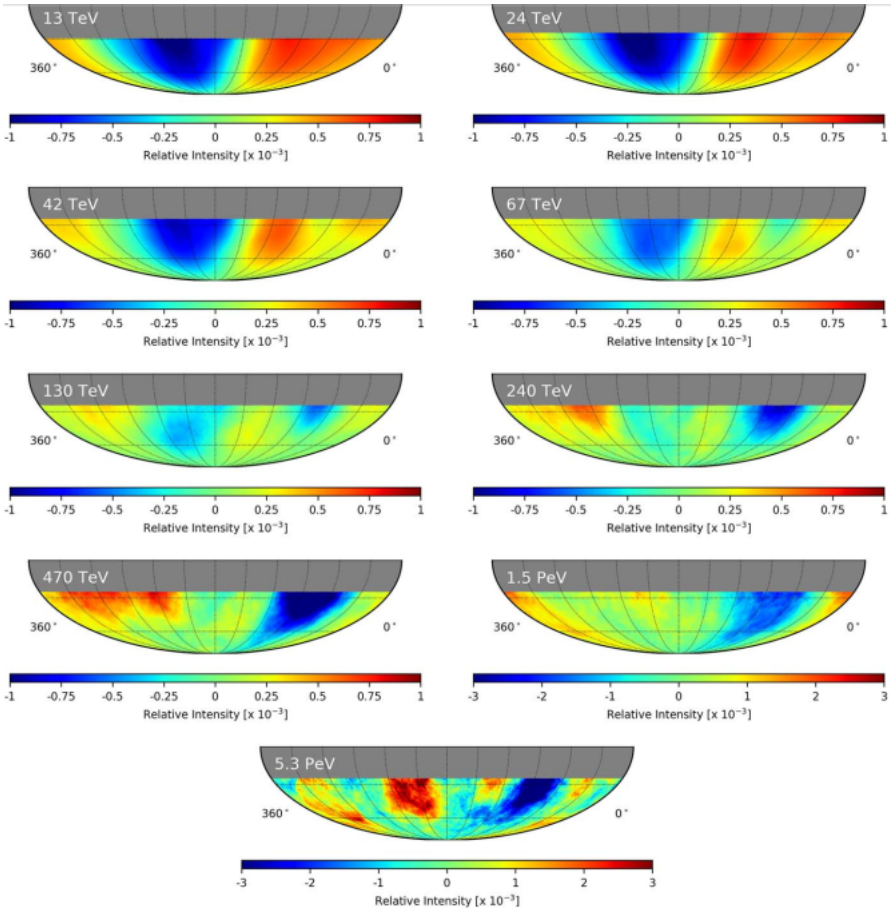

Fig. 2.5: Relative intensity sky map from the Icecube experiment[12] shown as function of the primary cosmic ray energy, illustrate the energy dependence of the dipole and reveal a phase shift around 100 TeV.

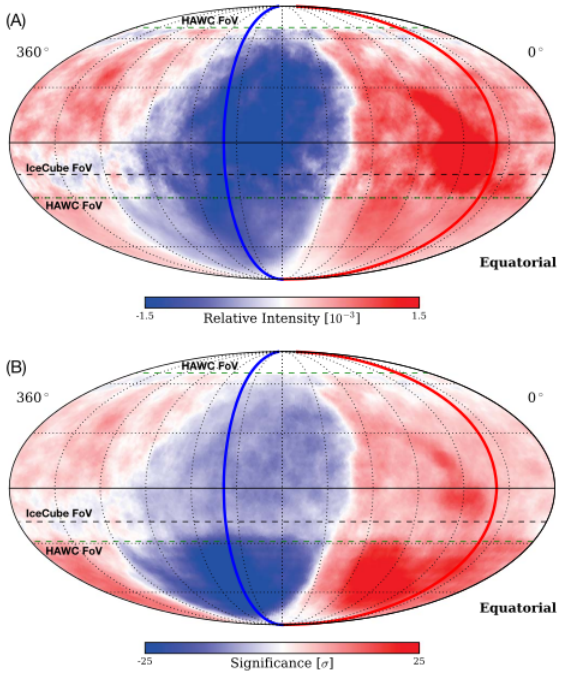

Fig. 2.6: (A) sky map of the relative intensity δI, (B) the corresponding statistical significance from the combined analysis of HAWC and IceCube. Taken from [14].

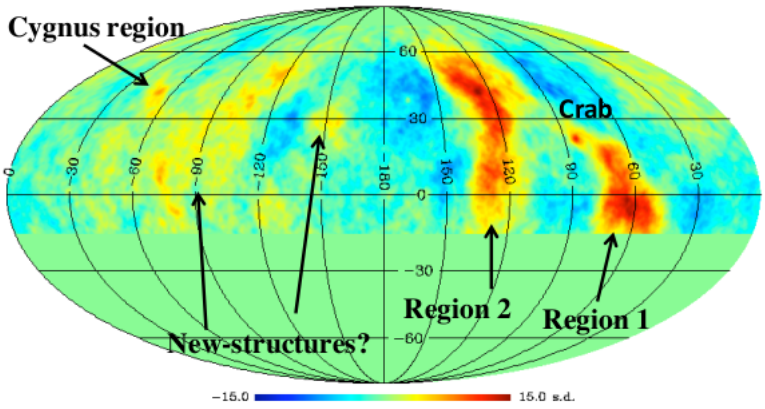

Fig. 2.7: Relative intensity observed by ARGO-YBJ experiment. Adapted from [15].

2.2.3 Small-scale anisotropy

The presence of small-scale structures poses a more significant theoretical challenge, unlike the large-scale anisotropies of cosmic rays which can be effectively addressed through the framework of diffusive propagation in the Galaxy. Observations in the northern sky have revealed localized regions of excess flux at multi-TeV energies, the most notable being two hotspots identified by the Milagro experiment with fractional excesses of order 10^{-4}. These features have stimulated a variety of interpretations, ranging from particle transport along magnetic field lines in the presence of nearby "magnetic mirrors" or "nozzles", to associations with local supernova remnants such as Geminga, or beam-like enhancements produced by propagation effects in a turbulent interstellar medium. A heliospheric origin has also been considered, but the density of interstellar material in the heliotail is too low to support this explanation. Subsequent measurements by ARGO-YBJ confirmed the existence of these excess regions and hinted at additional small-scale structures, reinforcing the view that localized anisotropies are a persistent and significant feature of the cosmic-ray sky (Fig. 2.7).

More recently, the GRAPES-3 experiment in India [16], located near the equator and sharing an overlapping field of view with detectors in both the Northern and Southern hemispheres, reported the observation of two localized excess regions, labeled A and B, using a data set of 3.7×10^9 CR events (Fig. 2.8). Region A covers a right ascension range of 50°–80° and a declination range of −15° to 30°, with an amplitude of $(6.5 \pm 1.3) \times 10^{-4}$ and a statistical significance of 6.8σ. Region B extends over right ascensions 110–140° and declination from −10° to 30°, with a relative intensity of $(4.9 \pm 1.4) \times 10^{-4}$ detected at a significance of 4.7σ. These features are consistent with the small-scale structures previously reported by ARGO-YBJ, Milagro, and HAWC.

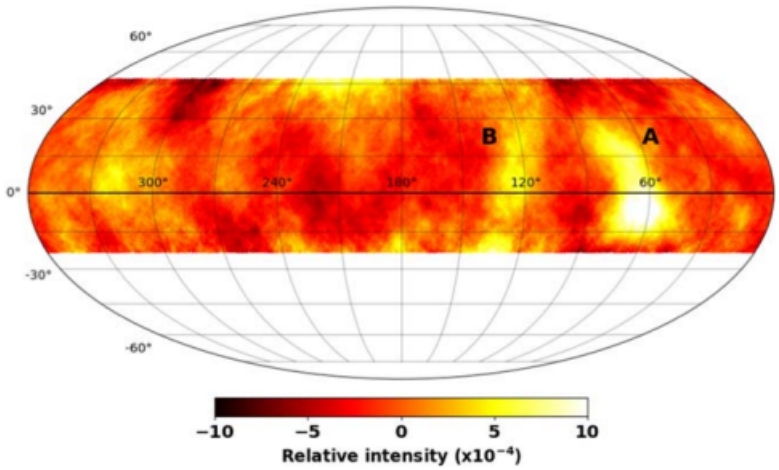

Fig. 2.8: Relative intensity map from the GRAPES-3 experiment [16]. A large-scale deficit is visible while smaller features labelled A and B appear prominently.

2.3 Anisotropy of PeV cosmic rays

In this energy regime, the gyroradius of CRs grows linearly and becomes comparable to the coherence scale of the Galactic magnetic field and to the characteristic dimensions of the Galaxy itself. Once this condition is reached, the assumption of isotropized diffusion breaks down, and cosmic rays begin to retain more directional information on their origin. The exact energy of this transition is not known, as it depends on both the still uncertain structure of the Galactic magnetic field and the chemical composition of the primaries, but theoretical arguments suggest that it is likely to occur in the range between the PeV and EeV. This makes the PeV domain particularly compelling, since it may coincide with the energy at which the transition from Galactic to extragalactic origin of CRs happens.

The EAS-TOP experiment [17], located at Campo Imperatore in Gran Sasso, Italy was the first experiment to report evidence for modulations in the right ascension distribution of cosmic rays with median energies of 110 TeV and 370 TeV, using a data set of about two billion air showers collected between 1992 and 1999. The anisotropy was parametrized by fitting harmonic functions suggesting the presence of large-scale structures beyond what would be expected from pure statistical fluctuations. These results were intriguing but remained limited in statistical power and were not independently confirmed at the time.

A more extensive investigation was later performed by the KASCADE experiment and subsequently by its extended configuration KASCADE-Grande [18]. Together, they did cover the energy range from a few hundred TeV to beyond 10^{17} eV. KASCADE did not find evidence for anisotropy, and instead set 95% confidence level upper limits on the dipole amplitude (Fig. 2.9). These upper limits are set for energies ranging from $\sim 10^{-3}$ at primary energies of 300 TeV up to $\sim 10^{-2}$ at 6 PeV. The follow-up KASCADE-Grande

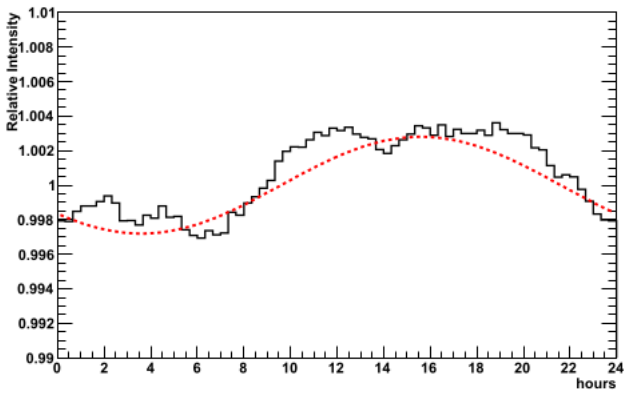

Fig. 2.9: Sidereal anisotropy reported by the KASCADE-GRANDE experiment. Taken from [18].

analysis extended the search to higher energies, setting limits of 5×10^{-3} at 3 PeV and up to ~ 0.3 at 300 PeV. In a more recent observation in 2019, the KASCADE-Grande collaboration revisited this question using an improved analysis technique based on the east–west method (see next section for details). By studying the sidereal time distribution of events above 10^{15} eV, they derived the dipole component of the anisotropy and reported a first harmonic with a significance of 3.5σ, leading to updated upper limits. The measured phase of the first harmonic was found to be consistent with that reported by EAS-TOP, IceCube, and IceTop in the 10^{14}–10^{15} eV range, confirming the systematic shift in phase at energies beyond $\sim 2 \times 10^{14}$ eV. IceCube and its surface array IceTop have considerably advanced this field by observing a similar dipolar structure that extends up to multi-PeV energies, providing continuity between the TeV and PeV domains as reported in their latest study.

2.3.1 Anisotropy at ultra-high energies

The Pierre Auger Observatory, with nearly two decades of observations, has provided the most precise measurements of anisotropy in this regime. A comprehensive analysis of 19 years of data has confirmed the presence of a large-scale dipole anisotropy above ~ 8 EeV, now detected with a significance of 6.8σ [19]. The dipole amplitude is at the level of a few percent, and its orientation in equatorial coordinates points toward right ascension $\sim 100°$ and declination $\sim -24°$, significantly offset from the Galactic center (Fig. 2.10). This signal has remained stable over time, with no measurable temporal variation and an upper limit of 0.3% per year.

In addition, Auger extended the search to lower energies, down to 3×10^{16} eV and found a smooth evolution of the equatorial dipole component with energy [20]. Complementary analyses of the angular power spectrum show that no higher-order multipole components

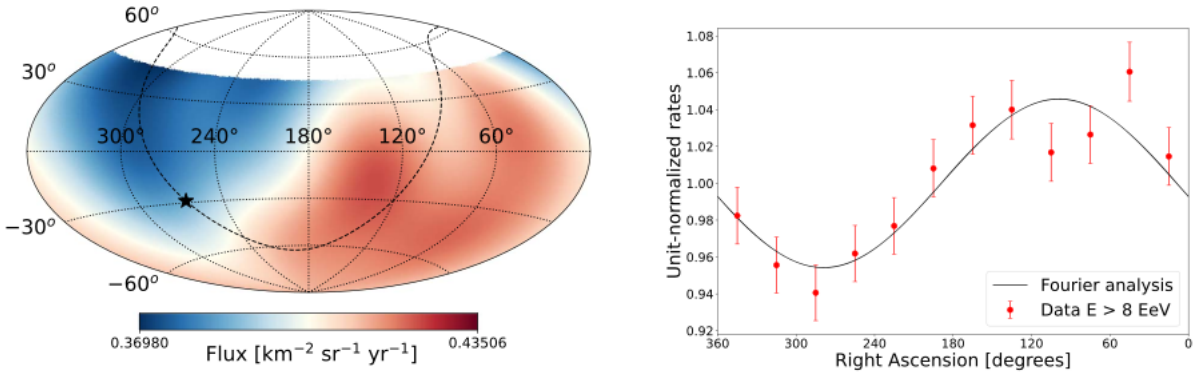

(a) (b)

Fig. 2.10: (a) sky map of the CR flux above 8 EeV. (b) Right ascension (RA) distribution showing the dipolar structure. Taken from [20].

beyond the dipole contribute significantly to the anisotropy [20]. When these empirical results are compared to astrophysical models constrained by the Auger spectrum and mass-composition data above 6×10^{17} eV, they strongly suggest that the observed dipole is linked to the distribution of matter in the nearby extragalactic universe, rather than being related to Galactic sources or local magnetic effects.

These updated measurements represent a milestone in ultra-high-energy cosmic-ray studies. While TeV–PeV experiments probe the interplay of Galactic diffusion and nearby sources, the Auger findings at EeV energies provide the clearest evidence so far that cosmic rays above the ankle are extragalactic in origin, tracing the large-scale structure of the universe itself.

2.4 Analysis methods

The standard approach for studying cosmic-ray anisotropy consists of comparing the *data map*, which stores the arrival directions of detected events, to a *reference map* representing the expected directional response of the detector to an isotropic cosmic-ray flux. Any deviation of the data map from the reference map might be regarded as a signal. As aforementioned, the amplitude of cosmic-ray anisotropy in the TeV-PeV energy range is of the order of one-per-mille. Sensitivity to such a tiny effect requires large collecting areas along with a long operation time.

More specifically, the measured flux of cosmic rays is considered as the sum of an isotropic component and an anisotropic component:

$$I(\alpha, \beta) = I_{\text{iso}} + I_{\text{ani}}(\alpha, \beta) \tag{2.5}$$

where (α, β) are the right ascension and declination, respectively. $I_{\rm iso}$ is the isotropic component and $I_{\rm ani}(\alpha, \beta)$ is the anisotropic component. The anisotropy is defined as

$$\delta I(\alpha, \beta) = \frac{I(\alpha, \beta) - I_{\rm iso}}{I_{\rm iso}} = \frac{I(\alpha, \beta)}{I_{\rm iso}} - 1 \tag{2.6}$$

With the data map and the reference map in hand, we can calculate the anisotropy on a pixel-by-pixel basis:

$$\delta I_i = \frac{N_i - \langle N \rangle_i}{\langle N \rangle_i} = \frac{N_i}{\langle N \rangle_i} - 1 \tag{2.7}$$

where N_i and $\langle N \rangle_i$ are the counts of the ith pixel of the data map and the reference map, respectively.

The best way to obtain this reference level is injecting an isotropic flux of simulated air showers into a Monte Carlo model of the detector and then analysing the event distribution that meets the same trigger conditions as the actual data. This approach is only feasible for significant anisotropies (exceeding about 10%), since detector simulations often lack the accuracy necessary to discern minor fluctuations. For anisotropies with amplitudes on the order of 10^{-3} to 10^{-4}, as expected in the TeV–PeV energy range, such a method becomes unfeasible owing to the high agreement required between simulation and empirical data. Consequently, the reference level is directly obtained from the data. The techniques commonly used are discussed in the following subsections.

The search for anisotropy in the arrival directions of primary cosmic rays observed by Earth-bound instruments is complicated, mainly due to several inescapable observational biases. It relies on analyzing the variation of the number of events with the local sidereal time (or right ascension). However, the counting rates are affected by instrumental and atmospheric effects, which can be orders of magnitude larger than the expected anisotropy signal. Before conducting any anisotropy analysis, it is therefore essential to disentangle the detector and atmospheric effects from the data to eliminate any bias and avoid misinterpretation of variations in the cosmic-ray flux. Monte Carlo simulation is inefficient in the TeV-PeV energy range as it cannot estimate the instrument exposure with the required precision for reconstructing per-mille-level anisotropies. The only alternative is to use the experimental data themselves to construct the isotropic reference map. Many data-driven methods have been developed in this respect, each with its strengths and limitations. These methods can reveal broad anisotropy features in large samples, even if the angular resolution is poor. However, their implementation requires the detector to be as stable as possible and to operate uniformly over time. Among the most widely used are the *time-scrambling method* [21], the *direct-integration method* [22], the *East-West method* [23], [24], and the *iterative maximum-likelihood method* [25].

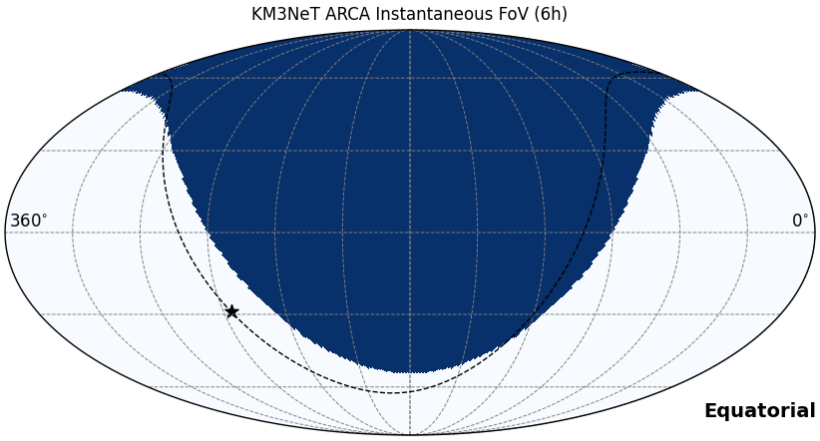

Fig. 2.11: Instantaneous field of view of the KM3NeT/ARCA detector at a local sidereal time of 6 hours in equatorial coordinates.

2.4.1 Rayleigh analysis

The field of view (FOV) of Earth-bound detectors is shaped as a cone with a constant declination (δ) and points in different directions as the Earth rotates. An example of the FOV of KM3NeT/ARCA detector at a fixed LST is shown in Figure 2.11. The anisotropy dependence upon declination is not accessible by such instruments. For this reason, the study of cosmic-ray anisotropy is usually carried out only in right ascension (α) through a harmonic analysis of the counting rate within the declination band determined by the FOV of the detector [26]. This method can help to estimate the amplitude of the different harmonics, the corresponding phases (angle of the maximum intensity), and the probability of detecting a spurious signal due to a fluctuation of an isotropic flux with an amplitude equal or greater than the observed one. In general, the first harmonic (dipole) and the second harmonic (quadripole) are derived from data by measuring the counting rate as a function of the right ascension (or sidereal time) and fitting the results to a sine wave.

To quantify the anisotropy, the intensity distribution in right ascension $I(\alpha)$ can be expressed as a Fourier series [27]:

$$I(\alpha) = \frac{a_0}{2} + \sum_{k=1}^{\infty} (a_k \cos k\alpha + b_k \sin k\alpha) = \frac{a_0}{2} + \sum_{k=1}^{\infty} r_k \cos(k\alpha - \varphi_k) \tag{2.8}$$

where a_k and b_k are the Fourier coefficients of the harmonic of order k. We have

$$\begin{cases} a_k = r_k \cos\varphi_k \\ b_k = r_k \sin\varphi_k \end{cases} \qquad \begin{cases} r_k = \sqrt{a_k^2 + b_k^2} \\ \varphi_k = \tan^{-1}\left(\dfrac{b_k}{a_k}\right) \end{cases} \tag{2.9}$$

r_k and ϕ_k are the amplitude and phase of the harmonic of order k, respectively. The Fourier coefficients a_k and b_k can be deduced from the right ascension α_1, α_2, ..., α_N of N collected events:

$$\begin{cases} a_k = \dfrac{2}{N} \sum\limits_{i=1}^{N} \cos(k\alpha_i) \\ b_k = \dfrac{2}{N} \sum\limits_{i=1}^{N} \sin(k\alpha_i) \end{cases} \tag{2.10}$$

The amplitude and phase of the first harmonic (dipole) provide, at first order, the degree of the large-scale anisotropy. Although the observed anisotropy is not a simple dipole, measuring the first harmonic allows a quantitative comparison between the results from different experiments. To account for the non-uniformities in the detector exposure as a function of time, we usually proceed with *weighted* harmonic analysis, introducing weights in the Fourier coefficients. For the first harmonic, we have:

$$\begin{cases} a = \dfrac{2}{\mathcal{N}} \sum\limits_{i=1}^{N} w_i \cos\alpha_i \\ b = \dfrac{2}{\mathcal{N}} \sum\limits_{i=1}^{N} w_i \sin\alpha_i \end{cases} \qquad \mathcal{N} = \sum_{i=1}^{N} w_i \tag{2.11}$$

where w_i are the weight factors and $\mathcal{N}$ is a normalization factor. The weighted first-harmonic analysis in right ascension (α) is often referred to as Rayleigh analysis. If the amplitude of the first harmonic is non zero, it is very important to evaluate the chance that this harmonic arises from a fluctuation of an isotropic distribution. The probability P to obtain an amplitude equal or larger than r as a result of a fluctuation of an isotropic flux is given by the well-known Rayleigh formula [26]:

$$P(\geq r) = \exp\left(-\frac{\mathcal{N} r^2}{4}\right) \tag{2.12}$$

The uncertainties of the amplitude and phase of the first harmonic are given by

$$\sigma_r = \sqrt{\frac{2}{\mathcal{N}}} \qquad \sigma_\varphi = \frac{\sigma_r}{r} \tag{2.13}$$

The Rayleigh analysis can be applied to data only when full detection efficiency is achieved. If the trigger conditions do not reach 100% efficiency, the systematic effects arising from

the geometry of the detector layout cannot be fully corrected. Therefore, it is more appropriate to combine the Rayleigh analysis with an additional technique, such as the East-West method, which takes care of correction for non-uniformities.

2.4.2 East-West method

Let us assume the presence of a genuine large-scale cosmic-ray anisotropy of dipolar structure. As the Earth rotates, one-half of the detector FOV will be closer to the dipole excess region for half a day. Then, the second half of the detector FOV becomes closer to the dipole excess region during the next half-day. The whole process is repeated every day. It is evident that the nearer a specific direction to the dipole excess region, the higher the counting rate from this direction. The difference in the counting rates from the Eastern and the Western hemispheres is thus subject to an oscillation whose amplitude and phase are expected to be equivalent to those of the genuine large-scale anisotropy.

The aim of the East-West method is the reconstruction of the equatorial component of a genuine large-scale anisotropy signal by comparing counting rates of events coming from the East and West directions [23], [24]. The subtraction removes spurious experimental effects which are generally independent of the incoming direction. As a consequence, the method does not require corrections for detector acceptance or atmospheric variation the approach assumes a symmetrical azimuthal direction efficiency with respect to the East-West axis. if any asymmetries are present, appropriate corrections must be applied. This method is less sensitive to anisotropy than the Rayleigh analysis, but the systematic uncertainties are under better control. It was first applied to analyse air shower observations at Mt. Norikura [23] and has since been utilised in major experiments such as Tibet-ASγ [28], EAS-TOP [17], Baksan [29], Pierre Auger Observatory [30], [31], and KASCADE-Grande [18].

Let $I_{\mathrm{E}}(t)$ and $I_{\mathrm{W}}(t)$ represent the number of events detected from the East and the West directions at a given LST (local sidereal time) t. The key idea of the EW method is that the difference between these two counting rates is directly related to the first derivative of the total event rate (I_{tot}) [24]. This relationship is given by the following equation:

$$\frac{\mathrm{d}I_{\mathrm{tot}}}{\mathrm{d}t} = \frac{I_{\mathrm{E}}(t) - I_{\mathrm{W}}(t)}{\delta t} \equiv \frac{D(t)}{\delta t} \tag{2.14}$$

here δt represent the average hour angle between the vertical and the two sectors. Using this definition, the corresponding Fourier coefficients for the EW method can be expressed as:

$$\begin{cases} a_{\mathrm{EW}} = \dfrac{2}{N} \sum\limits_{i=1}^{N} \cos\left(\dfrac{2\pi t_i}{T_{\mathrm{s}}} + \xi_i\right) \\ b_{\mathrm{EW}} = \dfrac{2}{N} \sum\limits_{i=1}^{N} \sin\left(\dfrac{2\pi t_i}{T_{\mathrm{s}}} + \xi_i\right) \end{cases} \tag{2.15}$$

where N denotes the number of total events collected and T_{s} the sidereal period. The variable takes the value 0 for events arriving from the East ($0 < \varphi < \pi$) and π for events arriving from the West ($\pi < \varphi < 2\pi$). The Fourier amplitude, r, and phase, φ, are then given by [24]

$$\begin{cases} r = \dfrac{1}{\delta t}\sqrt{a_{\mathrm{EW}}^2 + b_{\mathrm{EW}}^2} \\ \varphi = \tan^{-1}\left(\dfrac{b_{\mathrm{EW}}}{a_{\mathrm{EW}}}\right) + \dfrac{\pi}{2} \end{cases} \tag{2.16}$$

Just as in the Rayleigh analysis, the probability of observing an amplitude greater than that what would be expected under the assumption of isotropy is given by:

$$P(\geq r) = \exp\left(-\frac{r^2}{2\sigma_r^2}\right) \tag{2.17}$$

with

$$\sigma_r = \frac{1}{\delta t}\sqrt{\frac{2}{N}} \qquad\qquad \sigma_\varphi = \frac{\sigma_r}{r} \tag{2.18}$$

2.4.3 Iterative maximum likelihood method

The iterative maximum-likelihood method was designed to effectively recover the amplitude of large-scale features in the anisotropy that are attenuated as a result of the difference between the instantaneous and integrated FoV [25]. This issue is inherent to detectors located in mid-latitude regions such as ARCA (but not exclusively). It was applied to analyse the data from HAWC, IceCube, and KASCADE-Grande [10], [32], [33].

This method is based on the standard ansatz that the detector exposure $\mathcal{E}$ per solid angle and sidereal time t, accumulated over many sidereal days, can be factorized into a time-dependent event rate $E(t)$ and a time-independent relative acceptance $\mathcal{A}(\theta, \varphi)$:

$$\mathcal{E}(t,\,\theta,\,\varphi) = E(t)\,\mathcal{A}(\theta,\,\varphi) \tag{2.19}$$

$E(t)$ is the angular-integrated exposure per sidereal time:

$$E(t) = \int \mathcal{E}(t,\,\theta,\,\varphi)\,\mathrm{d}\Omega \tag{2.20}$$

The relative acceptance of the detector, supposed here to be approximately constant over time, is normalized as

$$\int \mathcal{A}(\theta,\,\varphi)\,\mathrm{d}\Omega = 1 \tag{2.21}$$

Assuming that the flux of cosmic rays in the TeV-PeV energy range remains constant over the lifetime of ground-based detectors such as ARCA, the angular distribution of the flux can be expressed in terms of the equatorial coordinates $(\alpha,\,\delta)$ as

$$\phi(\alpha,\,\delta) = \phi^{\mathrm{iso}}\,I(\alpha,\,\delta) \tag{2.22}$$

where ϕ^{iso} is the angular-averaged isotropic flux and $I(\alpha,\,\delta)$ is the relative intensity of the flux. The anisotropy, which is the deviation from isotropy, is defined as

$$\frac{\phi(\alpha,\,\delta) - \phi^{\mathrm{iso}}}{\phi^{\mathrm{iso}}} = I - 1 \equiv \delta I \tag{2.23}$$

Because cosmic rays are continuously and randomly scattered by turbulent magnetic fields during propagation in the galactic environment, the flux is dominated by the isotropic term ϕ^{iso}. Hence, $|\delta I| \ll 1$.

The expected number of cosmic rays arriving from a direction $(\theta_i,\,\varphi_i)$ within the solid angle $\Delta\Omega$ and sidereal time interval Δt (centered on t_τ) can be expressed as [25]

$$\mu_{\tau i} \simeq I_{\tau i}\,\mathcal{N}_\tau \mathcal{A}_i \tag{2.24}$$

where

- $I_{\tau i} = I(\mathbf{R}\,(t_\tau)\,\mathbf{n}(\Omega_i))$ is the relative intensity observed in the local angular bin i during Δt;

- $\mathcal{N}_\tau = \Delta t\, \phi^{\rm iso} E(t_\tau)$ is the expected number of isotropic background during Δt;
- $A_i = \Delta\Omega\, \mathcal{A}(\theta_i,\, \phi_i)$ is the relative acceptance in the local angular bin i.

Given the expectations $\mu_{\tau i}$, the likelihood of observing a distribution of $n_{\tau i}$ events is given by the product of Poisson probabilities:

$$\mathcal{L}(n|I,\, \mathcal{N},\, \mathcal{A}) = \prod_{\tau i} \frac{(\mu_{\tau i})^{n_{\tau i}} e^{-\mu_{\tau i}}}{n_{\tau i}!} \tag{2.25}$$

Maximizing this likelihood provides estimators for the isotropic background count $\mathcal{N}_\tau$ and for the relative acceptance function $\mathcal{A}_i$.

The null hypothesis of no anisotropy corresponds to $I_{\mathfrak{a}}^{(0)} = 1$. In this case, the maximum likelihood estimators for $\mathcal{A}_i$ and $\mathcal{N}_i$ are:

$$N_\tau^{(0)} = \sum_i n_{\tau i}\ ; \qquad\qquad A_i^{(0)} = \sum_\tau n_{\tau i} \Big/ \sum_{\kappa j} n_{kj} \tag{2.26}$$

Allowing for the possibility of anisotropy entails maximizing the likelihood ratio of signal over null hypothesis

$$\lambda = \frac{\mathcal{L}(n|I,\, \mathcal{N},\, \mathcal{A})}{\mathcal{L}(n|I^{(0)},\, \mathcal{N}^{(0)},\, \mathcal{A}^{(0)})} \tag{2.27}$$

The maximum $(I^\star,\, \mathcal{N}^\star,\, \mathcal{A}^\star)$ of this equation follows the relations:

$$I_{\mathfrak{a}}^\star = \sum_\tau n_{\tau\mathfrak{a}} \Big/ \sum_\kappa \mathcal{A}_{\kappa\mathfrak{a}}^\star\, \mathcal{N}_\kappa^\star \tag{2.28}$$

$$\mathcal{N}_\tau^\star = \sum_i n_{\tau i} \Big/ \sum_j \mathcal{A}_j^\star\, I_{\tau j}^\star \tag{2.29}$$

$$\mathcal{A}_i^\star = \sum_\tau n_{\tau i} \Big/ \sum_\kappa \mathcal{N}_\kappa^\star\, I_{\kappa i}^\star \tag{2.30}$$

The binned quantity $\mathcal{A}_{\kappa\mathfrak{a}}^\star$ is the relative acceptance seen in the equatorial coordinate system in pixel $\mathfrak{a}$ during interval time Δt centered on t_κ. We have

$$\mathcal{A}_{\kappa\mathfrak{a}}^\star = \Delta\Omega_{\mathfrak{a}}\, \mathcal{A}\left[\mathbf{R}^\intercal(t_\kappa)\, \mathbf{n}(\Omega_{\mathfrak{a}})\right] \tag{2.31}$$

Relations (2.28), (2.29), and (2.30) represent a set of non-linear equations that cannot be solved explicitly. However, an iterative approach can be used to find the best-fit solutions [25]. This iterative maximum likelihood method allows to reconstruct simultaneously the background count $\mathcal{N}$, the cosmic-ray intensity I, and the relative acceptance $\mathcal{A}$ for

mid-latitude detectors where the instantaneous field of view changes rapidly.

References

[1] Y. HU and A. Lazarian, *Astrophys. J.*, vol. 943, p. 38, 2023. DOI: 10.3847/1538-4357/ad5a9b.

[2] A. H. Compton and I. A. Getting, *Phys. Rev.*, vol. 47, p. 817, 1935. DOI: 10.1103/PhysRev.47.817.

[3] S. R. Majewski, *IAU Symposium*, vol. 248, p. 450, 2008. DOI: 10.1017/S1743921308019790.

[4] L. J. Gleeson and W. I. Axford, *Astrophys. Space Sci.*, vol. 2, p. 431, 1968. DOI: 10.1007/BF02175919.

[5] K. Nagashima, K. Fujimoto, and R. M. Jacklyn, *J. Geophys. Res.*, vol. 103, pp. 17 429–17 440, 1998. DOI: 10.1029/98JA01105.

[6] M. Amenomori *et al.*, *Science*, vol. 314, p. 439, 2006. DOI: 10.1126/science.1131702.

[7] A. A. Abdo *et al.*, *Astrophysical Journal*, vol. 698, p. 2121, 2009. DOI: 10.1088/0004-637X/698/2/2121.

[8] G. Guillian *et al.*, *Phys. Rev. D*, vol. 75, no. 6, p. 062 003, 2007. DOI: 10.1103/PhysRevD.75.062003.

[9] S. cui *et al.*, *Proc. 32nd Int. Cosmic Ray Conf.*, 2011.

[10] A. U. Abeysekara *et al.*, *Astrophys. J.*, vol. 865, no. 1, p. 57, 2018. DOI: 10.3847/1538-4357/aad90c.

[11] M. Zha *et al.*, *Proc. 38th Int. Cosmic Ray. Conf.*, p. 186, 2023. DOI: 10.22323/1.444.0186.

[12] R. Abbasi *et al.*, *Astrophys. J.*, vol. 981, p. 182, 2025. DOI: 10.3847/1538-4357/adb1de.

[13] R. U. Abbasi and et al., *Physical Review D*, vol. 98, no. 2, p. 022 002, 2018. DOI: 10.1103/PhysRevD.98.022002.

[14] *Astrophys. J.*, vol. 871, p. 96, 2019. DOI: 10.3847/1538-4357/aaf5cc.

[15] R. Iuppa *et al.*, *arXiv preprint*, 2011. DOI: 10.48550/arXiv.1112.2375.

[16] M. Chakraborty *et al.*, *Astrophys. J.*, vol. 961, p. 87, 2024. DOI: 10.3847/1538-4357/ad132b.

[17] M. Aglietta *et al.*, *Astrophys. J. Lett.*, vol. 692, p. L130, 2009. DOI: 10.1088/0004-637X/692/2/L130.

[18] W. D. Apel *et al.*, *Astrophys. J.*, vol. 870, p. 91, 2019. DOI: 10.3847/1538-4357/aaf1ca.

[19] A. Abdul Halim, *Proc. 39th Int. Cosmic Ray. Conf.*, vol. PoS(ICRC2025)272, DOI: 10.22323/1.501.0272.

[20] A. Abdul Halim *et al.*, *Astrophys. J.*, vol. 976, p. 48, 2024. DOI: 10.3847/1538-4357/ad843b.

[21] D. E. Alexandreas *et al.*, *Nucl. Instrum. Meth. A*, vol. 328, p. 570, 1993. DOI: 10.1016/0168-9002(93)90677-A.

[22] R. Atkins *et al.*, *Astrophys. J.*, vol. 595, p. 803, 2003. DOI: 10.1086/377498.

[23] K. Nagashima *et al.*, *Nuov. Cim. C*, vol. 12, p. 695, 1989. DOI: 10.1007/BF02511970.

[24] R. Bonino *et al.*, *Astrophys. J.*, vol. 738, p. 67, 2011. DOI: 10.1088/0004-637X/738/1/67.

[25] M. Ahlers *et al.*, *Astrophys. J.*, vol. 823, p. 10, 2016. DOI: 10.3847/0004-637X/823/1/10.

[26] J. Linsley, *Phys. Rev. Lett.*, vol. 34, p. 1530, 1975. DOI: 10.1103/PhysRevLett.34.1530.

[27] G. Di Sciascio and R. Iuppa, 2014. DOI: 10.48550/arXiv.1407.2144.

[28] M. Amenomori *et al.*, *Astrophys. J.*, vol. 626, p. L29, 2005. DOI: 10.1086/431582.

[29] V. V. Alekseenko *et al.*, *Nucl. Phys. B - Proc. Suppl.*, vol. 196, p. 179, 2009. DOI: 10.1016/j.nuclphysbps.2009.09.032.

[30] P. Abreu *et al.*, *Astropart. Phys.*, vol. 34, p. 627, 2011. DOI: 10.1016/j.astropartphys.2010.12.007.

[31] A. Abdul Halim *et al.*, *Astrophys. J.*, vol. 976, p. 48, 2024. DOI: 10.3847/1538-4357/ad843b.

[32] A. U. Abeysekara *et al.*, *Astrophys. J.*, vol. 871, p. 96, 2019. DOI: 10.3847/1538-4357/aaf5cc.

[33] M. Ahlers, *Astrophys. J. Lett.*, vol. 886, p. L18, 2019. DOI: 10.3847/2041-8213/ab552f.

Chapter 3

The KM3NeT detectors

The Kilometre Cubic Neutrino Telescope (KM3NeT) is a research infrastructure currently under construction in the deep Mediterranean Sea [1], [2]. This state-of-the-art project is designed to explore neutrino physics as well as astroparticle phenomena and is distributed across two distinct sites, each optimized for specific scientific objectives. Both detectors capture the Cherenkov radiation produced when charged particles travel faster than the speed of light in water. In order to catch this Cherenkov light, the detector is equipped with 3-inch Photomultiplier tubes (PMTs) [3].These PMTs are arranged in a grid pattern, allowing for the precise reconstruction of neutrino events. These sites employ the same underlying technology but differ in their detector configurations and research goals.

The KM3NeT project foresees the construction of several of these detectors in the depths of the Mediterranean Sea along the southern coasts of Europe: KM3NeT-Fr (offshore Toulon, France) houses the ORCA (Oscillation Research with Cosmics in the Abyss) detector, and KM3NeT-It (offshore Portopalo di Capo Passero, Sicily, Italy) houses the ARCA (Astroparticle Research with Cosmics in the Abyss) detector. Both detectors are collecting data. KM3NeT-Gr (offshore Pylos, Peloponnese, Greece) will expand the KM3NeT Research Infrastructure in a next phase. The KM3NeT project continues the work done by the ANTARES neutrino telescope, which operated off the coast of France between 2008 and 2022. The oversight, governance and management of the implementation and operation of KM3NeT is conducted by an international collaboration with more than 68 institutions from 21 countries all over the world being involved. The KM3NeT community consists of about 360 scientists, along with engineers and technicians (Fig. 3.1).

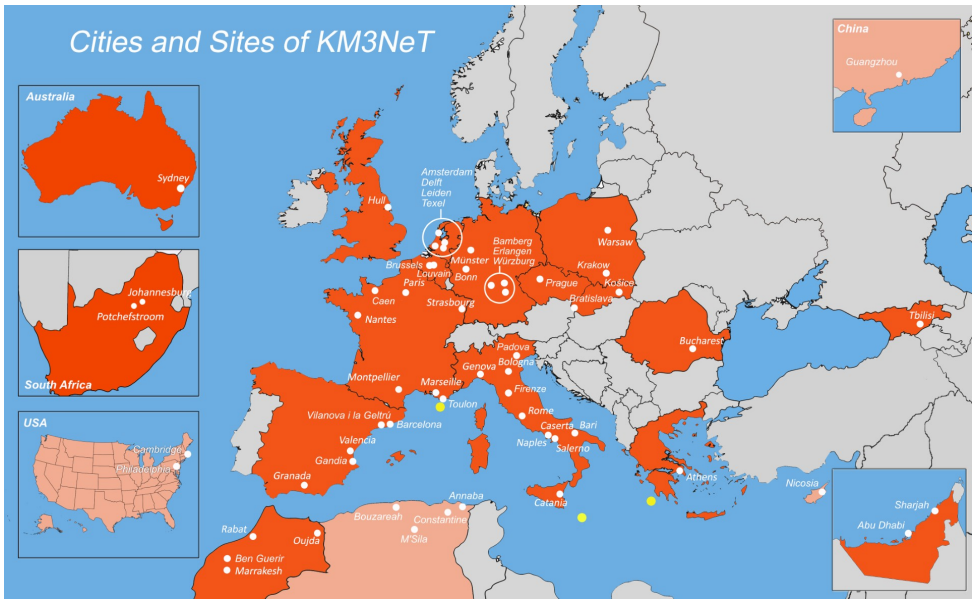

Fig. 3.1: Map showing the locations of KM3NeT collaboration institutes. Full members are indicated in bright orange whereas associated members are shown in lighter shade. The KM3NeT detectors sites are shown in yellow. Taken from the KM3NeT website https://www.km3net.org/

3.1 KM3NeT/ORCA

The ORCA (Oscillation Research with Cosmic in the Abyss) detector is located at a depth of 2450 meters near Toulon, in southern France. This site features a highly dense instrumentation layout within a 0.007 km^3 volume of water, which is optimized for the precise measurement of atmospheric neutrino oscillations. ORCA is designed to study neutrinos with energies ranging from 3 to 100 GeV. The primary goal of this detector is determining the neutrino mass ordering. Moreover, ORCA explores various phenomena beyond the Standard Model, such as non-standard neutrino interactions, Lorentz invariance violation, tau neutrino appearance, sterile neutrinos, decoherence, and invisible neutrino decay [4].

3.2 KM3NeT/ARCA

Off the coast of Sicily, Italy, is the ARCA(Astroparticle Research with Cosmics in the Abyss) detector, which is located at a depth of 3500 meters close Capo Passero. ARCA has a lower density instrumentation but spans over a larger volume. The configuration of this detector is optimized to stufdy neutrinos originating from astrophysical sources with energies in the TeV-PeV range [5]. The main goal of ARCA is to search for the sources of these high-energy neutrinos, such as AGNs, GRBs

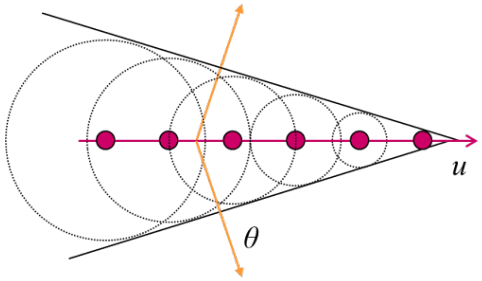

Fig. 3.2: Schematic illustration of Cherenkov radiation. Taken from [7].

3.3 Working principle

3.3.1 Cherenkov light

Water Cherenkov detectors, such as KM3NeT, detect neutrinos by measuring the Cherenkov radiation [6] emitted by charged secondary particles produced in neutrino interactions. This radiation occurs when the particle's velocity v exceeds the speed of light in the medium. The light velocity in a medium is given by c/n, where c represents the speed of light and n is the refractive index of the medium. The Cherenkov radiation occurs when the velocity a charged particle is greater than the speed of light in the medium. The interference of electromagnetic waves leads to the formation of a cone shaped wavefront which is characteristic of Cherenkov light. The angle of the cone θ is given by

$$\cos\theta = \frac{1}{\beta n}$$

where $(\beta = v/c)$. This process is illustrated in Fig. 3.2 for a highly relativistic particle $(\beta \approx 1)$. For instance, a relativistic muon travelling through ice with $n \approx 1.35$ would produce a light cone with an opening angle of approximately 42°. Particle detectors that capture the Cherenkov light emitted by relativistic charged particles can be constructed by placing light sensors in a medium that is both optically transparent and dark, such as ice or water.

3.3.2 Neutrino interaction with matter

Neutrino interactions occur via the exchange of heavy bosons (Fig. 3.3). In **charged-current (CC)** interactions, a neutrino exchanges a $W^{\pm}$ boson and is converted into its corresponding charged lepton, for example

$$\nu_\ell + N \;\rightarrow\; \ell^- + X\,.$$

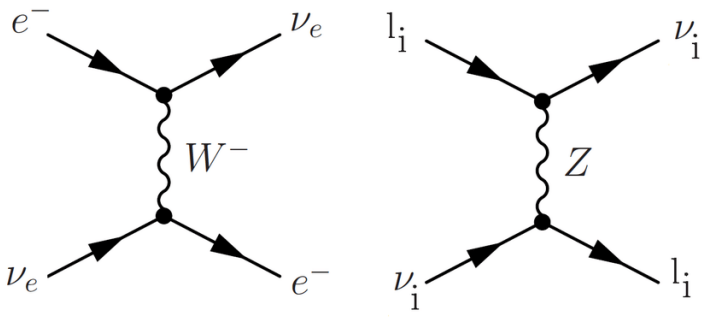

Fig. 3.3: Feynman digrams of a neutrino-electron scattering. Taken from [8].

In **neutral-current (NC)** interactions, a neutrino exchanges a Z^0 boson and remains a neutrino of the same flavor, e.g.

$$\nu_\ell + N \;\rightarrow\; \nu_\ell + X\,.$$

CC events produce charged leptons that can be directly observed in the detector, whereas NC events only leave hadronic showers, with part of the energy carried away by the outgoing neutrino.

3.4 Photomultiplier tube

A photomultiplier tube (PMT) is a device that converts photons into electrical signals (Fig. 3.4). When a photon hit the photocathode, it releases an electron via the photo-electric effect. The probability of this process depends on the quantum efficiency. These electrons are then multiplied through a series of dynodes until they reach the anode, where each collision releases more electrons, the signal is then amplified by a factor of 3 $\times 10^6$. An electrical pulse is then produced by a photon.

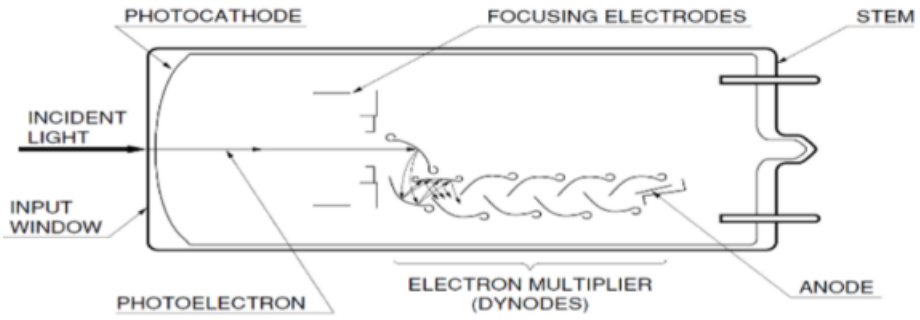

Fig. 3.4: Schematic illustration of a PMT. Taken from [9].

(a) **(b)**

Fig. 3.5: KM3NeT digital optical module. (a) fully assembled DOM. (b) DOM with the upper hemisphere removed showing the internal arrangement of PMTs. Taken from [3].

3.5 Digital optical modules

KM3NeT detectors contain an array of thousands of optical sensors designed to capture the Cherenkov light of charged particles as they propagate through sea water. These sensors are housed in pressure resistant glass spheres called Digital Optical Modules (DOMs), each with a diameter of 42 cm, capable of withstanding the extreme pressures at the depths where the detectors are deployed in the Mediterranean Sea [10]. Each DOM is equipped with 31 3-inch PMTs (Fig. 3.5), which provide a 4π signal coverage. PMTs are highly sensitive sensors that can detect single photons with nanosecond precision, making them critical for capturing the faint Cherenkov light produced by neutrino interactions. Beyond their primary light detection capability, these DOMs incorporate additional instrumentation, such as piezoelectric sensors for precise acoustic positioning, a tiltmeter/compass to monitor orientation, and a light emitting diode for accurate time and energy calibration. Other integrated electronics, including a Central Logic Board which manages data acquisition, synchronizes timing via the White Rabbit protocol, and transmits raw photon arrival times and pulse-width data to shore for analysis [11].

Calibration systems such as acoustic sensors and LED nanobeacons ensure module positioning and timing accuracy, critical for reconstructing neutrino trajectories with angular resolutions as sharp as $0.05°$. Scalable and mass produced, over 6,000 DOMs, will form KM3NeT's underwater arrays.

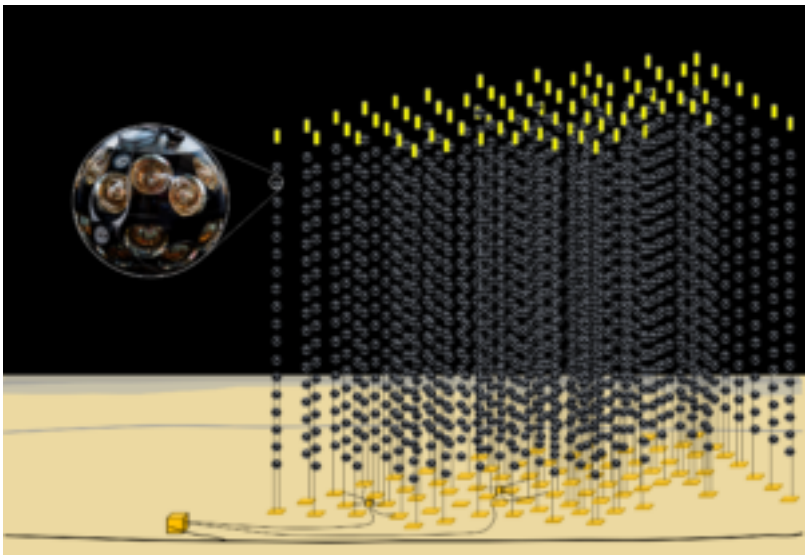

Fig. 3.6: Detailed visualization of a KM3NeT detector array showing vertical strings with optical modules. Highlighting a close up of the DOM. Adapted from the KM3NeT website:https://www.km3net.org/

3.6 Detector layout

The DOMs are arranged along vertical, flexible string-like structures known as Detection Units (DUs) (Fig. 3.6). Each DU comprises 18 DOMs, organized along two parallel, slender ropes. These units are anchored to the sea floor with weights and maintained in an upright position by the buoyancy of the DOMs, complemented by a submerged buoy at the top. This configuration ensures stability and precise positioning of the DOMs, which is crucial for accurate data collection, even in the presence of strong underwater currents.

The DOMs of ORCA are positioned 9 m apart in a vertical orientation, along with DUs that are separated by 20 m horizontally. During its final stage, it will be composed of a cylindrical structure with a radius of around 100 m and a height of roughly 115 m, leading to an instrumented volume of about 7 million metric tons. In contrast, ARCA's final configuration consists of 2 building blocks, each containing 115 DUs spaced 90 m apart horizontally. The spacing between DOMs in ARCA is 36 m creating a cubic kilometer crucial for neutrinos detectors given the small cross sections and the flux of cosmic neutrinos. A comparison between the size of ORCA and ARCA detectors is shown in the Figure 3.7. Each detector connects to the shore via one or more main electro-optical cables (MEOC) that contain a power conductor and a bundle of optical fibres for transmitting high bandwidth data over distances of approximately 100 kilometers.

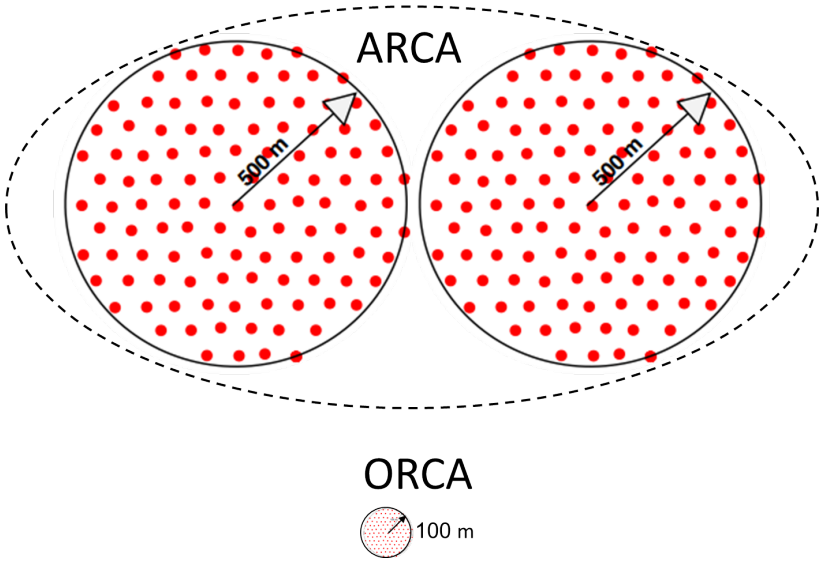

Fig. 3.7: Schematic overview of KM3NeT detectors. The building blocks of ARCA are cylindrical with a radius of 500 m. For ORCA the building block has a radius of 100 m. Adapted From the KM3NeT website: https://www.km3net.org/

3.7 PMT's characteristics

3.7.1 Quantum efficiency

Quantum efficiency (QE) is referred to as the average number of photoelectrons produced when photons hit the photosensitive plate (photocathode) divided by the number of incident photons. The QE depends on the wavelength of the incoming photons [3]. The efficiency of KM3NeT PMTs is shown in Fig. 3.8. The PMTs have a relatively low nominal gain of 3.10^6 to minimize aging effects during their 15 year projected lifetime . Operational gain is adjusted by tuning the High Voltage of each PMT, ensuring optimal quantum efficiency both in the laboratory and during telescope operation.

3.7.2 Transit time

When a photon interacts with the photocathode of a PMT, it induces the emission of an electron through the photoelectric effect. Subsequently, this initial electron is accelerated towards the dynodes within the PMT by an electromagnetic field, triggering the release of more electrons through a chain reaction [12]. Hamamatsu PMTs are equipped with ten dynodes each with increasing electric potential in order to amplify the signal through a cascade of electrons. The interactions between the electrons and the dynodes lead to the amplification of the original signal by more than 10^6 times, significantly boosting the signal intensity. The amplified electron cascade reaches the anode of the PMT producing an

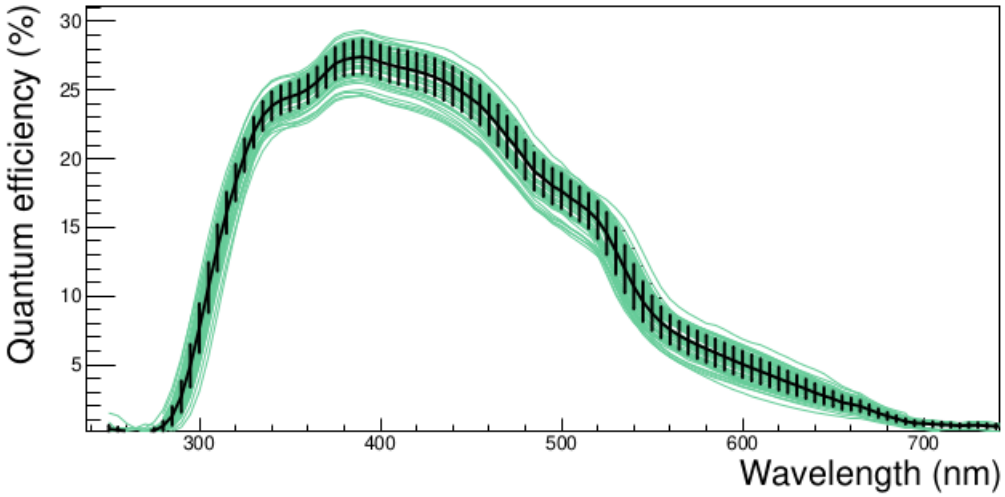

Fig. 3.8: The QE of KM3NeT PMT's shown as function of the wavelength. Each green curve represents an individual measurement from on of th 56 PMT's tested. The black curve indicate the mean value for each wavelength and the black bars represent 1 standard deviation. Taken from [12].

electrical pulse presented in Fig. 3.9, if the pulse's magnitude exceeds a predefined threshold. This threshold ensure that only signals with specific strength are captured helping to distinguish real signal from background. The interval from when the initial photon strikes the photocathode to the secondary electrons arriving at the anode is referred to as the the transit time and its value is 30 ns [13]. This nanosecond time measurement accuracy captures the time structure of photon flux accurately without distortion in the seawater.

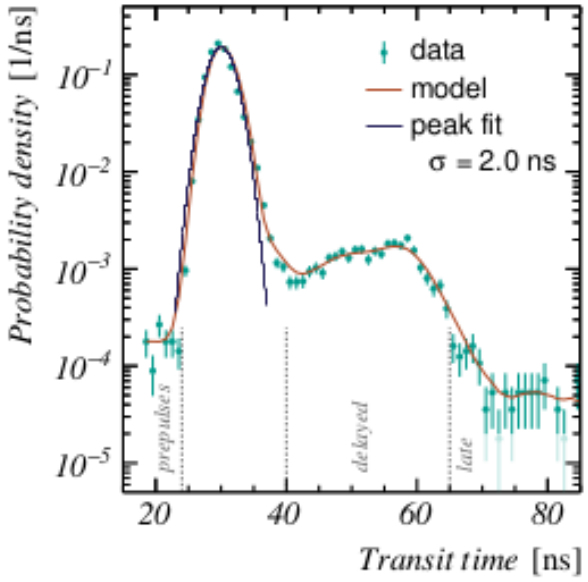

Fig. 3.9: Transit time distribution of PMTs in KM3NeT. Taken from [14].

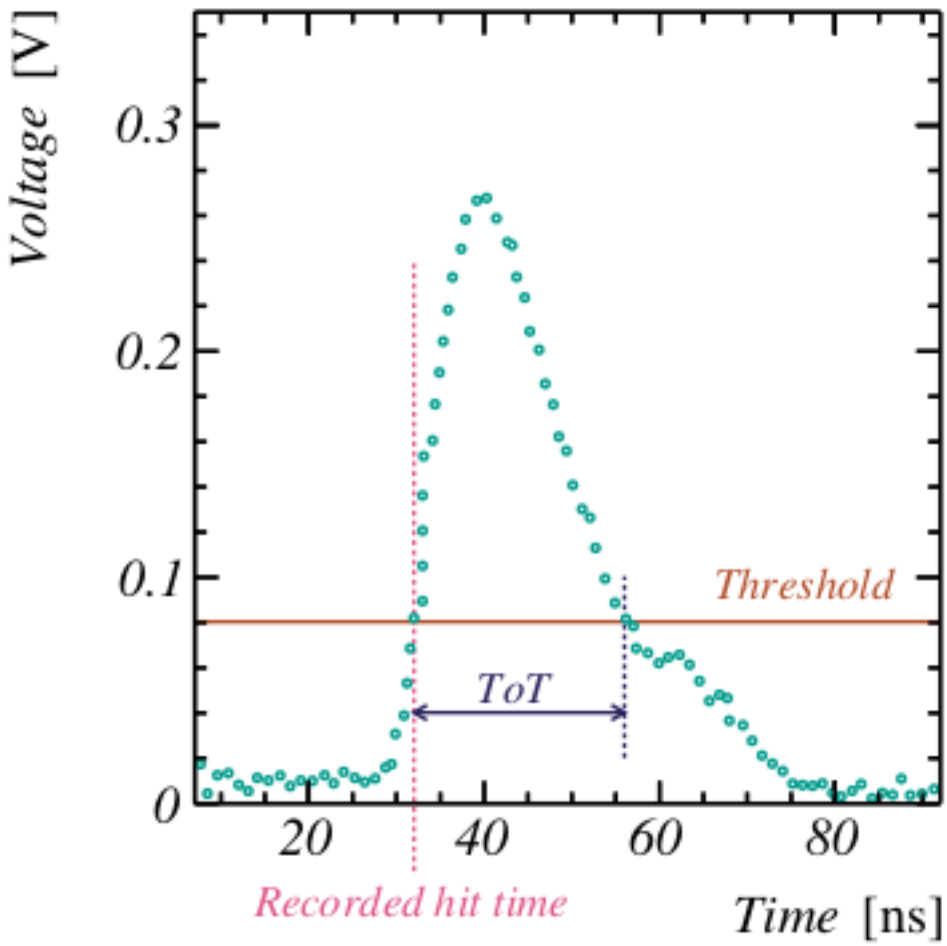

Fig. 3.10: Recorded pulse in a PMT. Adapted from [14]

3.7.3 Time over threshold (ToT)

The ToT measures the duration for which the pulse remains above the threshold level (Fig. 3.10). This duration, or time over threshold, correlates with the amount of charge collected, which can be related to the number of incident photons or the energy of the detected event. Information from PMT photon measurements is encoded with arrival time and pulse width using the ToT technique, which reduces the required bandwidth while providing sufficient data for signal analysis .

3.8 Optical background

The various origins of background for the KM3NeT detectors are outlined in the following section, as the generation of light underwater is not solely due to neutrino interactions.

3.8.1 Bioluminescence

Certain marine organisms produce lights via a chemical reaction within their bodies. This phenomena is known as bioluminescence . This is common in deep seas and involves a variety of organisms such as algae, jellyfish, worms, sea stars... Bioluminescence presents a significant optical background for deep sea water Cherenkov detectors detectors. To address noise background, a high rate veto mechanism is employed. This mechanism is triggered if the hit rate in a PMT exceeds a predetermined threshold of 20 kHz. When the HRV is activated, any data recorded on the affected PMT is discarded until the hit rate falls below the threshold again. This prevents bioluminescent signals, which can be much more intense than the desired neutrino interactions, from contaminating the data. The veto remains in effect until the PMT's count rate decreases below the 20 kHz threshold. This ensures that the data stream sent to shore is free from these intense bioluminescent bursts and clean for the detection of neutrino interactions.

3.8.2 K^{40} radioactive decay

One of the main sources of background light in KM3NeT detectors is the natural radioactivity of the potassium-40 (^{40}K) which is present in seawater. The ^{40}K isotope mostly decays into calcium-40 (^{40}Ca) releasing an electron and antineutrino. The produced electron has a maximum energy of 1.31 MeV. At these energies the electron emits Cherenkov light which is capable of triggering the detector. Specifically, a constant background of Cherenkov photons in every photomultiplier tube (PMT) is produced. While it's "noise" for physics analyses, it's actually very useful in terms of calibrating the response of the PMTs. A typical rate of about $6-8$ kHz (including the dark count rate) of hits per PMT is observed.

3.9 Atmospheric muons in KM3NeT

In KM3NeT, the majority of detected events are atmospheric muons produced in extensive air showers following the interaction of CRs with the atmosphere. While these muons constitute an irreducible background for neutrinos astronomy, they also present a valuable tool to study cosmic ray flux and for testing hadronic interaction models. Fig. 3.11 presents the atmospheric muon flux observed in KM3NeT/ ARCA detector with its 6 DU's configuration at energies above the TeV range.

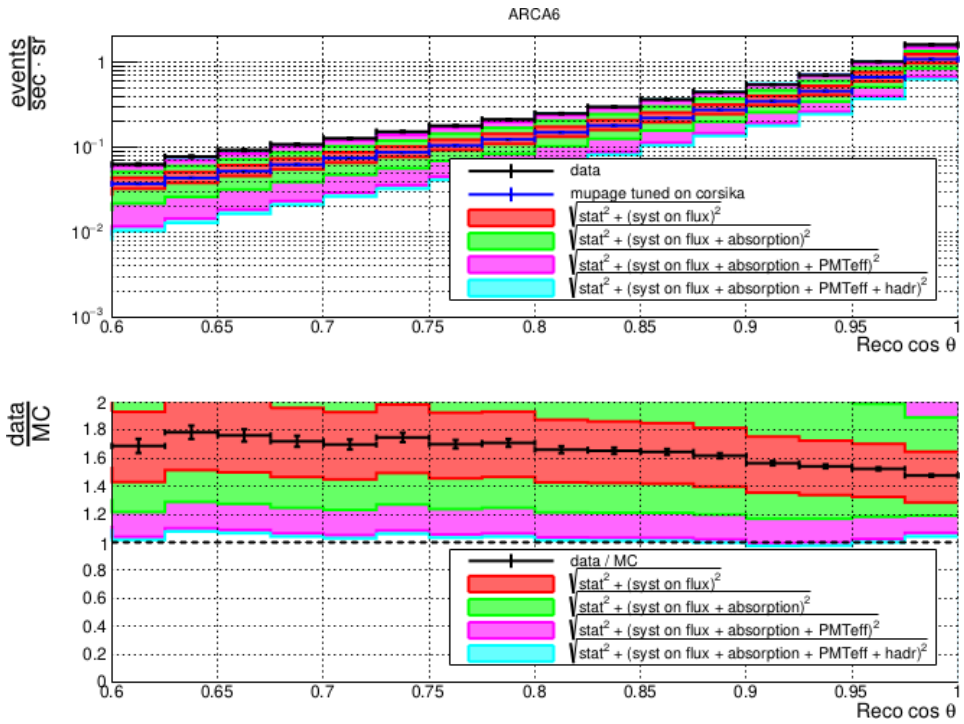

Fig. 3.11: Comparison of the simulated atmospheric muon flux with data from 6 DUs of ARCA. Top plot shows the event rates and bottom plot the data simulation ratio. The simulated flux underestimates the atmospheric muon flux. Taken from [15].

3.10 Calibration

Accurate reconstruction of neutrino events relies on the precise determination of the position and orientation of the optical modules, which are responsible for detecting Cherenkov radiation. Due to the movement of the detector elements caused by deep-sea currents, continuous tracking of their positions and orientations is necessary. The positions of the optical modules are determined using a network of acoustic emitters and receivers, while their orientations are measured using compasses embedded within each module. To achieve the target angular resolution of 0.05 degrees for the KM3NeT/ARCA telescope, the positions of the optical modules must be determined with a resolution of 20 cm. Furthermore, the orientations of the modules must be resolved with an accuracy of around 3 degrees and a PMT time offset of 1 ns to ensure the quality of event reconstruction remains uncompromised [16]. The detection unit is anchored to the seafloor and stabilized by buoys. The tilt angles, defined as the angles between the detection unit and a vertical reference string, quantifies DU deviation caused by sea currents (Fig. 3.12). The latter are dynamically calibrated every 10 minutes using acoustic data to model DU curvature caused by sea currents. The absolute pointing of the detector is derived by obtaining the absolute positions ot the DOMs, using the absolute position of each acoustic emitter and the latter are established after sea operations.

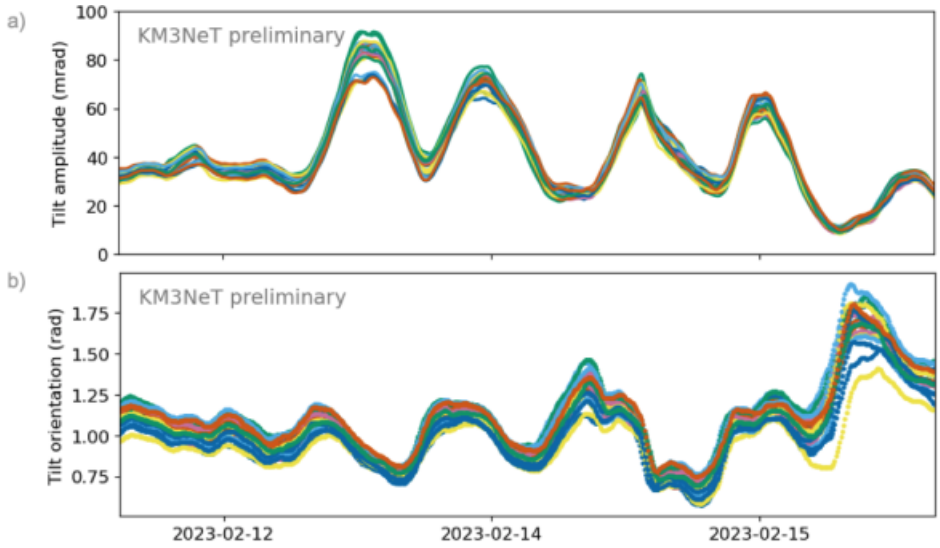

Fig. 3.12: (a) Tilt amplitudes; (b) Tilt orientation for a period of few days for ARCA 21 detector. Different curves represent different detection units. Taken from [16].

- **Intra-PMT**
  If the PMTs are perfectly calibrated, the rate of coincidences from ^{40}K should be maximized. At this calibration level, the ^{40}K is used to synchronize the PMTs within each DOM.

- **Inter-DOM**
  At this level, the calibration relies on the relative time between DOMs within the same DU, which is called inter-DOM. To begin, a laser is used to illuminate two reference PMTs in each DOM in a dark environment, allowing for a first estimate. The use of atmospheric muon tracks and optical beacons, more especially nanobeacons, allows for in-situ confirmation.

- **Inter-DU**
  Inter-DU calibration guarantees that all detection units in the KM3NeT array are time-synchronized. Before deployment, laboratory and infrastructure experiments are conducted to determine the initial deviations. The timing is cross-checked in situ using atmospheric muons and light from laser beacons.

Another method to calibrate the detector make use of the Sun and Moon shadows. As cosmic rays propagate towards Earth, some of them are blocked by the Moon or the Sun, producing a small but measurable deficit in the muon flux (Fig. 3.13). This can be used in order to verify the absolute pointing of the detector. Details of the analysis can be found here [17].

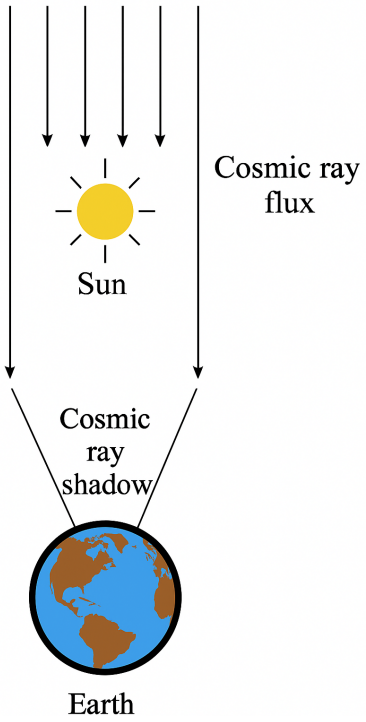

Fig. 3.13: Illustration of the cosmic ray shadow caused by the sun.

3.11 Event topology

Different kinds of particles interacting inside the detector produce various event signatures, which represent the particle's physical properties and interaction mechanisms (Fig. 3.14).

3.11.1 Track-like events

Track-like events are caused by muons travelling across the detector's sensitive volume. Among them, the most significant for neutrino investigations are muon tracks originating from charged-current (CC) interactions of muon neutrinos and antineutrinos. These events may be reconstructed with great angular accuracy because of the longer muon path through the detector and the significant Cherenkov radiation released, which is detected by a large number of PMTs. However, energy reconstruction is significantly less precise since the complete energy of the entering particle is not always deposited inside the instrumented volume. In addition to neutrino induced muons, atmospheric muons leave track-like signatures in the KM3NeT telescopes. The fundamental goal of this thesis is to characterise and analyse these atmospheric muon directions. The first and last panels in Fig. 3.14 provide examples of track-like event topologies.

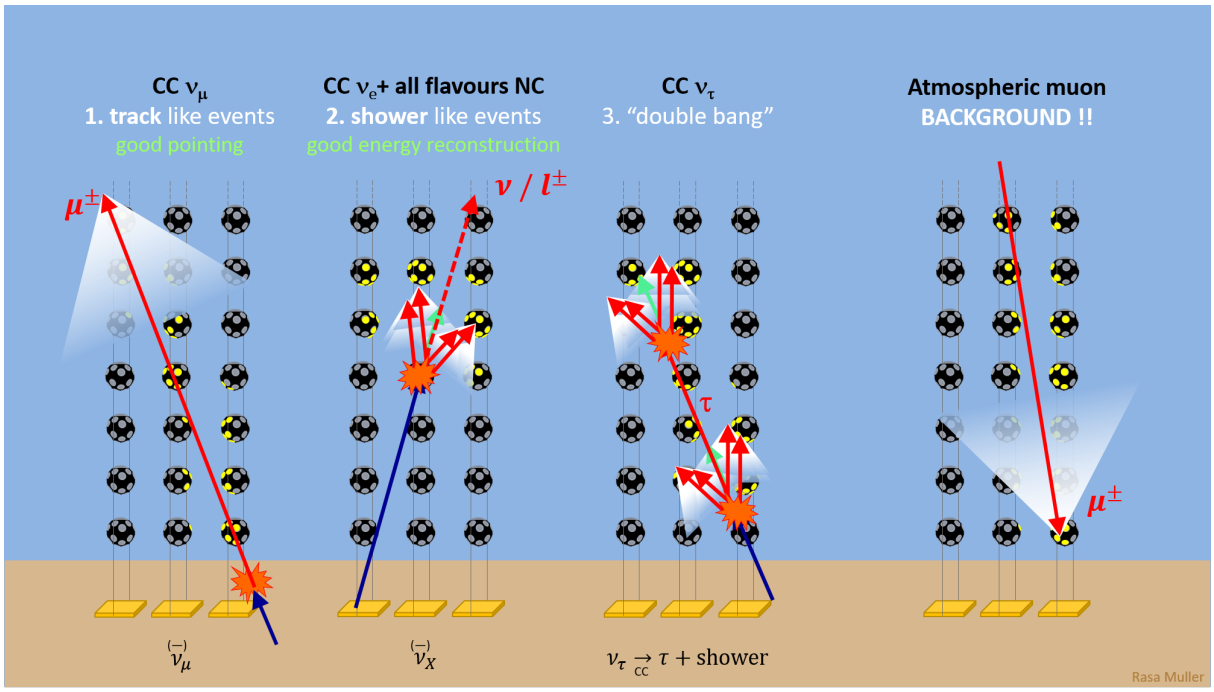

Fig. 3.14: Topologies of the events detected in KM3NeT detectors.

3.11.2 Shower-like events

Shower-like (cascade-like) events primarily arise from neutral-current (NC) interactions of neutrinos across all three flavours, in addition to charged-current (CC) interactions involving electron neutrinos. In both interaction types, the resulting hadronic cascade produces an electromagnetic shower that emits Cherenkov light, which is detectable by PMTs. These events facilitate precise energy reconstruction, as the energy deposition generally remains entirely contained within the detector's instrumented volume. Nonetheless, the directional reconstruction exhibits lower precision in comparison to track-like events, as the emitted light typically activates only adjacent digital optical modules (DOMs).

A specific category of events emerges from the charged-current interactions of high-energy tau neutrinos (PeV scale) with matter, leading to a distinctive double-cascade (or double-bang) signature [18]. The initial CC interaction results in the production of a tau lepton and a corresponding hadronic cascade. The tau lepton propagates a measurable distance through water, approximately 50 meters for a 1 PeV tau lepton prior to decaying into a second cascade. When the distance between the two cascades is sufficiently large, the detector can distinguish them as two separate light emission regions, facilitating the identification of a double-bang event.

3.12 Data Acquisition

The KM3NeT experiment employs an advanced Data Acquisition (DAQ) system based on the "all-data-to-shore" concept. In this approach, the filtering and selection of physics events occur in real time using software onshore. The detection of a photon by a PMT generates an L0 hit, which includes the signal crossing time and the time over threshold (ToT) that quantifies the signal amplitude. When at least two L0 hits occur within a time window of 25 ns on the same DOM, an L1 hit is formed. The coincidence of two L1 hits or more in an opening angle between the PMTs of 180° results in an L2 hit. Data acquisition is organized into time slices and summary slices recorded every 100 ms. Time slices capture all hits detected within this interval, while summary slices provide detector status, including module identifiers, PMT rates, and system health indicators like high-rate vetoes or synchronization errors. An event is a set of causally related hits generated when one of the triggers is fired. Multiple trigger algorithms operate concurrently on the L2 data to identify signatures of neutrino interaction products. These events record all related hits and include additional snapshots of the detector's activity before and after the trigger, enabling detailed analyses of the signals [19].

3.13 Current status of ARCA detector

A very successful sea campaign has taking place in last June at the KM3NeT ARCA site. Throughout the operation, 18 new detection units were deployed alongside a new acoustic long baseline positioning system. ARCA has been expanded to incorporate 51 deployed detection units, which are linked to the shore via a network consisting of two long-distance electro-optical cables and five submarine junction boxes.

3.14 Very high energy event

On the 12th February 2023, a total of 3672 photomultiplier tubes (about 30%) were triggered in the ARCA detector then, operating in its 21 DUs configuration [20]. This corresponds to the highest energy event ever observed. The estimated energy of 120 PeV corresponds to a muon produced by the interaction of a muon neutrino near the detector, leaving a clear track signature as it traversed its vicinity. The energy of the parent neutrino is estimated to have a median energy about 220 PeV in 90% confidence interval of 72 PeV – 2.6 EeV.

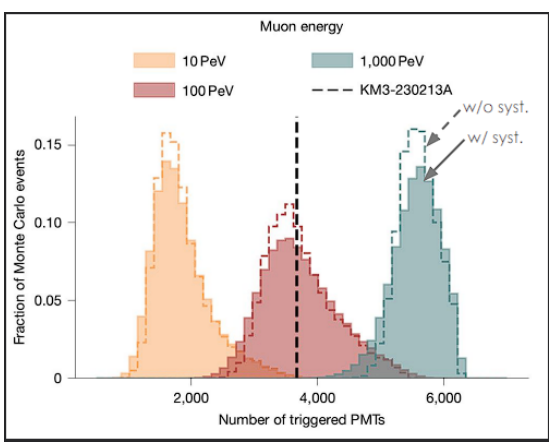

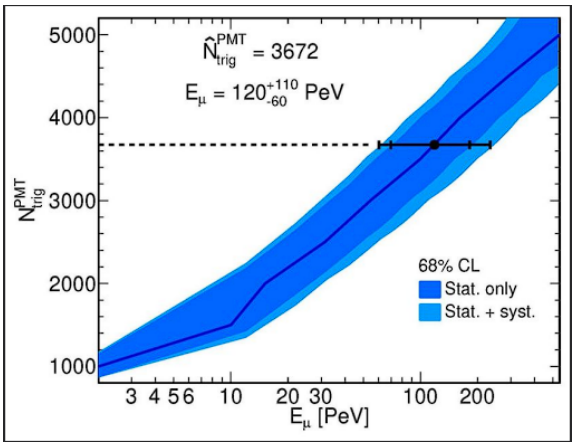

Fig. 3.15: The figure on the left shows the number of triggered PMTs involved in the event. The dashed line corresponds to the 3672 triggered PMTs. On the right, the true muon energy maximizing the log likelihood for a specific number of triggered PMTs. Taken from [20].

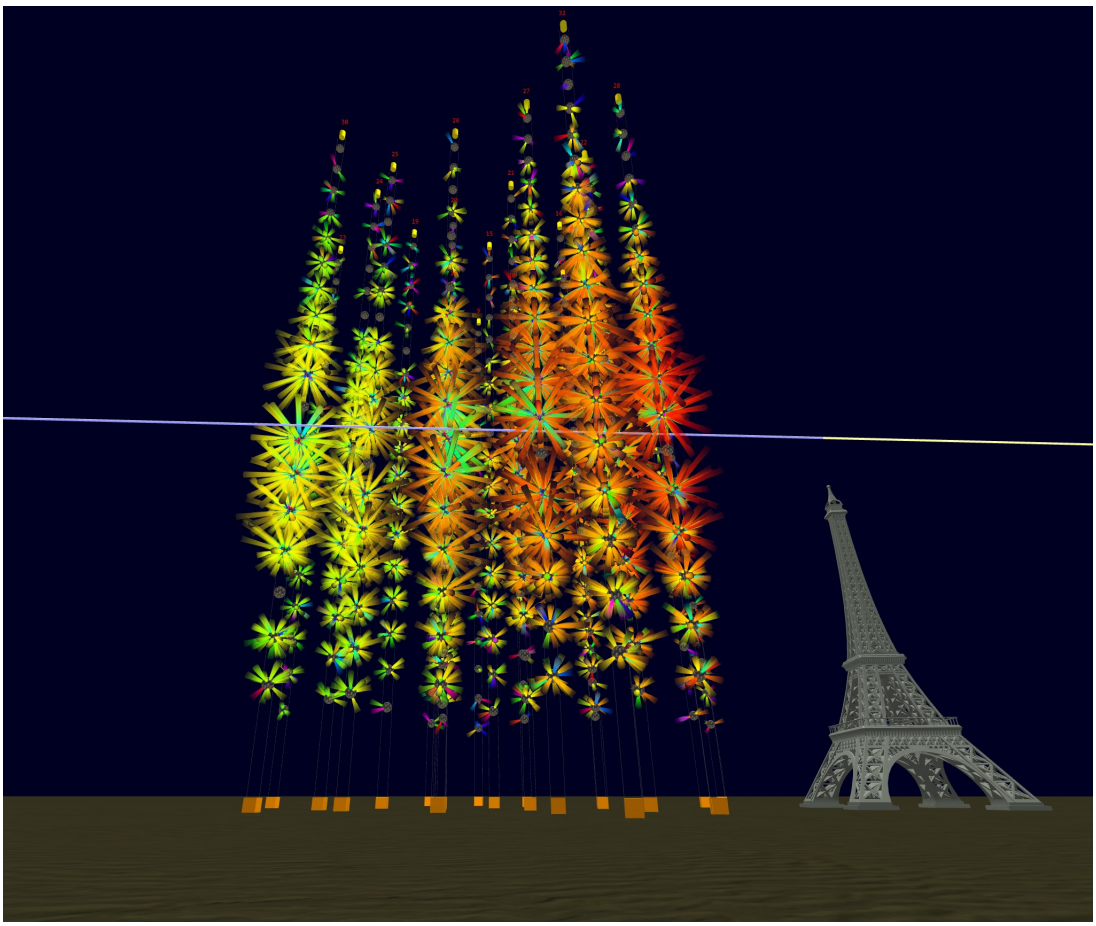

Fig. 3.16: Artistic representation of the very high energy event detected by ARCA.

References

[1] S. Adrian-Martinez *et al.*, *J. Phys. G: Nucl. Part. Phys.*, vol. 43, p. 084 001, 2016. DOI: 10.1088/0954-3899/43/8/084001.

[2] M. Sanguineti, *Il Nuovo Cimento C*, vol. 46, no. 1, p. 1, 2023. DOI: 10.1393/ncc/i2023-23004-3.

[3] S. Aiello *et al.*, *J. Instrum.*, vol. 17, no. 07, P07038, 2022. DOI: 10.1088/1748-0221/17/07/P07038.

[4] S. Aiello *et al.*, *Eur. Phys. J. C*, vol. 82, no. 1, p. 26, 2022. DOI: 10.1140/epjc/s10052-021-09893-0.

[5] S. Aiello *et al.*, *Astropart. Phys.*, vol. 111, p. 100, 2019. DOI: 10.1016/j.astropartphys.2019.04.002.

[6] P. Cerenkov, *Phys. Rev.*, vol. 52, no. 4, p. 378, 1937. DOI: 10.1103/PhysRev.52.378.

[7] H. Alaeian, *An introduction to cherenkov radiation*, Submitted as coursework for PH241, Stanford University, 2014.

[8] D. Bolognini *et al.*, *Nucl. Instrum. Methods Phys. Res. A*, vol. 646, no. 1, p. 108, 2011. DOI: 10.1016/j.nima.2011.05.008.

[9] Hamamatsu Photonics, *Photomultiplier Tubes: Principle and Applications*. Hamamatsu Photonics K.K., 2002.

[10] R. Bruijn and D. van Eijk, *Proc. 31th Int. Cosmic ray. Conf., the Hague, the Netherlands,*, p. 1157, 2015. DOI: 10.22323/1.236.1157.

[11] S. Aiello, *J. Astron. Telesc. Instrum. Syst.*, vol. 5, p. 046 001, 2019.

[12] S. Aiello *et al.*, *JINST*, vol. 13, P05035, 2018. DOI: 10.1088/1748-0221/13/05/P05035.

[13] S. Aiello *et al.*, *JINST*, vol. 17, p. 07 038, 2022. DOI: 10.1088/1748-0221/17/07/P07038.

[14] K. W. Melis, "Studying the universe from -3000m n.a.p.," PhD thesis, Ph.D. dissertation, Amsterdam University, 2021.

[15] A. Romanov, "Cosmic ray studies with the km3net neutrino telescope," PhD Thesis, 2023.

[16] C. G. Oliver *et al.*, *Proc. 38th Int. Cosmic Ray. Conf.*, PoS(ICRC2023)1033, 2023. DOI: 10.22323/1.444.1033.

[17] S. Aiello *et al.*, *Eur. Phys. J. C*, vol. 83, no. 4, p. 344, 2023. DOI: 10.1140/epjc/s10052-023-11401-5.

[18] J. G. Learned and S. Pakvasa, *Astropart. Phys.*, vol. 3, p. 267, 1995. DOI: 10.1016/0927-6505(94)00043-3.

[19] O. Adriani *et al.*, *arXiv preprint arXiv:2506.05881*, 2025. arXiv: 2506.05881 [astro-ph.IM].

[20] S. Aiello *et al.*, *Nature*, vol. 638, p. 376, 2025. DOI: 10.1038/s41586-024-08543-1.

Chapter 4

Simulation

This chapter introduces common tools to generate atmospheric muons at sea level and to propagate them through seawater, and the software employed in KM3NeT simulations.

4.1 CORSIKA

CORSIKA (COsmic Ray Simulations for KAscade) [1] is an advanced Monte Carlo simulation program originally developed for the KASCADE experiment in Karlsruhe. Its purpose is to study extensive air showers (EAS) generated by high-energy CRs. The program provides a detailed physics-based simulation of the development of particle cascades in the Earth's atmosphere tracking the process from the first interaction of primaries (protons, nuclei, and photons) to the produced secondary particles reaching ground level.

CORSIKA has become a standard tool in the cosmic-ray community, widely used by experiments covering the full energy spectrum, from Cherenkov telescope arrays operating at TeV energies to ultra-high-energy cosmic ray observatories above EeV scales. The design philosophy extends past merely delivering precise mean values of key observables, including particle multiplicities and spatial distributions. CORSIKA effectively captures the intrinsic fluctuations in the development of extensive air showers, making it an indispensable tool for both the interpretation of experimental data and the optimization of detector design. CORSIKA can simulate showers initiated by a wide range of primaries, including photons, protons, light and heavy nuclei up to iron ($A = 56$), and other particles. The primary energy can be fixed or sampled from a specified energy spectrum with a given spectral index to simulate realistic flux conditions. The zenith and azimuth of the events which constitute their arrival direction can also be fixed or randomly sampled to simulate an isotropic flux.

The code tracks over 50 different types of particles through the atmosphere, accounting for several key processes, such as the ionization energy loss, which is described by the standard Bethe-Bloch formula for charged particles, the multiple Coulomb scattering and the deflection in magnetic fields. Hadronic interactions at high energies in CORSIKA are simulated using different models, namely, EPOS-LHC [2], SIBYLL 2.3d [3], QGSJEt-II.04 [4] and DPMJET III [5], whereas low energy hadronic interactions, i.e., less than 80 GeV, are simulated using the URQMD model [6]. This refers to the classic Fortran-based version of the program, CORSIKA 7, which served as the community standard for many years [7], [8], before the advent of CORSIKA 8 [9].

CORSIKA 8 is not just an update, but a complete rewrite in a modern, modular C^{++} framework that greatly expands what can be simulated compared to its predecessor. While CORSIKA 7 was limited to a fixed atmospheric setup, CORSIKA 8 gives users the flexibility to choose and adapt the atmospheric model and even to follow particle cascades as they pass from air into other media, such as ice or water. The hadronic interaction models EPOS-LHC, Sibyll 2.3d, and QGSJet-II.04, which were already present in CORSIKA 7, are also included in CORSIKA 8, but here they are implemented as modular components. In addition, the older EGS4 has been replaced by the more advanced PROPOSAL package [10]. These developments not only improve the accuracy of simulations but also open up entirely new applications, particularly for experiments that rely on neutrino detection or radio emission studies across different media.

One of the interesting quantities that can be simulated by CORSIKA is the depth of shower maximum, $X_{\max}$ defined as the atmospheric depth (in g/cm^2) at which the number of charged particles in the cascade reaches its maximum. CORSIKA samples the longitudinal profile of all charged particles, $N(t)$ as a function of the atmospheric depth T (g/cm^2). The sampled profile is fitted to an empirical function which is implemented in the code and given by:

$$N(T) = N_{\max}\left(\frac{T - T_0}{T_{\max} - T_0}\right)^{\frac{T_{\max}-T}{a+bT+cT^2}} . \tag{4.1}$$

The fit returns the following parameters: $N_{\max}$, T_0, $T_{\max}$, a, b, c and the fit quality (χ^2/d.o.f).

Another approach is used to describe the longitudinal profile and to extract the value of $X_{\max}$, the Gaisser–Hillas parametrization [11], which is widely used experimentally. The Gaisser–Hillas parametrization is given by:

$$N(X) = N_{\max}\left(\frac{X - X_0}{X_{\max} - X_0}\right)^{\frac{X_{\max}-X_0}{\lambda}} \exp\left(\frac{X_{\max} - X}{\lambda}\right), \tag{4.2}$$

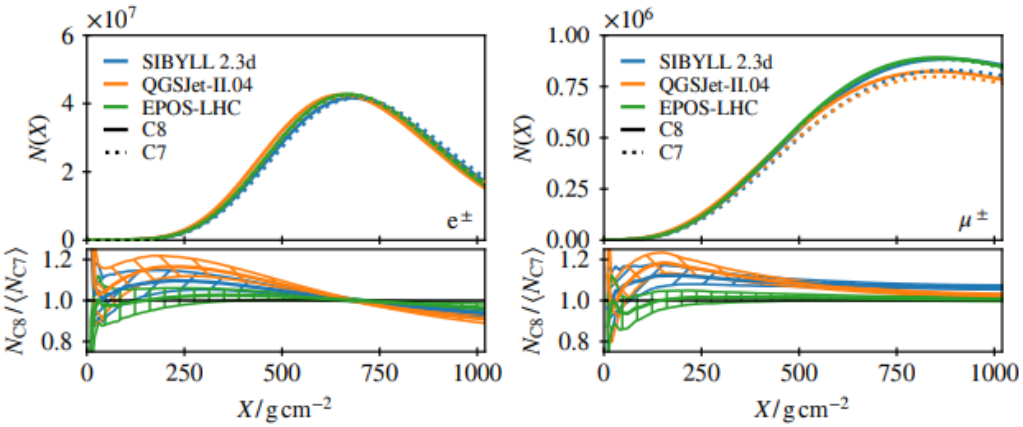

Fig. 4.1: Comparison of average longitudinal shower profiles for electrons/positrons (left) and muons (right) from vertical proton-induced air showers at a primary energy of 10^{17} eV. Results from CORSIKA 8 (solid lines) and CORSIKA 7 (dotted lines) are shown. The lower panels display the ratio of CORSIKA 8 to the mean prediction of CORSIKA 7, illustrating agreement at the $\sim 10\%$ level across models. Taken from [9].

Here the free parameters are typically $N_{\max}$, X_0, $X_{\max}$ and λ. The fitted $X_{\max}$ from this function is the standard definition used by fluorescence detectors and many hybrid experiments because it maps directly onto the energy-deposit signal used in these experiments. In CORSIKA 8, the longitudinal profile is likewise produced and the user fits the longitudinal profile externally, for instance by applying the Gaisser-Hillas parametrization. A direct comparison of the performance of CORSIKA7 and CORSIKA8 in extracting longitudinal shower profiles is shown in Fig. 4.1.

4.2 PROPOSAL

PROPOSAL (Propagator with Optimal Precision and Optimized Speed for All Leptons) is a Monte Carlo simulation tool designed to model the propagation of high-energy leptons through matter and now supports other particles like photons and even hypothetical particles such as supersymmetric sleptons. The program was created to accurately and efficiently simulate the propagation of muons and taus, which are crucial particles in large-volume detectors. PROPOSAL has evolved into modular software library accessible in both C++ and Python formats. A major design principle behind PROPOSAL is to strike a careful balance between physical realism and computational speed, a necessity in large experiments like IceCube and KM3NeT, where vast amounts of data must be simulated over volumes as large as a cubic kilometer. To meet this challenge, the software includes advanced models for the main energy loss processes (ionization, bremsstrahlung, pair production, and photonuclearinteractions), along with important corrections such as the Landau–Pomeranchuk–Migdal (LPM) effect [12], [13] and multiple scattering based on both Molière theory [14] and Highland's approximation [15].

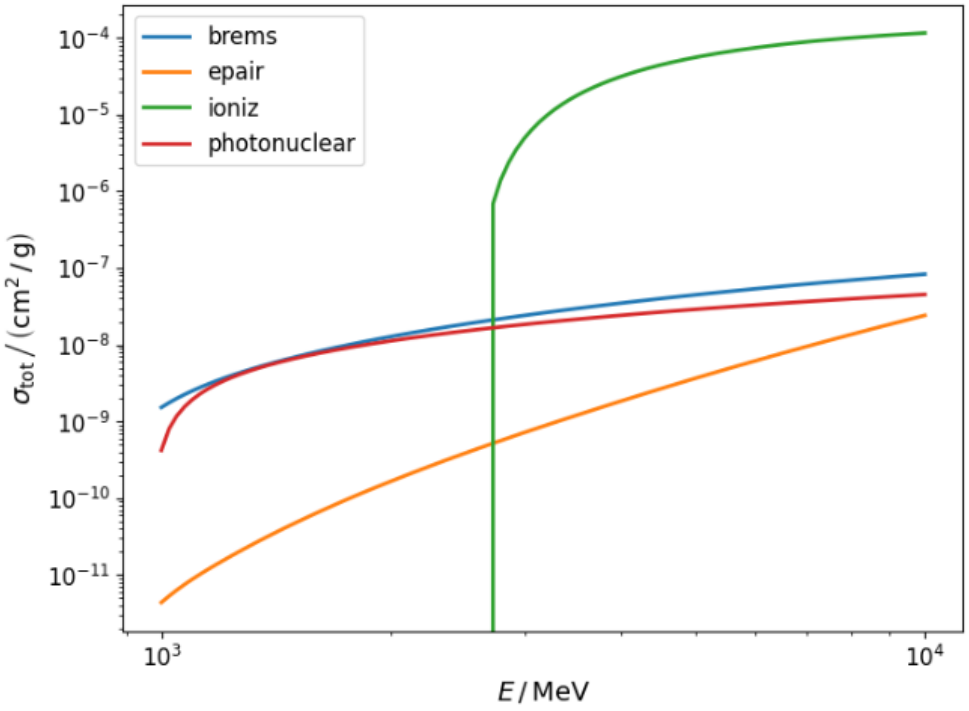

Fig. 4.2: Energy dependence of muon interaction cross sections in seawater. The contributions from bremsstrahlung, pair production, ionization, and photonuclear interactions are shown as a function of muon energy.

The average energy loss of a muon with energy E can be expressed as:

$$-\left\langle \frac{dE}{dx} \right\rangle = a(E) + b(E)\, E, \tag{4.3}$$

where $a(E)$ represents the continuous ionization losses and $b(E)\,E$ accounts for the radiative processes (bremsstrahlung, electron–positron pair production, and photonuclear interactions). For muons in water, the ionization term is approximately constant with

$$a(E) \simeq 2 \text{ MeV cm}^2/\text{g},$$

while the radiative term is much smaller at low energies but grows with energy, with

$$b(E) \sim 4 \times 10^{-6} \text{ cm}^2/\text{g}.$$

The crossover between these regimes occurs around the *critical energy* $E_c \approx 500$ GeV, below which ionization dominates and above which radiative processes dominate.

PROPOSAL is now also implemented in CORSIKA 8 as a modern electromagnetic shower module, replacing the older EGS4 routines and allowing for more detailed step-by-step shower development. Fig. 4.2 and 4.3 show the performance of PROPOSAL in modelling the different interactions occurring when a muon propagates through sea water.

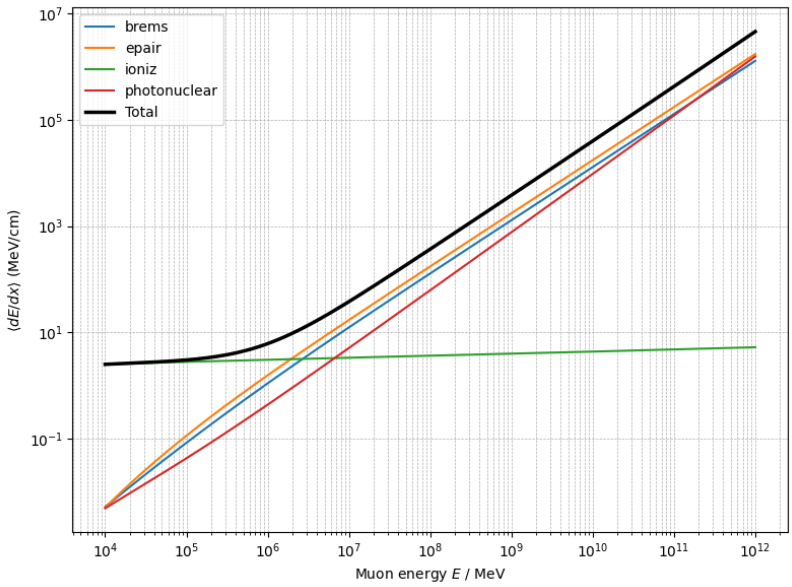

Fig. 4.3: Average energy loss of muons in seawater as a function of their energy, computed with PROPOSAL. Contributions from individual processes are shown: bremsstrahlung (blue), electron–positron pair production (orange), ionization (green), and photonuclear interactions (red). The thick black line indicates the the sum of all processes.

4.3 Event generation in KM3NeT

In KM3NeT, neutrino interactions are generated within a *generation volume* surrounding the detector. The light from these interactions is simulated inside a region called the *can*, shown in Fig. 4.4. The can is defined as a cylinder around the instrumented volume, extended by about four light absorption lengths in water, so that any photons capable of reaching the detector are included. For ARCA21, the can has a radius of about 600 m, while for a complete building block it extends to roughly 900 m.

The required size of the generation volume depends on the type of secondary particles produced:

- For **shower-like interactions** (e.g. ν_e CC, all-flavor NC), the light is confined near the interaction point, so the generation volume coincides with the can.
- For **track-like interactions** (e.g. ν_μ CC, ν_τ CC), the produced muon or tau can travel kilometers through water, so the generation volume must extend well beyond the can to account for such long-range particles. Specifically, the generation volume in this case is a cylinder made of a layer of sea water and a layer of rock separated by the sea bed, presented in Fig.4.5. Its radius is then extended by the muon maximum range in water and the rock layer has a height of the maximum of the muon range in that medium [16].

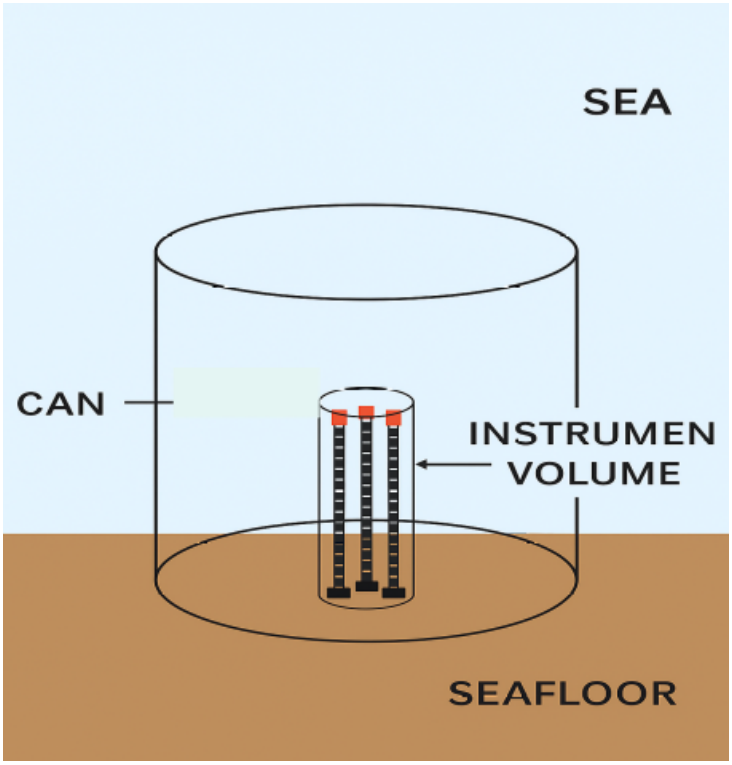

Fig. 4.4: Schematic view of the instrumented volume and the can volume.

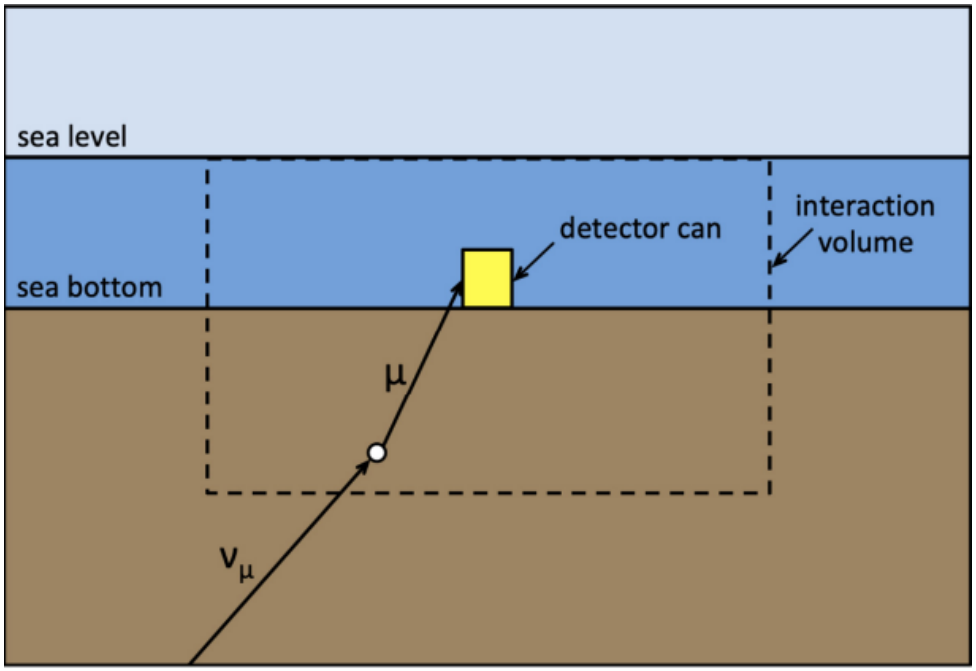

Fig. 4.5: Schematic view of the generation volume for track-like events. Taken from [16].

4.3.1 Atmospheric muon generation

A realistic way to simulate atmospheric muons generated in cosmic-ray air showers is to use a full air-shower code such as CORSIKA. However, this approach is extremely time consuming and computationally expensive, especially for cubic-kilometer detectors like KM3NeT, where an enormous number of atmospheric muons must be generated. For this reason, the MUPAGE package [17] is used as a fast and efficient alternative that still preserves the essential physical realism.

MUPAGE is capable of generating both single atmospheric muons and muon bundles, which are an important component of the background in deep-sea neutrino telescopes. It relies on parametric models derived from detailed Monte Carlo simulations of cosmic-ray showers and constrained by underground and underwater experimental data. These parameterizations describe the muon flux as a function the zenith angle, the detector depth, the multiplicity of muons in a bundle, and the radial distance of each muon from the bundle axis.

In practice, atmospheric muons in KM3NeT are generated at the edge of the can volume, where the kinematic properties of each muon are sampled from the parametric formulas and their arrival times are assigned consistently. To save the computational time, an energy threshold to the generated bundles in current KM3NeT simulations is set at 100 GeV, ensuring that the majority of detectable muons are included. For full KM3NeT detector studies focusing on high-energy neutrino searches, higher thresholds of 10 TeV and 50 TeV are applied.

At the same time, work is ongoing in the collaboration to make the simulations even more realistic. MUPAGE is currently being tuned against CORSIKA simulations in KM3NeT. The idea is to adjust the MUPAGE parametrisations so that they reproduce as closely as possible the CORSIKA predictions for the muon flux. Fig. 4.6 and 4.7 show the outcome of this tuning.

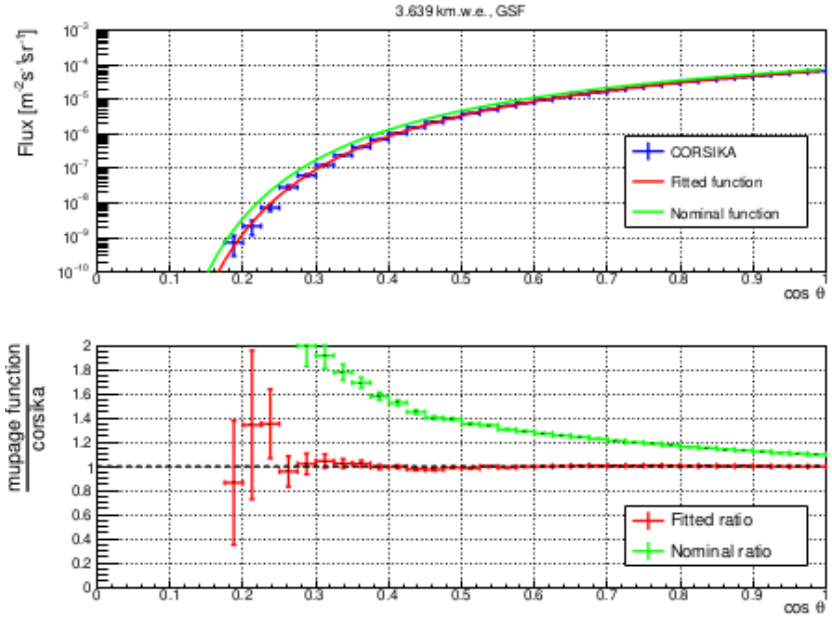

Fig. 4.6: Ratio of single muon zenith flux from CORSIKA simulations, with respect to the nominal and fitted MUPAGE functions for ARCA's detector depth. The largest discrepancy is observed at very inclined muons. Taken from [18].

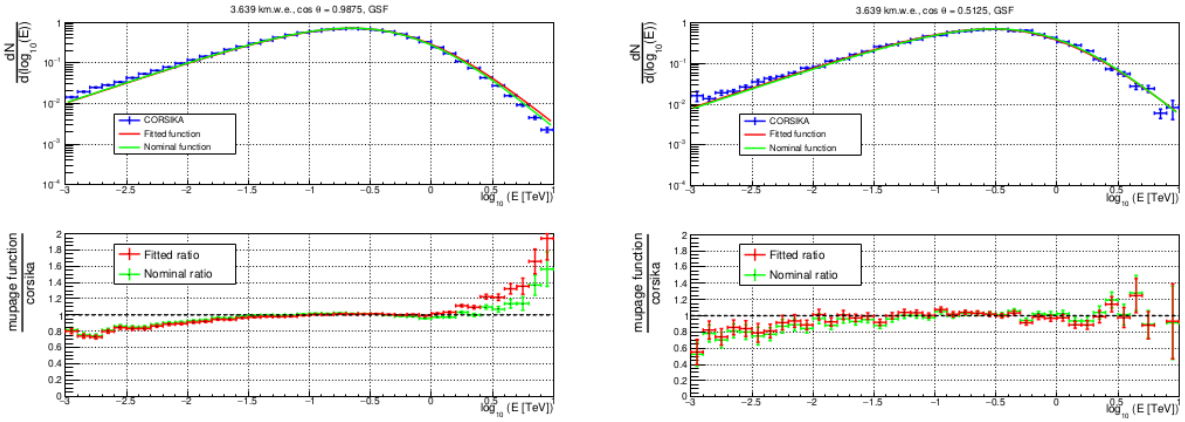

(a) **(b)**

Fig. 4.7: Energy spectrum of vertical muons from CORSIKA simulations compared to the nominal and fitted MUPAGE functions (left). Ratio of energy distribution using CORSIKA and MUPAGE functions at ARCA's depth (right). Taken from [18].

4.3.2 Neutrino generation

Neutrino interactions in KM3NeT are simulated using the gSeaGen framework [16]. The simulation covers all neutrino flavours and interaction channels over a wide energy range, from 10^2 to 10^8 GeV, and includes the propagation of charged leptons to the can surface. The main interaction processes considered are quasi-elastic scattering, resonant interactions, and deep inelastic scattering, with the latter dominating at these energies. To realistically account for absorption effects, the transmission probability of neutrinos through the Earth is computed using the PREM density model, which describes the variation of the Earth's internal structure with depth. Neutrino events are initially generated with a simple power-law spectrum ($E^{-1.4}$) to ensure good statistical coverage across the full energy range, and are reweighed to match physical flux models. The weighting incorporates the chosen flux parameterisation, the interaction cross section, the Earth transmission probability, and the appropriate normalisation constants. For the atmospheric neutrino background, two components are considered: the conventional flux, originating from pion and kaon decays and modeled with the Honda et al. (2006) [19] parameterisation, which dominates up to tens of TeV; and the prompt flux, produced in the decay of charmed hadrons, modeled following Enberg et al. [20], which becomes increasingly important at higher energies due to its harder spectrum. Both components are further corrected to reflect the steepening of the primary cosmic ray spectrum at the so-called knee, as described by the H3a composition model.

4.3.3 Light generation

In the KM3NeT simulation chain, the program JSirene, which is part of the JPP software framework [21] is responsible for propagating charged particles inside the can volume and for simulating the production of Cherenkov light in seawater. It accounts for the continuous energy loss of muons along their tracks, including light from minimum ionising particles, δ-rays, and stochastic processes such as bremsstrahlung. Electrons and positrons are treated through bremsstrahlung and pair production, both of which are modeled as electromagnetic showers. Hadronic showers are approximated in the same way, since in water their light production is sufficiently similar to that of electromagnetic showers. Tau leptons are simulated as minimum ionising particles producing δ-rays along their path. Instead of tracking every single photon individually, which would be far too slow, JSirene uses precomputed probability density functions (PDFs) of photon arrival times. These PDFs depend on the energy of the primary particle, the distance between the particle trajectory and a PMT, and the angle under which photons reach the PMT.

To describe photon transmission in water, JSirene includes absorption and dispersion, and it approximates scattering by considering only single scattering, for which an analytic treatment is available. The simulated light yield is then combined with the response of the KM3NeT photomultipliers. They also include the response of the photomultiplier tubes (PMTs), such as their angular acceptance and quantum efficiency, to produce realistic distributions of detected photo-electrons.

4.4 Detector response

4.4.1 Trigger level

Following the light generating step with `JSirene`, the simulation proceeds with the software `JTriggerEfficiency`. This software is responsible for converting the idealised photon information into a realistic detector signal and describes the KM3NeT detector's response to light. `JTriggerEfficiency` first converts the photons into detected photo-electrons, taking into account the quantum efficiency and angular acceptance of each PMT. It then simulates the internal PMT response and the readout electronics. In particular, the detection times of photo-electrons are not exact but are sampled from the measured transit-time spread distributions of the KM3NeT PMTs, which introduce a natural timing uncertainty. In addition, the program includes the contribution of random optical background present in the deep sea. This background is dominated by the radioactive decay of ^{40}K in seawater, which produces photons detected as single coincidences at an average rate of about 7 kHz per PMT, as well as contributions from bioluminescence.

Two categories of simulation are usually performed: one assumes nominal detector conditions with standard PMT parameters and a fixed background rate, while the other follows a run-by-run approach, in which the measured background rates and calibration constants for each PMT during real data taking are reproduced. The software also models the charge response of the PMTs, i.e., how the observed charge relates to the number of detected photons, which may vary slightly for each sensor. The output of `JTriggerEfficiency` is a list of hits, each containing the PMT identifier, the time, and the charge, in exactly the same data format as used for the events collected from the sea. At this stage, the simulated events are indistinguishable from real raw data.

The final step in this stage of the chain is the application of the detector trigger conditions. The trigger algorithms search for characteristic hit patterns, such as coincidences across different PMTs in a short time window around the event, referred to as "snapshot" [22]. This time window is set at 3.5 μs for ARCA21 configuration. When the conditions are

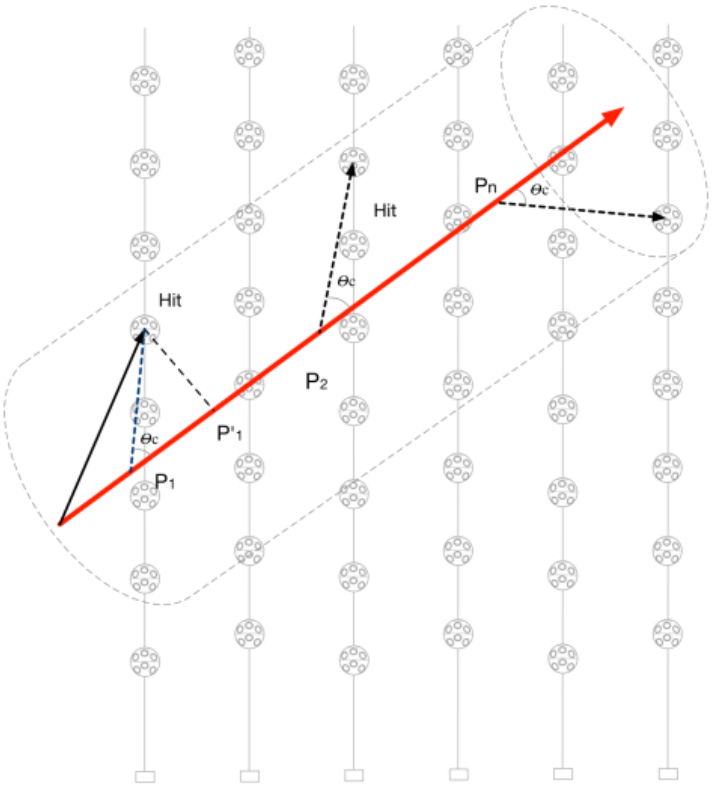

Fig. 4.8: Schematic overview of muon triggering. All hits falling inside a cylinder whose axis is the muon track are taken into account. The Cherenkov light emitted is represented by dashed lines. Taken from [25].

met, all hits falling in that predefined window are written to disk. Currently, the following algorithms are use: 3DShower, 3DMuon, MXShower. For instance in the 3DMuon trigger algorithm, the trigger condition states that at least 5 causally correlated hits fall inside a cylinder whose axis is the muon track and with a radius of 120 m (Fig. 4.8). The Cherenkov condition which describes the correlation of a pair of hits is given by:

$$(t_i - t_j)c - (z_i - z_j) \leq \sqrt{(x_i - x_j)^2 + (y_i - y_j)^2} \tan\theta_c \tag{4.4}$$

where θ_c represents the Cherenkov angle and x,y,z denote the position of the PMT. The remaining trigger algorithms are described in details here [23], [24].

4.4.2 Reconstrustion

The reconstruction step allows to infer the physical parameters of an event (mainly the energy, vertex and direction) by fitting a model parameter to data. In fact, reconstruction is applied on both the real data and the MC simulations. In this section, only the track

reconstruction is highlighted since the primary goal of this thesis is the study of track-like events produced by atmospheric muons. The shower reconstruction can be found here [26].

a) Track reconstruction

The track reconstruction is divided into 5 steps known as the reconstruction chain. The first three steps fit the position and direction of track events within the detector and the last two estimate the length and energy of the track.

JMuonPrefit

The reconstruction of a muon track involves five independent parameters: two for the direction and three for the position. Since the relation between the photon arrival times and these parameters is highly non-linear, the prefit algorithm `JMuonPrefit` simplifies the problem by scanning a grid of possible track directions covering the sky. For each assumed direction, only the muon's position and reference time are fitted, effectively reducing the problem to a linear one. The fit is based on minimizing a χ^2 function that compares the expected and measured photon arrival times, normalized by the detector's timing resolution. From this scan, the algorithm keeps the most promising solutions (around 40 in practice) and passes them to `JMuonSimplex`, which then improves the reconstruction with a more detailed likelihood fit.

JMuonSimplex

After `JMuonPrefit` has generated a collection of potential track solutions, the algorithm `JMuonSimplex` proceeds to refine them. `JMuonSimplex` implements a more precise optimisation process in contrast to the prefit stage, which relies on a simplified χ^2 minimisation and a coarse directional scan. It achieves this by assessing the *time residuals*, which are the difference between the actual particle detection times and the expected times for a specific muon path. The muon trajectory is more accurately represented by `JMuonSimplex` when the track parameters are adjusted to minimise these residuals.

JMuonGandalf

JMuonGandalf is the central algorithm of the muon track reconstruction chain. It builds upon the intermediate solutions provided by *JMuonSimplex*, then performs a more refined fit. Starting from the candidate tracks, it scans around each hypothesis and minimizes a χ^2-like function in terms of both track direction and track position. The key to this method is the use of semi-analytical arrival time distributions. These

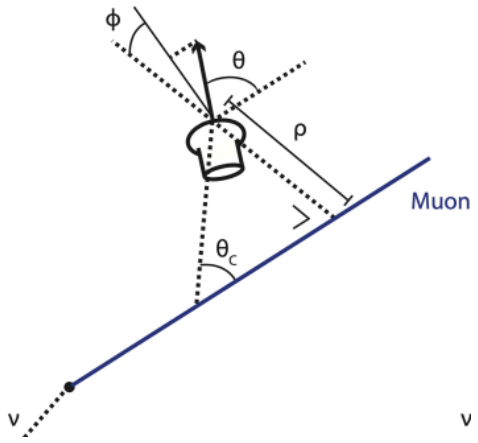

Fig. 4.9: Schematic overview of a muon track passing near a PMT. Taken from [23].

distributions describe the probability for a PMT to detect photo-electrons at specific times, depending on its position and orientation relative to the muon track. In building these distributions, many detectors and medium effects are explicitly taken into account, i.e, the quantum efficiency of the PMTs, the transit-time spread, the angular acceptance of the PMTs, and the wavelength-dependent dispersion, absorption, and scattering of light in seawater. The light sources themselves are also modeled in detail.

Besides direct Cherenkov photons, the algorithm includes single scattered photons, photons from electromagnetic and hadronic showers produced along the track, photons from δ-rays, and the general stochastic energy losses of the muon. All these contributions are combined to define probability density functions (PDFs) for the photon arrival times. In practice, a PDF represents the probability that the first detected photo-electron arrives at a given relative time compared to the expected time of an unscattered Cherenkov photon. The PDF distributions for a muon track passing a PMT (sketch presented in Fig. 4.9) with an energy of 10 GeV and at a distance of 50 m for different orientation of the PMT are shown in Fig. 4.10. With these PDFs, JMuonGandalf constructs likelihood functions under two competing hypotheses:

- H_0 hypothesis: the hit pattern arises from background noise, such as bioluminescence or radioactive decay (background hypothesis).
- H_1 hypothesis: the hit pattern is caused by a muon track (signal hypothesis),

The algorithm then minimizes the negative log-likelihood ratio between these two hypotheses. Thanks to Wilks' theorem [27], the logarithm of the likelihood ratio asymptotically follows a χ^2 distribution, which allows the definition of a statistical quality measure for the fit. The best-fit track corresponds to the minimum of this function, i.e. the solution most compatible with the presence of a signal track and

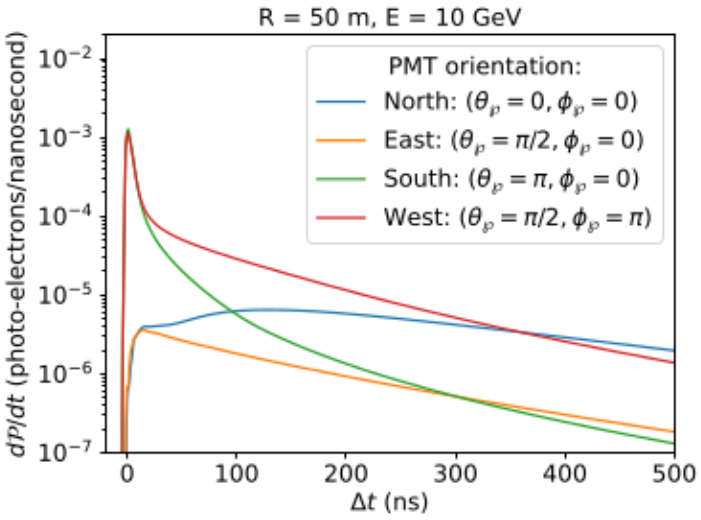

Fig. 4.10: Number of photo-electrons as function of the difference between the expected and actual arrival time of muon light using the Cherenkov hypothesis. Taken from [24].

least compatible with the background-only scenario. Finally, JMuonGandalf defines a quality parameter for the reconstruction,

$$Q = -\chi^2,$$

which quantifies the reliability of the fitted track [18].

JMuonStart

The algorithm JMuonStart is responsible for finding the starting point of the reconstructed muon track. While JMuonGandalf provides the direction and position of the track as a whole, it does not identify where along that track the muon actually originated. To do this, JMuonStart uses a back-projection technique: it projects the detected photon hits back onto the reconstructed track at the Cherenkov angle.

JMuonEnergy

This is the final step of the reconstruction chain where *JMuonEnergy* estimates the energy of the reconstructed track. To perform this estimation, JMuonEnergy minimizes a likelihood function that depends on the muon energy E. The likelihood is built from the probability of observing the measured hit pattern in the detector, using a cylindrical region around the reconstructed muon track. For each PMT inside this cylinder, the expected number of photon hits $\mu_i(E)$ is calculated. The number of hits detected by the i th PMT follows a Poisson distribution:

$$P(n; \mu_i(E)) = \frac{\mu_i(E)^n}{n!} e^{-\mu_i(E)}, \tag{4.5}$$

where $\mu_i(E)$ represents the expected number of hits as a function of energy. Based

on this, two useful probabilities are derived:

– the probability that no hits are observed:

$$P(n = 0; \mu_i(E)) = e^{-\mu_i(E)},$$

– the probability that at least one hit is observed:

$$P(n > 0; \mu_i(E)) = 1 - e^{-\mu_i(E)}.$$

The full likelihood $L(E)$ is then built as a product (or sum in log-space) over all PMTs inside the cylinder, depending on whether hits were observed or not. The definition of the likelihood in ORCA is different from the one in ARCA, reflecting their distinct detector geometries and energy ranges: In ORCA, a null M-estimator is used, giving the likelihood

$$L(E) = -\sum_{i=1}^{N} \ln\left[\left(1 - 2e^{-\mu_i(E)}\right) I_{n>0} + e^{-\mu_i(E)}\right],$$

where $I_{n>0}$ is 1 if at least one hit was observed on the PMT and 0 otherwise. In ARCA, when the estimator is based on a Lorentzian weighting function, the performances are improved

$$\rho(x) = \frac{1}{1 + \frac{1}{2}x^2},$$

leading to

$$L(E) = \sum_{i=1}^{N} \frac{1}{1 + \ln^2[(1 - 2e^{-\mu_i(E)})\, I_{n>0} + e^{-\mu_i(E)}]}.$$

minimizing the chosen likelihood with respect to energy, `JMuonEnergy` finds the value of E that best explains the observed pattern of PMT hits [18].

4.4.3 Reconstruction performance

Fig. 4.11 summarizes the performance of the ARCA detector for reconstructing charged-current (CC) neutrino events. For ν_μ CC track events, the angular resolution improves with energy, reaching about 0.1° at 100 TeV. This makes ν_μ tracks particularly valuable for neutrino astronomy, as they enable precise source pointing. In contrast, ν_e CC shower events exhibit a poorer angular resolution of about 3–6°, with only a modest improvement as energy increases. The energy resolution shows the opposite behavior. For track events, it is relatively poor ($\sim$ 50–100%), since a large fraction of the neutrino energy is carried away by the muon, which only deposits part of its energy in the detector. For shower

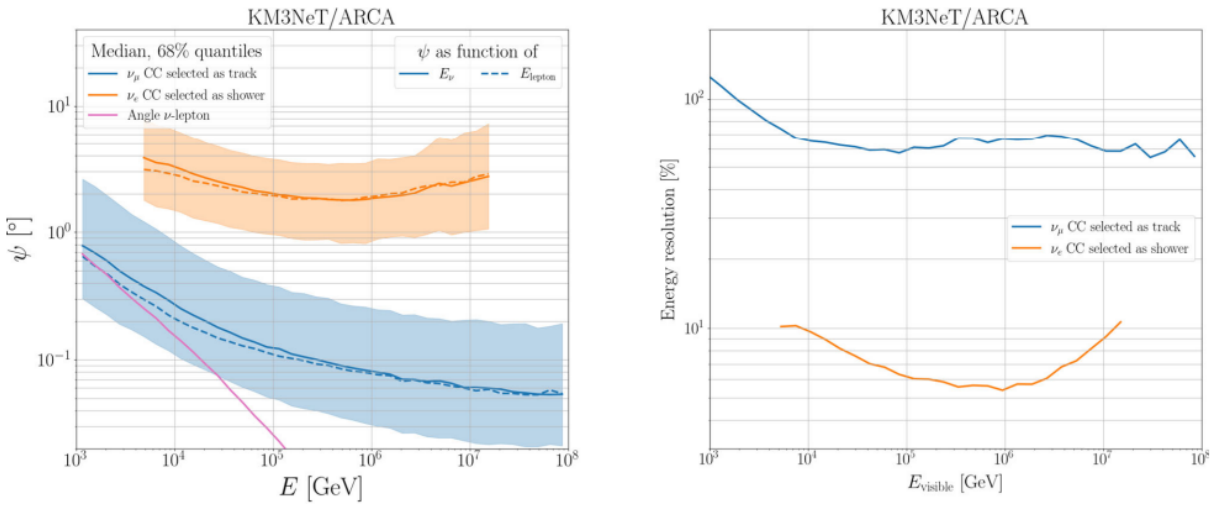

Fig. 4.11: The angular deviation of ARCA (left) and angular resolution (right) for ν_μ CC tracks and ν_e CC showers. Taken from [28].

events, the resolution is much better ($\sim$ 10–20%), as nearly all the neutrino energy is deposited in the hadronic and electromagnetic cascades, allowing a more reliable reconstruction. The resolution improves at intermediate energies (a few TeV-PeV) and worsens again at the highest energies due to shower fluctuations and light propagation effects.

For the muon reconstruction performance, well-reconstructed events are defined as those with $\cos\theta > 0.6$. As shown in the Figure 4.12 for the ARCA6 detector, the reconstructed muon energy does not directly match the true energy at the can surface. This is because muons lose part of their energy while propagating through seawater between the can surface and the point where the first Cherenkov light is detected. Therefore, the muon energy at the can must be corrected.Still a substantial disagreement is observed across the entire energy range in ARCA6.

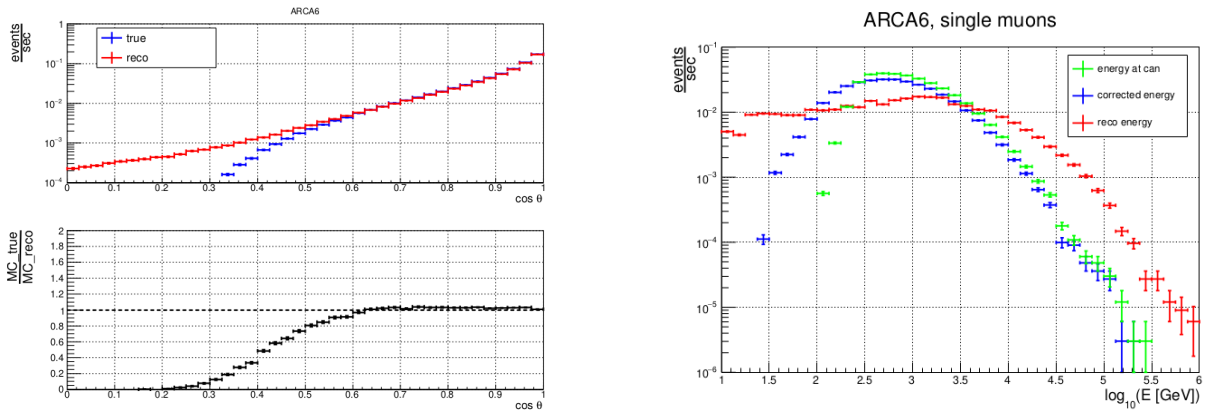

Fig. 4.12: Performance of the zenith angle reconstruction(left) and single muon energy reconstruction (right) for ARCA6 detector configuration. Taken from [18].

References

[1] D. Heck, J. Knapp, J. N. Capdevielle, G. Schatz, and T. Thouw, *CORSIKA: A Monte Carlo code to simulate extensive air showers, Report FZKA 6019*. Forschungszentrum Karlsruhe, 1998.

[2] T. Pierog *et al.*, *Phys. Rev. C*, vol. 92, p. 034 906, 2015. DOI: 10.1103/PhysRevC.92.034906.

[3] F. Riehn *et al.*, *Phys. Rev. D*, vol. 102, p. 063 002, 2020. DOI: 10.1103/PhysRevD.102.063002.

[4] S. Ostapchenko, *Phys. Rev. D*, vol. 89, p. 074 009, 2014. DOI: 10.1103/PhysRevD.89.074009.

[5] A. Fedynitch *et al.*, *Proc. 34th Int. Cosmic Ray Symp., the Hague, the Netherlands, PoS (ICRC2015) 1129*, 2015.

[6] M. Bleicher *et al.*, *J. Phys. G*, vol. 25, p. 1859, 1999. DOI: 10.1088/0954-3899/25/9/308.

[7] M. G. Aartsen *et al.*, *Astropart. Phys.*, vol. 78, p. 1, 2016. DOI: 10.3847/0004-637X/833/1/3.

[8] R. U. Abbasi and et al., *Physical Review D*, vol. 98, no. 2, p. 022 002, 2018. DOI: 10.1103/PhysRevD.98.022002.

[9] T. Huege *et al.*, *Proc. 38th Int. Cosmic Ray. Conf.*, vol. Nagoya, Japan, p. 310, 2023.

[10] J.-H. Koehne *et al.*, *Comp. Phys. Commun.*, vol. 184, no. 9, pp. 2070–2090, 2013. DOI: 10.1016/j.cpc.2013.04.001.

[11] T. K. Gaisser and A. M. Hillas, *Proc. 15th Int. Cosmic Ray Conf.*, vol. 8, p. 353, 1977.

[12] L. D. Landau and I. Y. Pomeranchuk, *Dokl. Akad. Nauk SSSR*, vol. 92, p. 535, 1953.

[13] A. B. Migdal, *Phys. Rev.*, vol. 103, p. 1811, 1956. DOI: 10.1103/PhysRev.103.1811.

[14] G. Molière, *Z. Naturforsch. A*, vol. 2, p. 133, 1947.

[15] V. L. Highland, *Nucl. Instrum. Meth.*, vol. 129, p. 497, 1975. DOI: 10.1016/0029-554X(75)90743-0.

[16] S. Aiello and et al., *Comput. Phys. Commun.*, vol. 256, p. 107 477, 2020. DOI: 10.1016/j.cpc.2020.107477.

[17] M. Bazzotti *et al.*, *Comput. Phys. Commun.*, vol. 179, p. 915, 2008. DOI: 10.1016/j.cpc.2008.07.014.

[18] A. Romanov, "Cosmic ray studies with the km3net neutrino telescope," PhD Thesis, 2023.

[19] M. Honda *et al.*, *Phys. Rev. D*, vol. 75, p. 043 006, 2006. DOI: 10.1103/PhysRevD.75.043006.

[20] R. Enberg *et al.*, *Phys. Rev. D*, vol. 78, p. 043 005, 2008. DOI: 10.1103/PhysRevD.78.043005.

[21] *The jpp framework*, https://sftp.km3net.de/documentation/jpp/v17.3.2/.

[22] O. Adriani *et al.*, *arXiv preprint arXiv:2506.05881*, 2025. arXiv: 2506.05881 [astro-ph.IM].

[23] T. J. van Eeden, "Neutrino astronomy with km3net/arca," Thesis, fully internal, Ph.D. dissertation, Universiteit van Amsterdam, 2024.

[24] B. Ó Fearraigh, "Following the light: Novel event reconstruction techniques for neutrino oscillation analyses in km3net/orca," PhD thesis, Ph.D. dissertation, Universiteit van Amsterdam, 2024.

[25] C. De Sio, "Event triggering and deep learning for particle identification in km3net," PhD thesis, Università degli Studi di Napoli Federico II, Ph.D. dissertation, Dottorato di Ricerca in Matematica, Fisica e Applicazioni, XXX ciclo, 2017.

[26] K. Melis *et al.*, *Proc. 35th Int. Cosmic Ray. Conf.*, vol. PoS(ICRC2017)1059, Bexco, Busan, Korea, p. 76,

[27] S. Wilks, *Ann. Math. Statist.*, vol. 9, p. 60, 1938. DOI: 10.1214/aoms/1177732360.

[28] S. Aiello *et al.*, *Eur. Phys. J. C*, 2024. DOI: 10.1140/epjc/s10052-024-13137-2.

Chapter 5

High-energy atmospheric muons

In this chapter, the high-energy atmospheric muons are investigated starting with their flux and charge ratio at sea level, followed by their propagation through sea water down to the depth of the ARCA detector. These studies provide an essential reference for understanding the background conditions at the detector site and form the basis for the analysis of CR induced signal in the following chapter.

5.1 Muons at sea level

Atmospheric muons, produced by high-energy cosmic rays represent the dominant particles that trigger deep underwater neutrino detector such as IceCube[1], Baikal-GVD[2], and KM3NeT. These aforementioned detectors heavily rely on the ability to detect these muons in order to infer the presence of neutrino interactions occurring beneath the surface of the water or ice. Due to the critical role that muons play in these detection systems, it is of utmost importance to acquire a comprehensive understanding of their characteristics at sea level. A thorough examination of the flux and charge ratio of muons in the sea-level environment provides us with invaluable insights into the behavior and properties of these particles, enabling us to accurately interpret the data collected by these detectors. In addition to their relevance for neutrino detection, muons at sea level serves as tracers for the primary cosmic ray flux, thus providing valuable information for studies of cosmic-ray anisotropy at the detector level. In the subsequent section, we will delve into the analysis of the flux and charge ratio of atmospheric muons with energies exceeding 100 GeV at sea level.

5.1.1 Simulation setup

We conducted a series of Monte Carlo simulations of extensive air showers initiated by cosmic rays of high energy. For this investigation, we primarily employed CORSIKA version 7.7500 in combination with the post-LHC hadronic interaction models, sibyll, QGSJET, EPOS. Fine-tuned at energies that are characteristic of colliders, these models have been carefully adjusted and calibrated to ensure that the results they produce are in line with the outcomes observed in a wide range of experiments that cover a broad energy spectrum. This process of validation, which confirms the accuracy and reliability of these models, establishes them as the leading and most-prominent choice for simulating and replicating the complex phenomenon of cosmic-ray cascades occurring in the Earth's atmosphere.

The characteristics of atmospheric muons are significantly influenced by the primary cosmic-ray energy spectrum and mass composition. In order to examine this correlation, two realistic models were employed that effectively capture essential elements of the primary cosmic-ray flux, including distinct features such as the knee and the ankle. The first model, known as the Gaisser-Stanev-Tilav (GST)[3] phenomenological model, highlights the presence of three populations of cosmic rays. The first two populations are attributed to the acceleration by sources within the Milky Way, while the third population is believed to originate from beyond our galaxy. Each of the three components comprises up to five groups of nuclei (p, He, C, O, Fe), with adjustable spectral indices and exponential cutoffs at characteristic rigidities. The overall primary energy spectrum of all particles can be expressed as:

$$\phi_i(E) = \sum_{j=1}^{3} a_{i,j} E^{-\gamma_{i,j}} \exp\left\{\left(-\frac{E}{Z_i R_{c,j}}\right)\right\} \tag{5.1}$$

where E represents the primary energy, $\gamma_{i,j}$ stands for the spectral index, $a_{i,j}$ represents a normalization constant, Z_i denotes the atomic number, and $R_{c,j}$ signifies the rigidity cutoff. The subscript i spans across the five nuclei groups, and the overall particle spectrum is derived from the summation of these five components (Fig. 5.1).

The Global Spline Fit (GSF) is the second model employed in this particular study to effectively characterize the primary cosmic-ray spectrum [4]. This model, unlike the previous one, takes a numerical and data-driven approach to accurately parametrize the most up-to-date measurements of the cosmic-ray flux and its mass composition. To be more precise, the GSF model utilizes splines to smoothly fit the present cosmic-ray data within the energy range of 10 GeV to 10^{11} GeV incorporating both direct and indirect observations and ensuring a comprehensive understanding of the cosmic-ray phenomenon. Similar

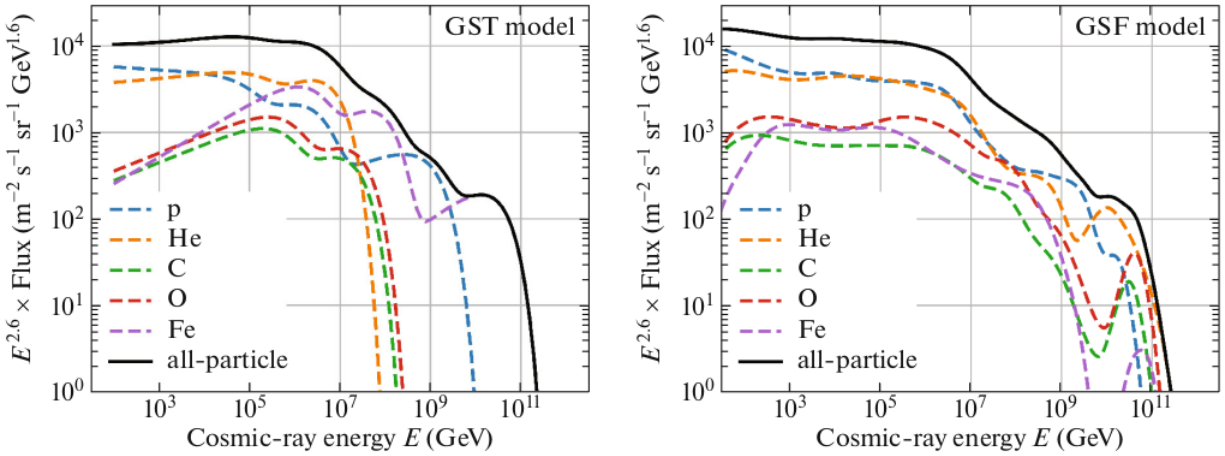

Fig. 5.1: The GST model [3] (left) and the GSF model (right) [2] of the primary cosmic-ray flux and mass composition. The flux is multiplied by $E^{2.6}$ to highlight the unique features of the steep spectrum.

to the previous model, we considered the five principal mass groups of the GSF model, which are proton (p), helium (He), carbon (C), oxygen (O), and iron (Fe) (Fig. 5.1).

In order to ensure a sufficient pool of statistics across all energy levels, the primary cosmic-ray particles were injected based on an energy spectrum that follows an E^{-1} shape, up until the highest energy level was reached. Subsequently, we adjusted the resulting distributions by reweighing them and ensuring appropriate normalization to align with the model used for the primary cosmic-ray flux (Figure 5.2). The reweighing formula is given by:

$$w(E_{\text{prim}}) = \frac{\ln\left(\frac{E_{\text{max}}}{E_{\text{min}}}\right)}{\int_{E_{\text{min}}}^{E_{\text{max}}} \phi(E)\, dE} E_{\text{prim}}\, \phi(E_{\text{prim}}). \tag{5.2}$$

where $\phi(E)$ is the differential primary cosmic ray flux, E_{prim} is the energy of the primary cosmic ray, E_{min} and E_{max} are the minimum and maximum energies of the simulation.

Each individual run consisted of 10^5 primary cosmic-ray particles with energies ranging from 10^2 to 10^7 GeV. For the purpose of the simulation setup, we carefully evaluated a hypothetical detector positioned at sea level, with a radius equivalent to the maximum span of the muon lateral distribution (Fig. 5.3). The simulated shower cores were redistributed randomly, covering an effective area that had a radius twice as large as that of the detector. As a result of our calculations, it was observed that approximately 25% of the simulated muons reach the hypothetical detector.

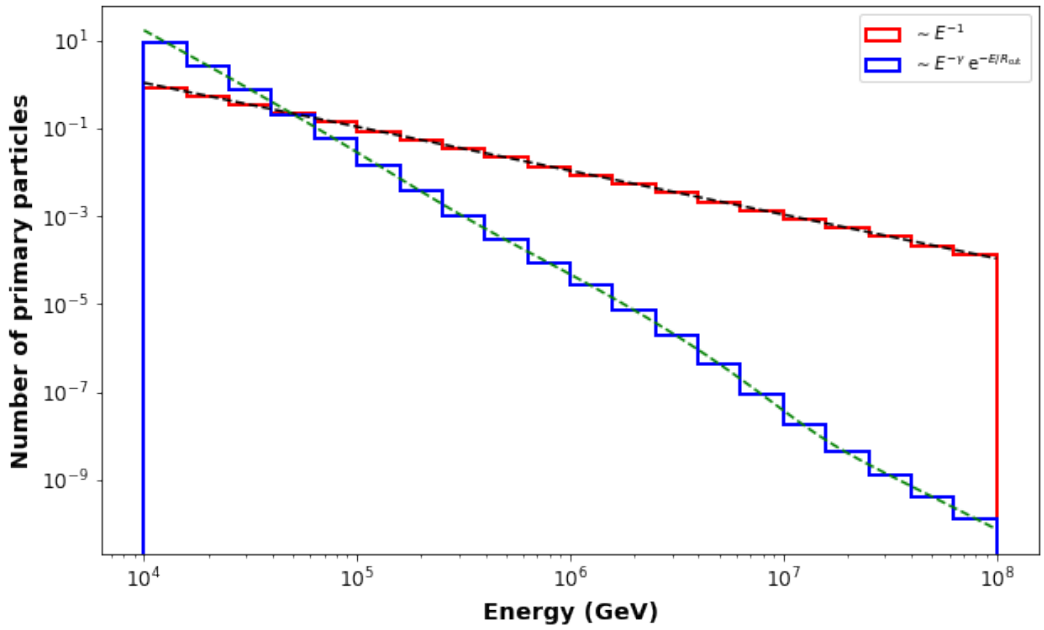

Fig. 5.2: Number of primary particles as function of the energy before(red) and after (blue) applying the reweighing defined in equation 5.1.

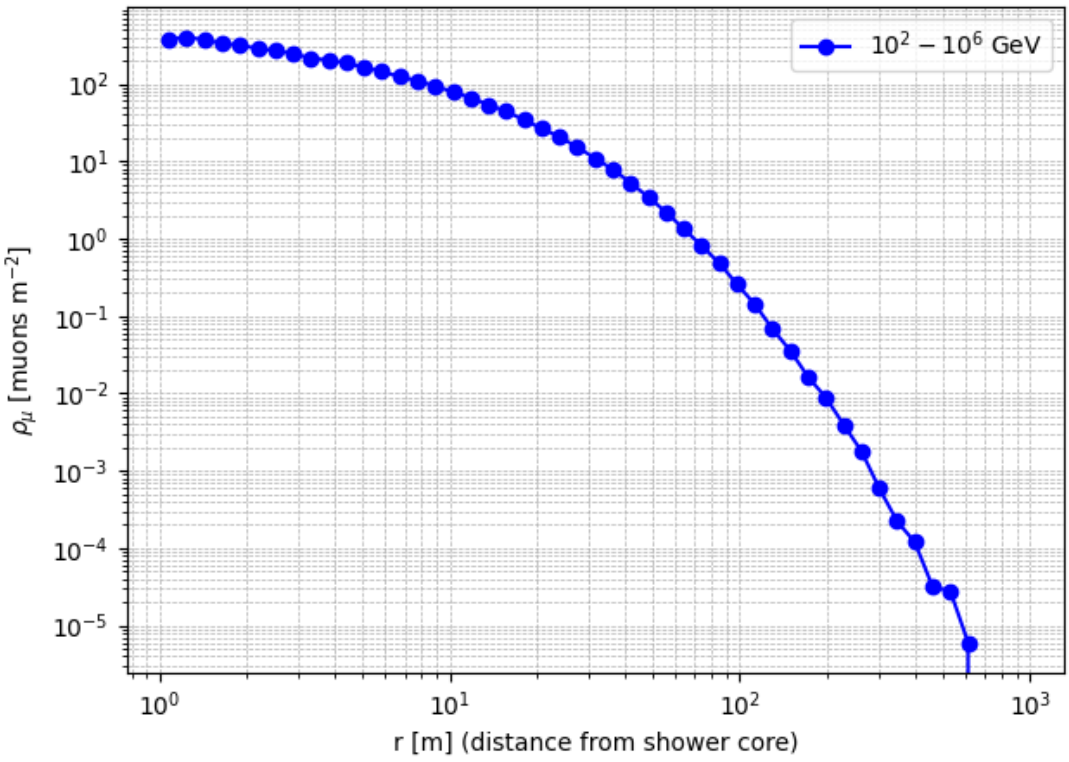

Fig. 5.3: Lateral distribution of the muonic component at sea level.

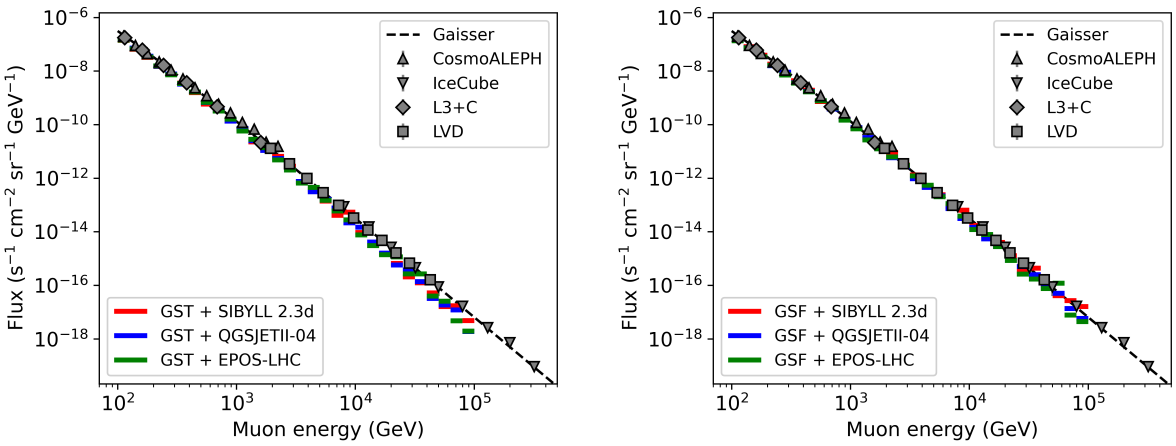

Fig. 5.4: Energy spectrum of vertical atmospheric muons at sea level for the GST (left) and GSF(right) models in comparison with CosmoALEPH [5], L3+C [6], Icecube data [8]. Taken from [9].

5.1.2 Results

Fig. 5.4 presents a visualization of the energy spectrum of vertical atmospheric muons with an energy threshold of 100 GeV at sea level. The simulation were performed using the 3 post-LHC hadronic interaction models. The results are in agreement with experimental data obtained from various experiments such as CosmoALEPH[5], L3+C [6], LVD [7], and IceCube[8]. Additionally, these simulations also exhibit good agreement with the analytical parametric model proposed by Gaisser. It is interesting to note that the three hadronic interaction models yield almost identical intensities of atmospheric muons at sea level. This observation holds true for both cosmic-ray flux models, GST and GSF.

One key parameter that provides valuable insights into the hadronic interaction and can aid in determining the mass composition of primary cosmic rays is the muon charge ratio. This ratio, defined as the ratio of the fluxes of positive to negative muons (N_μ^+/N_μ^-), plays a crucial role. It reflects important aspects of the hadronic interaction, particularly the excess of positively charged pions (π^+) over negatively charged pions (π^-) and positively charged kaons (K^+) over negatively charged kaons (K^-) in the forward fragmentation region of interactions induced by protons. This distinction is due to the positively charged nature of primary cosmic rays. A discernible increase in the contribution of kaon decays to the charge ratio of muons can be observed in the TeV energy range [10]. At energies above 10 GeV, where solar and geomagnetic effects have negligible impact, the experimental value of N_μ^+/N_μ^- remains relatively constant, hovering around 1.3 [11].

Fig. 5.5 illustrates the calculated charge ratio of vertical atmospheric muons that exceed 100 GeV at sea level. This ratio is plotted against muon energy and takes into account the

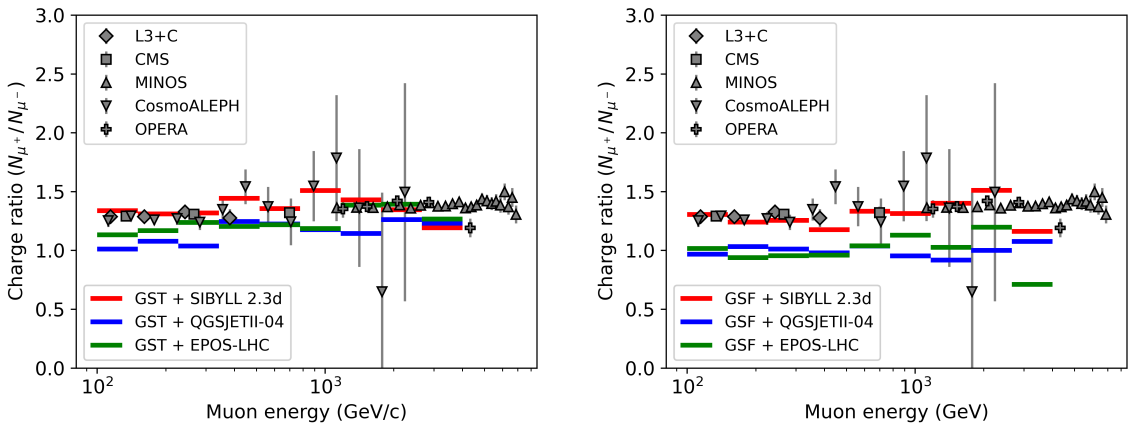

Fig. 5.5: Charge ratio computed for vertical atmospheric muons at sea level using the GST (left) and GSF (right) models in comparison with CosmoALEPH [5],OPERA [12], L3+C [6], CMS [13] and MINOS [14] data. Taken from [9].

three hadronic interaction models as well as the two cosmic-ray flux models. The results of this analysis align well with experimental data obtained from experiments such as CMS, L3+C, CosmoALEPH , MINOS, and OPERA. However, it is worth noting that the QGSJETII-04 and EPOS-LHC models tend to underestimate the charge ratio of vertical muons when compared to the SIBYLL 2.3d model. The latter exhibits greater consistency with the available data for both the GST and GSF models. The muon energy range is not fully representative in the latest energy bin due to limitations in statistics at the highest energies.

Fig. 5.6 presents a comparison between the muon flux and charge ratio of vertical atmospheric muons at sea level obtained from the GST model and those from recent studies that are comparable. One interesting paper is the work by Fedynitch et al. [15], where the authors used in their calculations the SIBYLL-2.3c hadronic interaction model (a previous version of SIBYLL) and the H3a cosmic-ray flux model [26] to compute the flux of atmospheric leptons. This computation was conducted using MCEq [16], a numerical code specifically designed to solve the cascade equations that describe the evolution of cosmic rays as they traverse through the atmosphere. Another study conducted by Kochanov et al. [4], focused on calculating the atmospheric muon flux in the energy range of 10 GeV-10 PeV. In this study, the authors employed the Kimel & Mokhov hadronic interaction model [17] in conjunction with the parametrisation of the cosmic-ray spectrum proposed by Zatsepin & Sokolskaya [18]. Additionally, another intriguing study by Fedynitch & Huber [19] was taken into consideration, which addressed the calculation of the flux and charge ratio of atmospheric muons using the Data Driven Model (DDM) in association with the GSF model. It is worth noting that the GSF model is the model employed in the present study. By analyzing Figure 5.6, it can be observed that the results obtained from this study exhibit consistency with the outcomes of all the aforementioned studies.

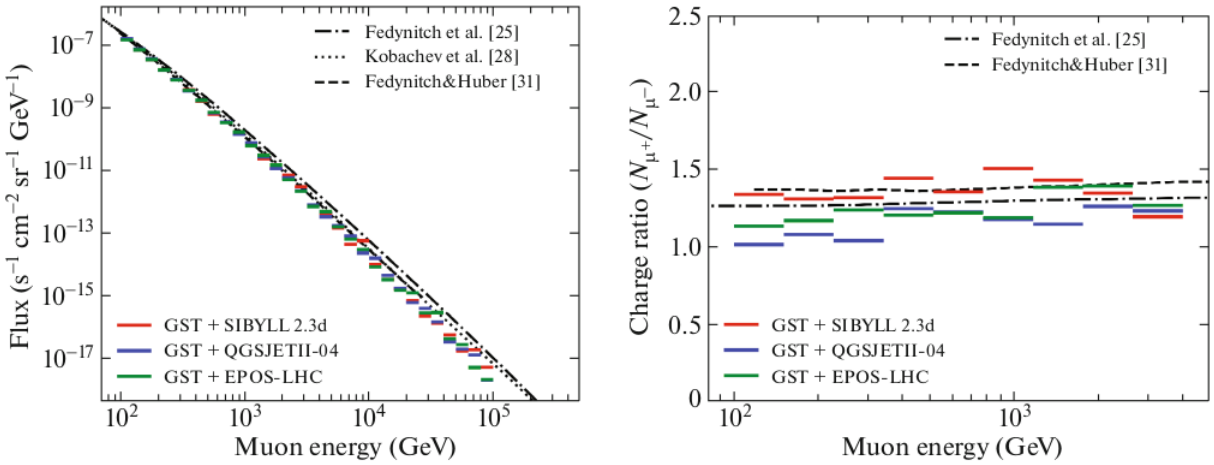

Fig. 5.6: Comparison the flux (left) and the charge ratio (right) of vertical atmospheric muons at sea level with recent comparable studies in the case of the GST model. Taken from [9].

Furthermore, the flux of atmospheric muons at sea level is estimated across a wide range of zenith angles based on the GSF and GST cosmic ray spectrums in combination with the post-LHC hadronic interaction models. In the case of inclined showers, the radius of the hypothetical detector is taken as $R_{\text{det}} = 112.8$ km, which corresponds to the average altitude of the first cosmic-ray interaction in the atmosphere as illustrated in Fig. 5.7. The normalization formula is given by:

$$\phi_\mu(E_\mu) = \frac{1}{N_{\text{sim}}} \cdot \frac{dN_\mu}{dE_\mu} \cdot \left(\int_{E_{\text{min}}}^{E_{\text{max}}} \phi_{\text{prim}}(E)\, dE \right) \cdot \frac{R_{\text{eff}}^2}{R_{\text{det}}^2} \cdot \frac{\Omega_0}{\Omega_\mu}, \tag{5.3}$$

where Ω_0 and Ω_μ represent the solid angles of the primary particle and the produced muon respectively. N_{sim} is the number of simulated showers, N_μ denotes the number of simulated muons and E_μ represent their energies.

Fig. 5.8 represents the flux for muons with zenith angles up to 60°, with IceCube data indicated by black triangles and the best-fit spectrum shown as a dashed black line. The comparison shows a strong dependence on the chosen hadronic interaction model. SIBYLL 2.3d has the highest agreement with IceCube data, with consistency within a factor of two in the energy range of 10^4 to 10^7 GeV. In contrast, QGSJET II-04 and, in particular, EPOS-LHC overestimate the muon flux, particularly at higher energies. These discrepancies are further highlighted in the bottom panel of Fig. 5.8, which shows the ratio of each model to the IceCube best-fit. This investigation demonstrates the sensitivity of atmospheric muon flux predictions to the treatment of hadronic interactions in air shower simulations. It also emphasizes the importance of accurate modelling for interpreting muon flux measurements. Fig. 5.9 is the outcome when taking into account only zenith angles from 60 to 80°.

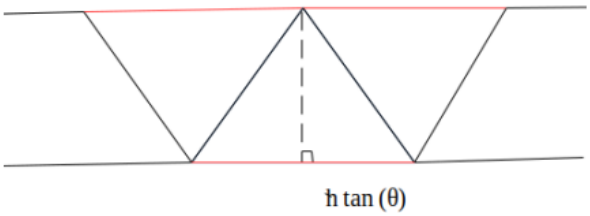

Fig. 5.7: Schematic illustration of the effective radius detector for inclined showers.

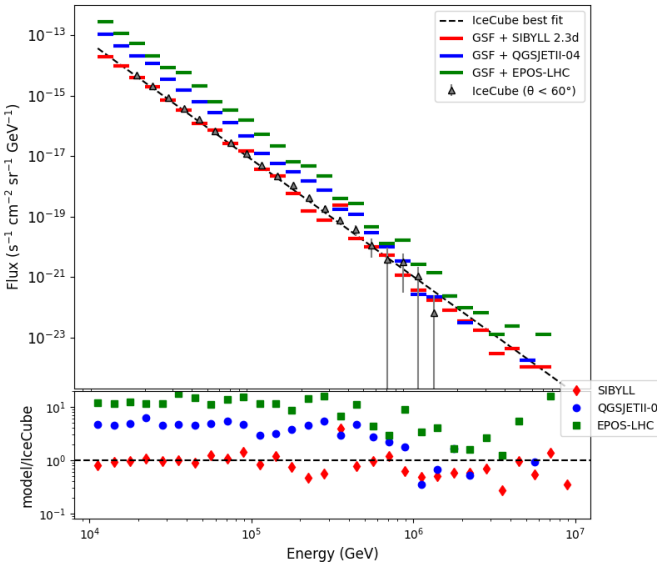

Fig. 5.8: Flux of near vertical atmospheric muons ($\theta < 60°$) at sea level compared to Icecube fit and Icecube data using the post-LHC hadronic interaction model in the case of the GSF model of primary cosmic rays.

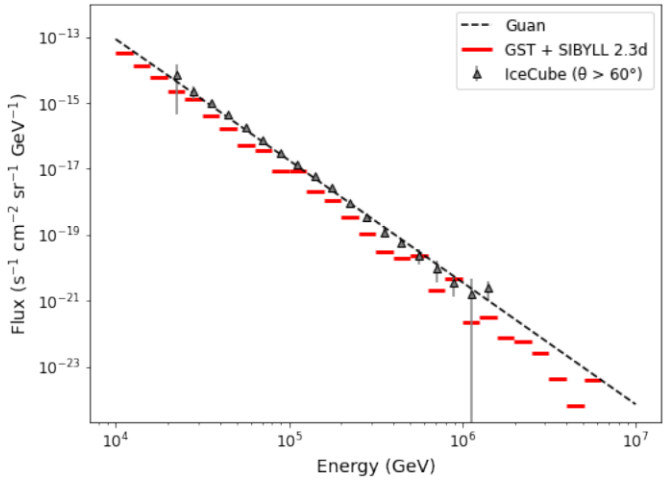

Fig. 5.9: Flux of inclined atmospheric muons ($60° < \theta \leq 80°$) at sea level compared to Guan fit [20] and Icecube data using the SIBYLL 2.3d hadronic interaction model in the case of the GST model of primary cosmic rays.

5.2 Muons underwater

To study the propagation of muons from sea level down to the detector length, the PROPOSAL library is used. The propagation was simulated through sea water for a slant depth of 3500 m. To this purpose, 10^4 muons were injected randomly at the sea surface.

The PROPOSAL framework assumes that the origin (0,0,0) is at the center of the Earth and the particle position is defined in a Cartesian 3D-system. In order to place muons correctly at the boundary of the medium, the injection points were shifted onto a surface of a sphere with a radius equals to the Earth radius R. For a given zenith angle and azimuth angle, the injection point was set to:

$$\vec{x}_{start} = (R\sin(\theta)\cos(\phi), R\sin(\theta)\sin(\phi), R\cos(\theta)) \tag{5.4}$$

with the corresponding unit vector:

$$\vec{d} = (-\sin(\theta)\cos(\phi), -\sin(\theta)\sin(\phi), -\cos(\theta)) \tag{5.5}$$

The starting position along the direction of travel was slightly displaced to ensure that the particle is not considered outside of the medium.

$$\vec{x_{start}} = \vec{x_{start}} + \epsilon\vec{d} \tag{5.6}$$

where $\epsilon = 1$ cm. In this case, the effect on the total path length is negligible.

For vertical muons, the slant depth is simply the detector depth D, but for inclined muons, the slant depth is given by:

$$L(\theta) = \frac{D}{\cos\theta} \qquad (\theta \lesssim 60^\circ) \tag{5.7}$$

For zenith angles greater than 60°, the Earth's curvature must be taken into account, the slant depth is then given by:

$$L(\theta) = \sqrt{(R+D)^2 - (R\sin\theta)^2} \; - \; R\cos\theta, \qquad (\theta > 60^\circ) \tag{5.8}$$

The survival probability of a muon with an energy E_0 and a zenith angle θ after traversing a depth D is given by:

$$P_{\text{surv}}(E_0, \theta) = \frac{N_{\text{survivors}}(E_0, \theta)}{N_{\text{injected}}(E_0, \theta)} \tag{5.9}$$

Where $N_{\text{survivors}}$ is the number of muons that arrive at ARCA depth and N_{injected} is the total number of injected muons in each (E_0, θ) bin. In these simulations, $N_{\text{injected}} = 10^4$.

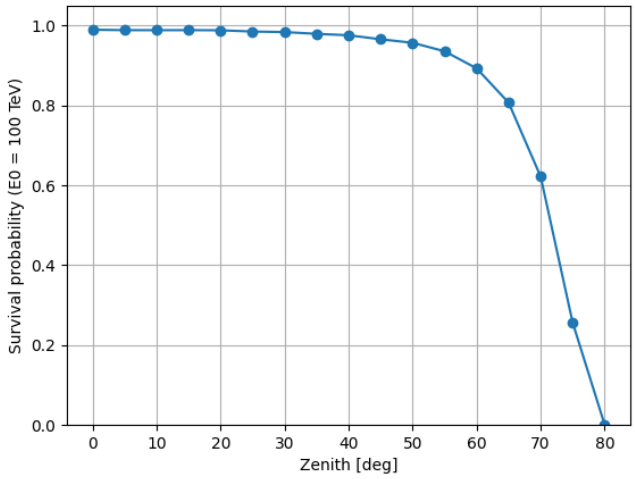

Fig. 5.10: Survival probability of 100 TeV muons as function of zenith angle at ARCA depth of 3500 m.

Fig. 5.10 shows the survival probability of muons with an initial energy of 100 TeV after propagating them through seawater down to the depth of ARCA detector. The probability remains close to 1 for nearly vertical trajectories but decreases with increasing zenith angles. At larger zenith angles ($\theta > 60°$) the survival probability reduces since the path length is longer dropping to almost 0 at zenith = 80°. As it is shown in Fig. 5.11, muons following such highly inclined trajectories can only reach the detector if their energies at sea level exceeds 100 TeV. Fig. 5.12 shows the dependence of the energy loss on the zenith angle. Near vertical muons retain a significant portion of their initial energy with mean final energies around 20–26 TeV. At large zenith angles ($\theta > 60°$), the mean final energy decreases sharply indicating the rapid increase in the energy loss as muons traverse longer paths through the medium.

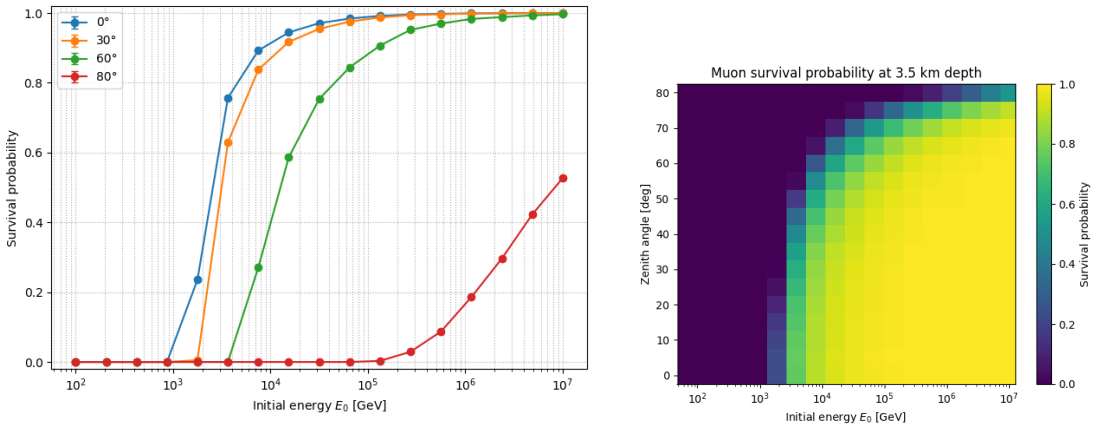

Fig. 5.11: Survival probability of muons as function of the initial energy for different zenith angles after propagation through 3.5 km of seawater.

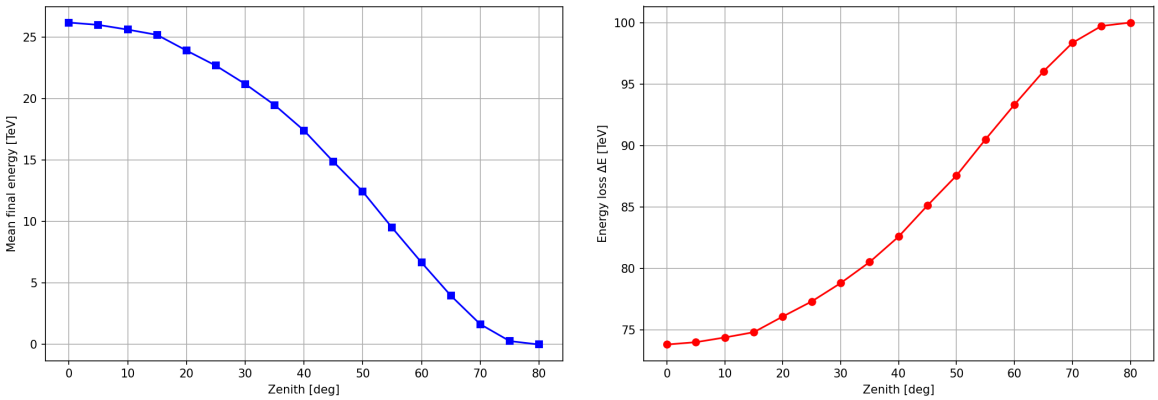

Fig. 5.12: Mean final energy (left) and muon energy loss (right) as function of the zenith angle for 100 TeV energies at sea level.

References

[1] S. Cecchini and M. Spurio, *Geosci. Instrum. Method. Data Syst.*, vol. 1, p. 185, 2012. DOI: 10.5194/gi-1-185-2012.

[2] H. P. Dembinski *et al.*, *Proc. 35th Int. Cosmic Ray Symp., Bexco, Busan, Korea, PoS (ICRC2017) 533*, 2017.

[3] T. K. Gaisser, T. Stanev, and S. Tilav, *Front. Phys.*, vol. 8, p. 748, 2013. DOI: 10.1007/s11467-013-0319-7.

[4] A. A. Kochanov *et al.*, *J. Phys.: Conf. Ser.*, vol. 1181, p. 012 054, 2019. DOI: 10.1088/1742-6596/1181/1/012054.

[5] M. Schmelling *et al.*, *Astropart. Phys.*, vol. 49, p. 1, 2013. DOI: 10.1016/j.astropartphys.2013.07.008.

[6] P. Achard *et al.*, *Phys. Lett. B*, vol. 598, p. 15, 2004. DOI: 10.1016/j.physletb.2004.08.003.

[7] M. o. Aglietta, *Phys. Rev. D*, vol. 58, p. 092 005, 1998. DOI: 10.1103/PhysRevD.58.092005.

[8] M. G. Aartsen *et al.*, *Astrophys. J.*, vol. 826, p. 220, 2016. DOI: 10.3847/0004-637X/826/2/220.

[9] A. B. Bouasla and R. Attallah, *Astron. Lett.*, vol. 49, p. 762, 2023. DOI: 10.1134/S1063773723340017.

[10] T. K. Gaisser, *Astropart. Phys.*, vol. 35, p. 801, 2012. DOI: 10.1016/j.astropartphys.2012.02.010.

[11] A. B. Bouasla and R. Attallah, *Proc. 27th European Cosmic Ray Symp., Nijmegen, the Netherlands, PoS (ECRS) 071*, 2022.

[12] N. Agafonova *et al.*, *Eur. Phys. J. C*, vol. 67, p. 25, 2010. DOI: 10.1140/epjc/s10052-010-1284-8.

[13] V. Khachatryan *et al.*, *Phys. Lett. B*, vol. 692, p. 83, 2010. DOI: 10.1016/j.physletb.2010.07.033.

[14] P. Adamson *et al.*, *Phys. Rev. D*, vol. 76, p. 052 003, 2007. DOI: 10.1103/PhysRevD.76.052003.

[15] A. Fedynitch *et al.*, *Phys. Rev. D*, vol. 100, p. 103 018, 2019.

[16] A. Fedynitch *et al.*, *Proc. 34th Int. Cosmic Ray Symp., the Hague, the Netherlands, PoS (ICRC2015) 1129*, 2015.

[17] A. N. Kalinovskii, N. V. Mokhov, and Y. P. Nikitin, *Passage of High Energy Particles Through Matter*. AIP, 1989.

[18] V. I. Zatsepin and N. V. Sokolskaya, *Astron. Astrophys.*, vol. 458, p. 1, 2006. DOI: 10.1051/0004-6361:20065108.

[19] A. Fedynitch and M. Huber, *Proc. 37th Int. Cosmic Ray Symp., Berlin, Germany, PoS (ICRC2021) 1227*, 2021.

[20] M. Guan *et al.*, *arXiv preprint*, 2015. DOI: 10.48550/arXiv.1509.06176.

Chapter 6

Cosmic-ray anisotropy observed with the ARCA neutrino telescope

In this chapter, the analysis of cosmic-ray anisotropy using the high-energy atmospheric muons detected with the ARCA detector is presented. The focus here is on extracting the large-scale anisotropy pattern. This study demonstrates the potential of the detector to probe the arrival directions of high energy CRs.

6.1 Introduction

Although the ARCA neutrino telescope is still under construction, its modular architecture has been specifically designed to enable continuous data acquisition during the staged deployment of its detection units. This important feature makes it possible to begin scientific investigations well before the completion of the full detector array. In this chapter, the focus is placed on the search for large-scale anisotropy in the arrival directions of primary cosmic rays, using data collected with ARCA during its initial operational phases, when only 21 DU's were deployed.

Since ARCA is situated at a depth of approximately 3500 m in the Mediterranean Sea, only atmospheric muons with energies exceeding roughly 1 TeV at sea level are able to penetrate to the detector. These muons are produced in extensive air showers initiated by primary cosmic rays when interacting with the atmosphere providing indirect access to the properties of the parent cosmic rays, typically in the TeV to PeV energy range. Thanks to ARCA's excellent angular resolution, which is capable of reconstructing the direction of muons with sub-degree precision, it becomes feasible to probe the angular distribution of the cosmic ray flux with high accuracy.

A genuine anisotropy in the arrival directions of cosmic rays should manifest as a variation in their intensity as a function of sidereal time, corresponding to a modulation in celestial coordinates. However, detecting such a signal is particularly challenging due to the presence of various time-dependent systematic effects. For instance, non-uniform exposure of the detector over time, geometric asymmetries, changes in detector livetime, and variations in atmospheric conditions (such as temperature-induced effects on air shower development) can all mimic or obscure real anisotropic patterns. The main challenge in this analysis is to identify and suppress these spurious effects to isolate the true astrophysical signal, thus, a careful treatment of the time and directional dependencies is required.

In our quest to identify large-scale cosmic-ray anisotropy with ARCA21, the East-West method is used to mitigate the spurious effects related to atmosphere and detector factors. while this method was originally developed to work without any corrections, the geometry of ARCA21 introduces a noticeable asymmetry. This asymmetry generates a spurious anisotropy that must be corrected beforehand. If this correction is not made, we cannot obtain a reasonable modulation of the true cosmic-ray intensity using the East-West method.

The first harmonic analysis was performed in three time frames, solar, sidereal and anti-sidereal. Each time frame helps us to identify different sources or factors that can affect the distribution of cosmic rays. The sidereal time frame is sensitive to anisotropies of astrophysical origin,i.e Galactic (or extragalactic) anisotropy. On the other hand, changes in solar time are in principle attributed to local factors, like the solar wind, diurnal atmospheric effects and the geomagnetic field. Any significant variation detected in anti-sidereal time is more likely due to systematic errors rather than a true cosmic-ray anisotropy. The statistical significance in this analysis can be evaluated using the Rayleigh probability, which can be considered as a p-value in a two-tailed test where the critical Z-score (number of σ) can be calculated using the inverse CDF (cumulative distribution function) of the standard normal distribution (Φ):

$$Z = \Phi^{-1}(1 - p/2) \tag{6.1}$$

Three energy ranges were considered in this analysis based on the energy threshold of the track, namely 10^2, 10^3, and 10^4 GeV. The maximum track energy was set at 10^6 GeV from the onset during data selection (first-level cuts).

6.2 Dataset

6.2.1 Data selection

The present analysis covers the period from September 2022 (run 13315) to September 2023 (run 17663), when the ARCA neutrino telescope was operating with 21 detection units (ARCA21). The data of ARCA21 version 9 was examined, which is the first mass production achieved using the Snakemake data processing workflow. This constitutes a significant step, as it marks the transition to a more structured and automated approach to data handling within the collaboration. The runs are selected based on the unique criterion of being, as much as possible, really good and safe to prevent issues arising from low quality runs or discrepancies in the database. While standard calibration procedures correct for instrumental effects such as timing and basic run quality, other factors, such as variations in sidereal exposure or atmospheric effects (Fig. 6.1) are not fully accounted for and require additional attention in anisotropy studies. For this reason, a stringent data selection was adopted to minimize the impact of such uncorrected systematics.

To process the mass production, the following software versions were used:

Software	**Version**
JPP	18.5.0. (18.5.1 for ARCA21v9.1)
Aanet	2.5.1
MUPAGE	5.2.5

6.2.2 Detector stability

The data acquisition process in ARCA is subject to multiple factor tat may impact both the quality and reliability of the resulting dataset. These include detector stability, the operational status of photomultiplier tubes (PMTs), environmental conditions, and variations in the data acquisition system. Since the study of cosmic-ray anisotropy is particularly sensitive to such variations due to the small amplitude of the expected signal, it is essential to ensure a high level of uniformity and stability in detector performance across both time and the instrumented volume. To this end, a first set of selection criteria were established, aimed at identifying runs in which ARCA operated under stable and well-controlled conditions. This preliminary filtering step is crucial to suppress systematic effects that could mimic or obscure a genuine anisotropy signal. The data quality from data-taking runs is evaluated with the *JQAQC* program, which processes the raw data and produces a list of values referred to as quality parameters. These include, among

Fig. 6.1: Atmospheric effect on the muon count.

others, the detector livetime, the number of working PMTs, the mean and RMS of PMT hit rates, synchronization flags, and the active trigger configuration during the run. These parameters describe the detector's behaviour during each run, enabling an efficient evaluation of operational stability. To assess the stability of ARCA21v9, the following quality parameters were used:

1. The average number of working PMTs;

2. The average counting rate and its RMS.

The 3σ-rule were applied successively to these parameters, with runs lying outside the interval $(-3\sigma, +3\sigma)$ were considered outliers. Runs that significantly deviate from the mean values in any of these quality parameters are likely to indicate unusual detector conditions or environmental disturbances, and are therefore excluded from the dataset. The outcome of this selection is illustrated in Fig. 6.2. After applying this criterion, the final sample includes 1946 runs out of 2039, meaning that approximately 95% of the data satisfy this first level of quality assurance.

To check how stable the detector is over time, Fig. 6.3 illustrates the average number of working PMTs, the average counting rate of PMTs, and the RMS variation with sidereal time. These quantities provide insight into the uniformity of the detector's response over time and help to verify that no artificial modulations mimicking an anisotropy signal are introduced by instrumental effects.

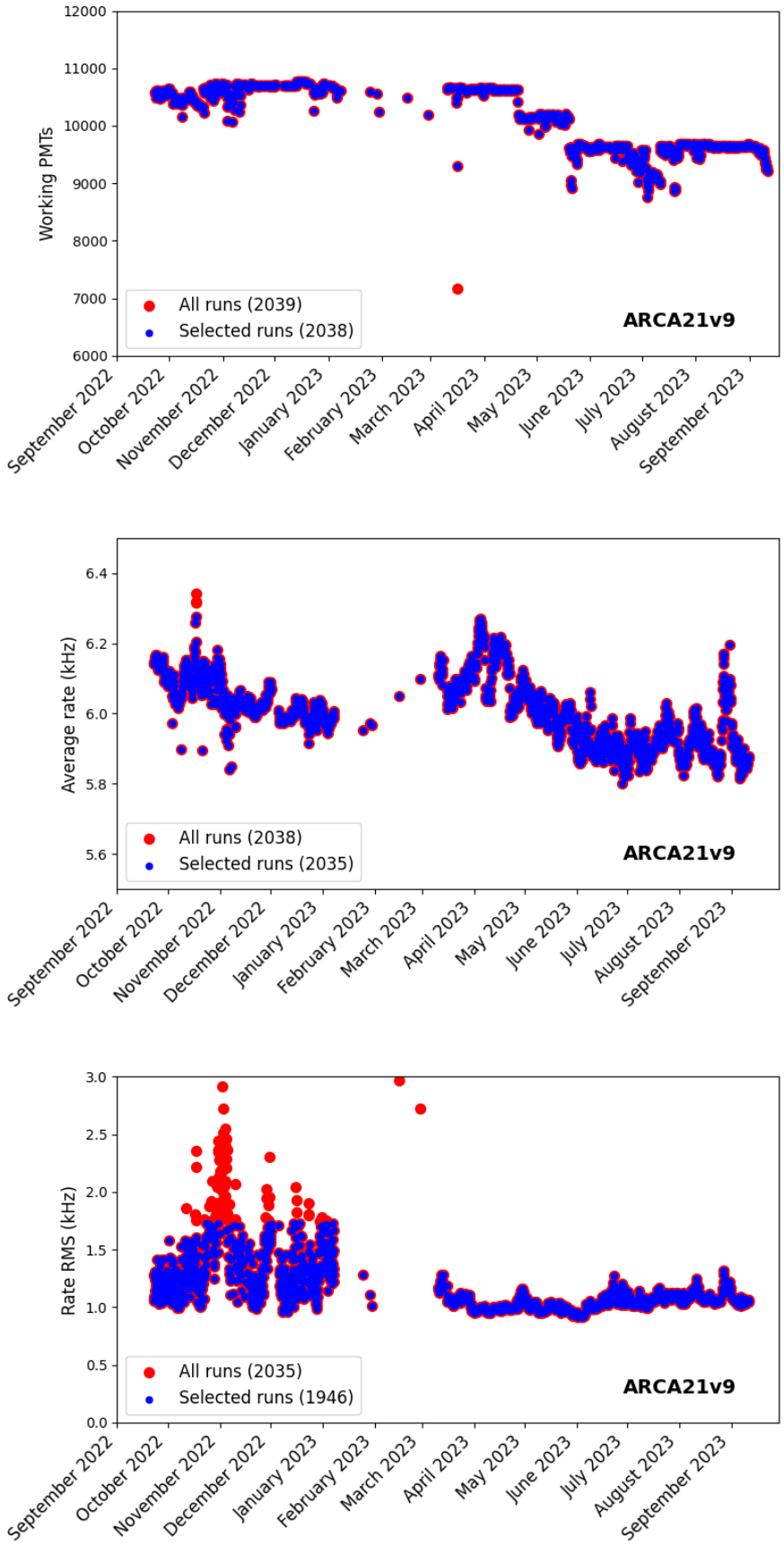

Fig. 6.2: Variation with time of the average number of working PMTs, the average counting rate, and the RMS of the counting rate in the case of ARCA21v9.

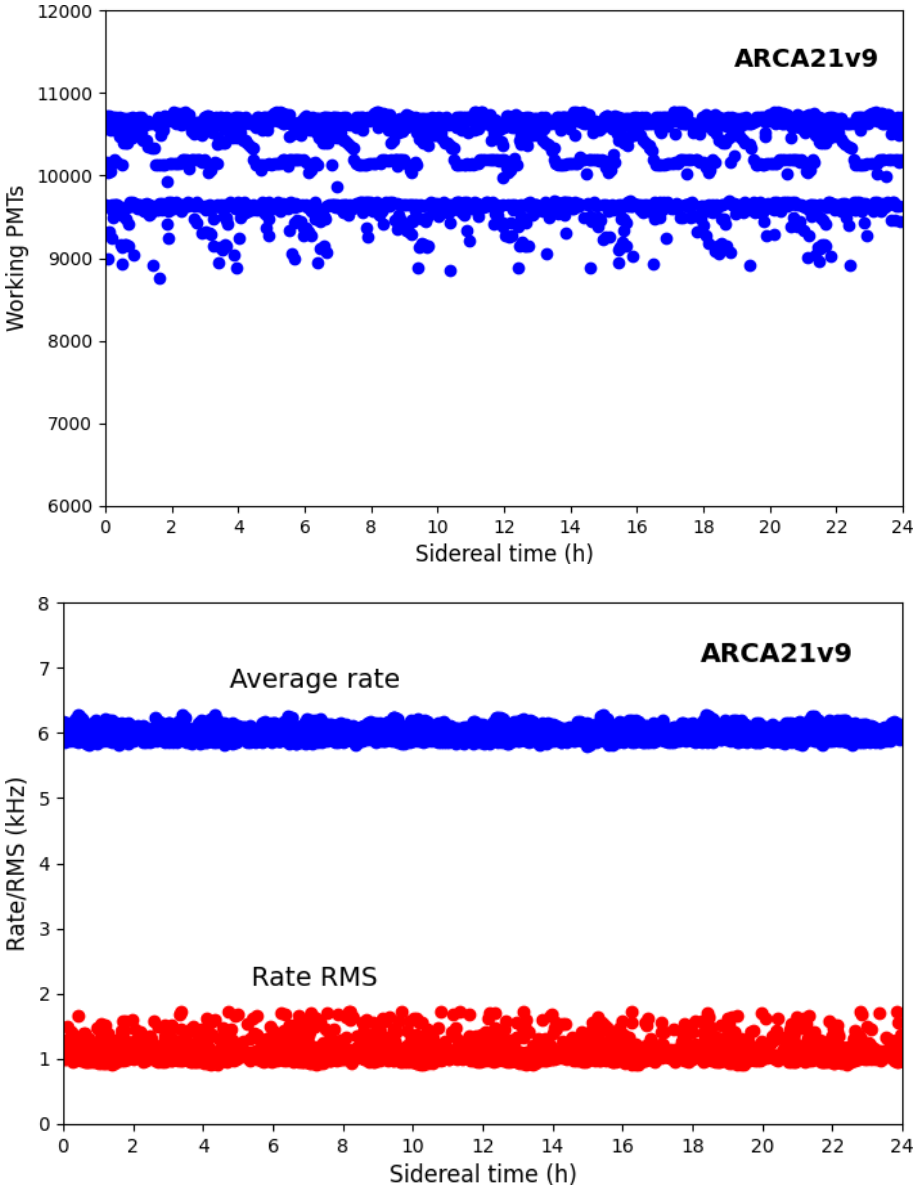

Fig. 6.3: Variation with sidereal time of the average number of working PMTs, the average counting rate, and the RMS of the counting rate in the case of ARCA21v9.

Pre-cuts	
trks[0].id != 0	Track–like events
trks[0].rec_type == 4000	JGandalf
trks[0].rec_stages >= 4	Reconstruction stages
trks[0].$E > 0$	Track energy
trks[0].lik > 0	Likelihood
trks[0].len > 0	Track length
trks[0].fitinf[0] > 0	Angular parameter (β)

Table 6.1: Summary of the pre-cuts applied to the data.

6.2.3 Monte Carlo simulations

Comparison between experimental data and Monte Carlo simulations play a central role in any analysis. They allow as to test how well the detector and its environment are understood. In principle, a good agreement between data and Monte Carlo is considered as a prerequisite for many analysis, since it ensures that the detector response, background condition and calibration conditions are well understood. The agreement between the Monte Carlo and data is achieved by applying quality cuts to the data. Monte Carlo simulations of atmospheric muons is produced on a run-by-run basis. For each data run, the measured PMT single rates, dominated by the optical background(40^K decay, bioluminescence) were used to reproduce the noise conditions, while the actual run duration were included to match the detector performance as closely as possible. Moreover, the most accurate detector calibrations (see chapter 4) were applied to simulate PMTs response, with PMT efficiencies obtained using the 40^K coincidence rates in the data.

The following analysis focuses exclusively on track-like events induced by the atmospheric muons. To retain only events with sufficient reconstruction quality, a set of pre-cuts were applied to the data from the first selection round (Table 6.1). This procedure defines a starting sample containing events with plausible values for the physical parameters, i.e.:

- a track that passes all the reconstruction stages;
- a positive track energy, a positive likelihood, and a positive track length;
- a positive angular reconstruction parameter (β).

The collected data from ARCA are dominated by events from environmental noise, i.e. bioluminescence and K-40 radioactivity (Table 6.2). These events are characterized by few hits in the detector and, thus, a reconstructed track with low likelihood. Therefore anti-noise cuts are set to eliminate these events.

Anti-noise cuts	
trks[0].lik > 50	Likelihood
trks[0].fitinf[3] > 20	Number of hits

Table 6.2: Summary of the anti-noise cuts applied to the data.

After applying the pre-cuts and the anti-noise cuts, the selected data are compared to Monte Carlo simulation for the most relevant quantities, as shown in Fig. 6.4. It can be seen that, overall, there is a good agreement between the calculated and the measured values. To further enhance the quality of data, we applied a last set of cuts, denoted first–level cuts (Table 6.3). They lead to a final sample of track-like events with:

- a maximum zenith angle of 80° to ensure that only down-going muons are kept;
- a reconstructed track length greater than 100 m;
- a track energy in the range 10^2–10^6 GeV to cover the primary cosmic–ray TeV–PeV energy range.

First-level cuts	
trks[0].dir.$\theta < 80°$	Down-going muons
$10^2 <$ trks[0].$E < 10^6$ GeV	Track energy
trks[0].len > 100	Track length

Table 6.3: Summary of the quality cuts applied to the data.

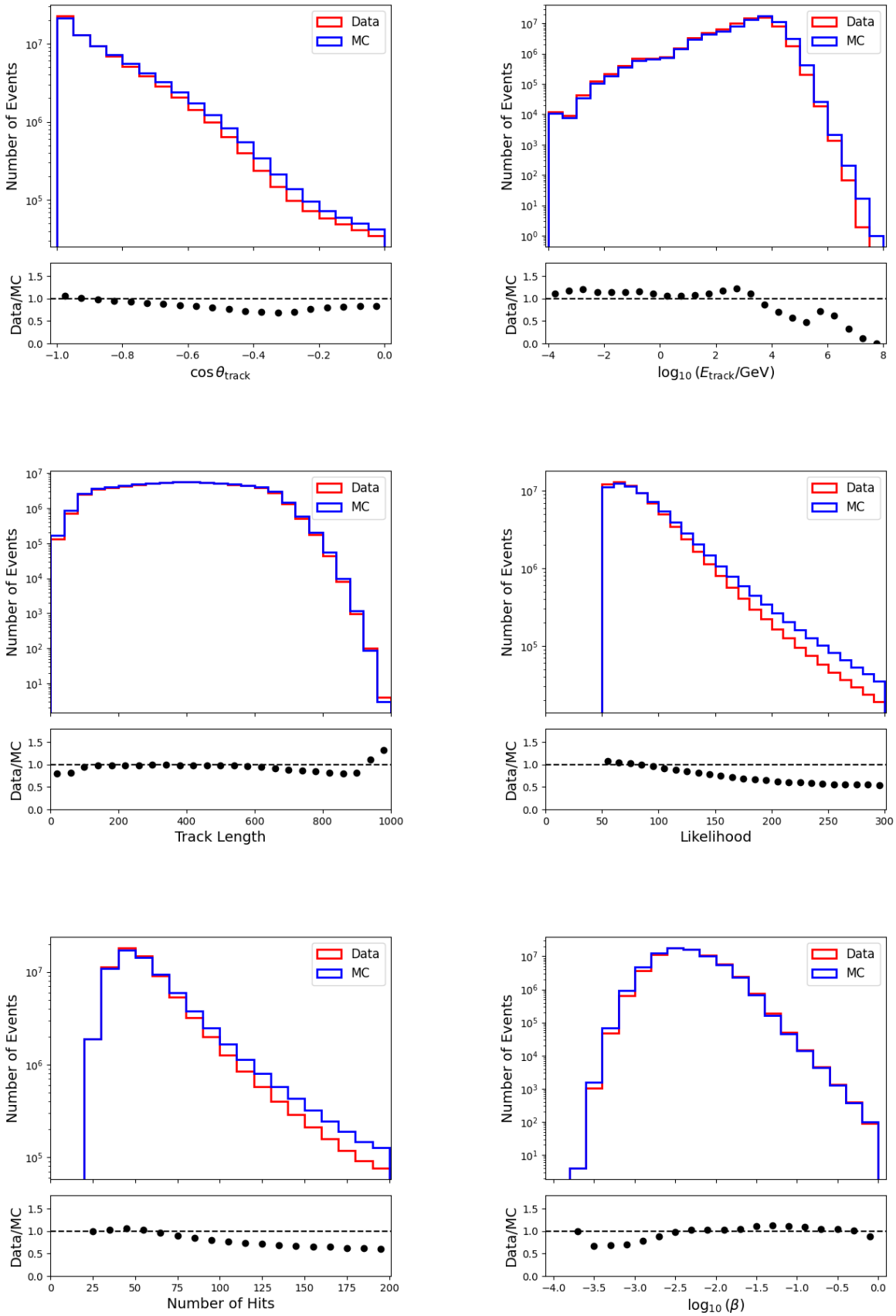

Fig. 6.4: Comparison of the selected experimental data to Monte Carlo simulation for the most relevant quantities after applying all cuts, except the first-level ones.

The plots of the different measured and calculated quantities after applying all cuts are shown in Fig. 6.5. The final sample consists of more than 55 million events, i.e., about 37% of the initial sample (Table 6.4). This dataset provides the distribution of cosmic-ray arrival directions in the northern hemisphere with a good angular resolution covering approximately one solar year. We must emphasize here that the statistics are not yet enough to thoroughly investigate a variation in the cosmic-ray flux of about 0.1% across the sky (see table 6.6). Nevertheless, this analysis can pave the way for future investigations, which will use much more statistics as the ARCA neutrino telescope grows.

Initial sample	**Pre-cuts**	**Anti-noise cuts**	**First-level cuts**
149,632,409	87,217,064	69,828,200	55,624,565
100%	58.3%	46.7%	37.2%

Table 6.4: Number of selected events (and percentage) after each phase of the selection procedure.

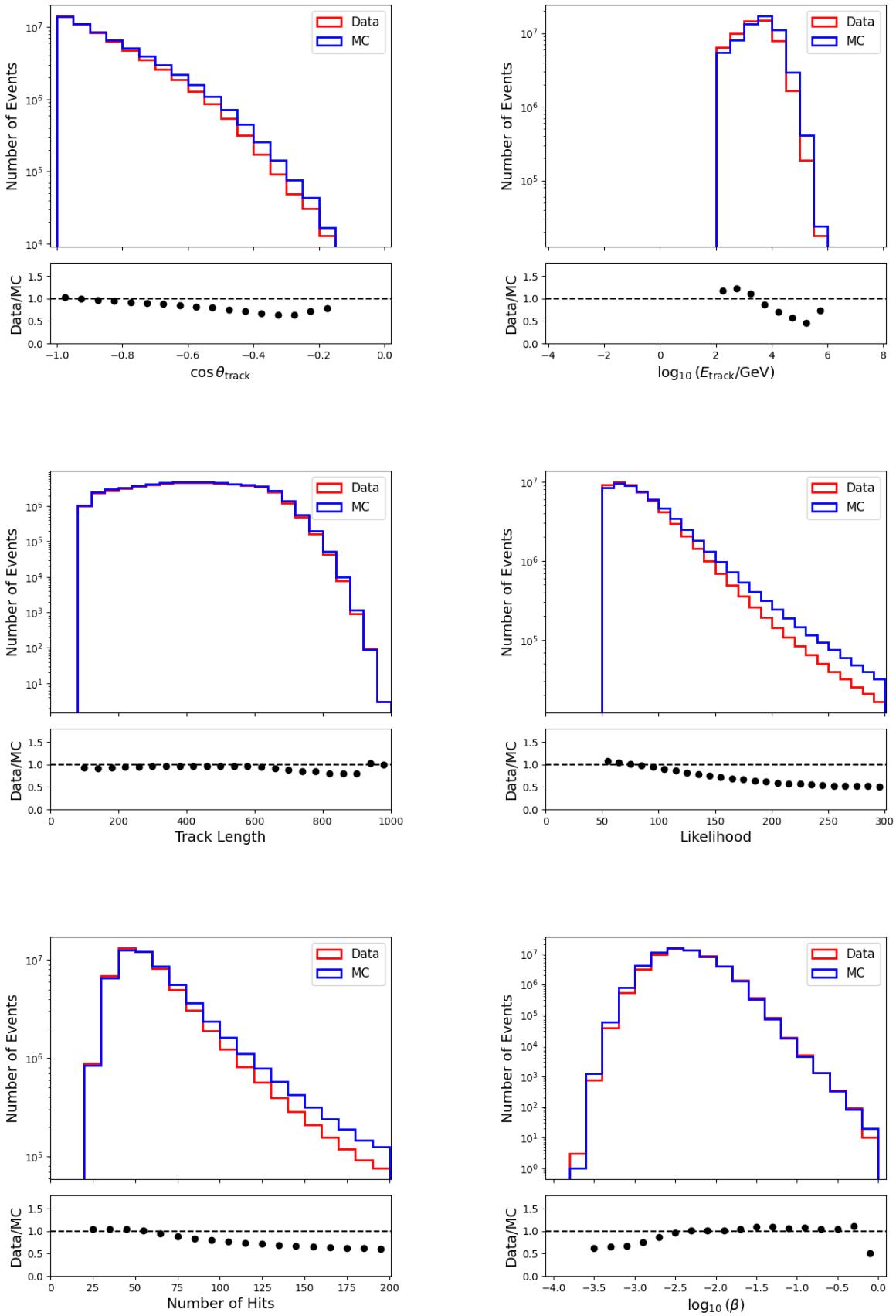

Fig. 6.5: Comparison of the selected experimental data to Monte Carlo simulation for the most relevant quantities after applying all cuts, including the first-level ones.

6.3 Azimuthal asymmetry

Fig. 6.6 presents the distributions of the true-azimuth angle (reconstructed clockwise from true North) for the three energy ranges. As shown, these distributions are not uniform. Specifically, there are less events coming from the East than from the West, which contradicts the expectations. The primary energies involved here (above TeV) exclude the possibility of geomagnetic effects. This anomaly is most likely due to the detector geometrical asymmetry. As the incident muons cross the detector, they encounter varying numbers of strings, leading to a detection efficiency that changes with the azimuth angle. This issue may arise from the limited number of detection units in ARCA21 detector and can be improved over time as the detector expands.

In order to correct for this spurious effect, we normalized the azimuthal distribution to make it uniform. Specifically, we divided the azimuth range (expressed in degrees) into $N = 360$ bins and calculated the average number of counts:

$$\overline{n} = \frac{1}{N} \sum_{i=1}^{N} n_i \tag{6.2}$$

n_i represents the number of tracks in the bin i. Then, we weighted each event with

$$w_i = \left(\frac{n_i}{\overline{n}} \right)^{-1} \tag{6.3}$$

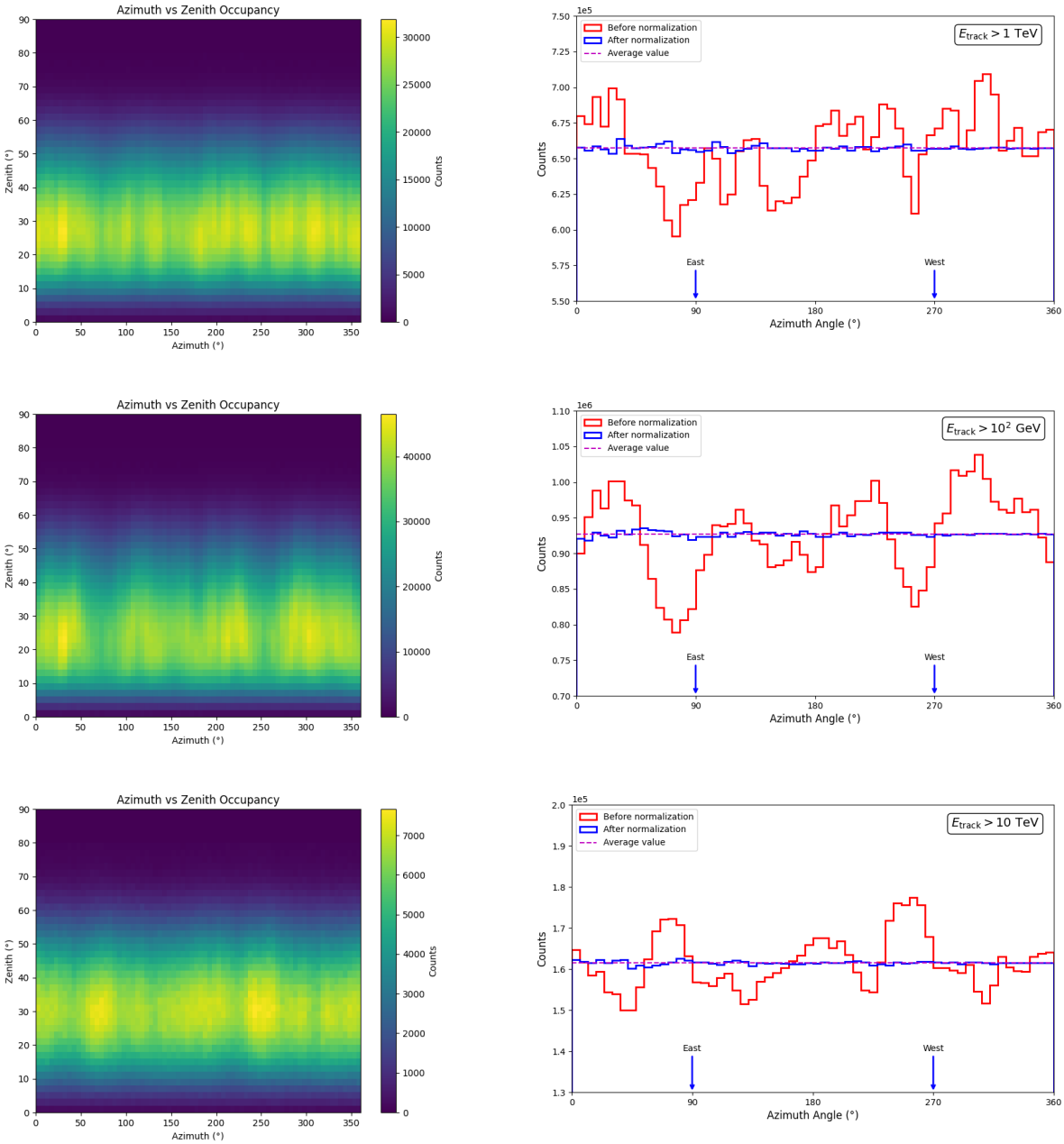

Fig. 6.6: True-azimuth angle distributions of events for the three energy ranges before and after normalization.

6.4 Sidereal anisotropy

Sidereal time is a timekeeping system based on the rotation of Earth relative to distant stars, rather than the Sun. Unlike solar time, which relies on the Sun apparent motion in the sky, sidereal time measures the duration it takes for a specific star to return to the same position in the sky. One of its key characteristics is that a sidereal day lasts 23 hours, 56 minutes, and 4 seconds, which is about 4 minutes shorter than a solar day (24 hours). The solar day is longer because Earth moves along its orbit, requiring extra rotation to align with the Sun again.

The sidereal time is closely tied to right ascension in equatorial coordinates; the right ascension of an astronomical object corresponds to the local sidereal time (LST) when the object crosses the local meridian. This time frame is particularly useful for studying cosmic-ray anisotropy.

In the KM3NeT experiment, the temporal variable recorded for each event is the Unix timestamp. The Python library Astropy can be used to derive LST from this timestamp accurately. However, this method was found to be extremely slow. Therefore, we opted to calculate LST manually using faster, though approximate, formulas.

To calculate the LST of the selected events, we first converted Unix time (t) to Julian date (JD):

$$\mathrm{JD} = \frac{t}{86400} + 2440587.5 \tag{6.4}$$

86400 is the number of seconds in a day and 2440587.5 is the Julian Date of 1970-01-01 00:00:00 UTC. Next, we computed Julian century (T) since J2000.0 (January 1, 2000, 12:00:00 UTC):

$$T = \frac{JD - 2451545}{36525} \tag{6.5}$$

Then, we calculated the Greenwich Mean Sidereal Time (GMST) in degrees:

$$\begin{aligned} GMST = 280.46061837 + 360.98564736629 \times (JD - 2451545) \\ + 0.000387933\,T^2 - \frac{T^3}{38710000} \pmod{360} \end{aligned} \tag{6.6}$$

Finally, we converted GMST to LST by adjusting to ARCA longitude λ (in degrees):

$$\mathrm{LST} = \mathrm{GMST} + \lambda \pmod{360} \tag{6.7}$$

Another important quantity in our analysis is the hour angle (HA) of the selected events, which is defined as

$$\mathrm{HA} = \mathrm{LST} - \mathrm{RA}$$

where RA is the right ascension. We calculated the two average values of HA for events coming from the East and from the West. Then, we calculated the mean hour angle between the two sectors (δt). The obtained results are given below.

E_{track} (GeV)	$> 10^2$	$> 10^3$	$> 10^4$
δt (h)	1.71	1.83	1.93

Table 6.5 presents the characteristics of the first harmonic in sidereal time, obtained by using the East-West method with a time bin width of 20 min (corresponding to 5° of angular aperture) for the three energy ranges. The amplitude values obtained are consistent with what is expected ($\sim 10^{-3}$).

However, the Rayleigh probabilities are high, resulting in low statistical significance ($\approx 2\sigma$ for the two first energy ranges). This issue stems from the size of our dataset, which is not yet large enough. By applying the Rayleigh probability formula, it is possible to estimate the number of events (N) required to achieve a pre-defined significance. As shown in Table 6.6, 86 million events are required to achieve 3σ significance and around 210 million for 5σ significance. Currently, our dataset consists of about 55 million events, meaning we are still falling short of the required numbers. However, this situation is expected to improve over time with the increase in statistics.

$$N = -\frac{4 \ln P}{r^2 \, \delta t^2} \tag{6.8}$$

where P is Rayleigh probability. Assuming an amplitude of 10^{-3} and a mean hour angle $\delta t \approx 2$ h, we calculated N for 3σ and 5σ statistical significance (6.6).

The statistical significance of the observed signal is low, well below the standard threshold (typically 3σ) to claim detection. Consequently the upper limits (UL) of the amplitudes at a 99% confidence level (CL) were computed. These limits are derived from based on the distribution drawn from the distribution of a population characterized by an anisotropy with unknown amplitude and phase [1]:

$$\sqrt{\frac{2}{\pi}} \, \frac{1}{I_0(r^2/4\sigma^2)} \int_0^{r_{\mathrm{UL}}} \frac{\mathrm{d}s}{\sigma} \, I_0\left(\frac{rs}{\sigma^2}\right) \exp\left(-\frac{s^2 + r^2/2}{2\sigma^2}\right) = \mathrm{CL} \tag{6.9}$$

E_{track} (GeV)	Amplitude ($\times 10^{-3}$)	No. of events ($\times 10^6$)	Phase ($^\circ$)	Rayleigh probability	Statistical significance	UL ($\times 10^{-3}$)
$> 10^2$	1.0 ± 0.4 (1.3 ± 0.1)	55.62	-15 ± 25 (-48 ± 3)	6.8%	1.83σ	1.9
$> 10^3$	1.0 ± 0.5 (1.5 ± 0.1)	39.44	-40 ± 26 (-62 ± 4)	8.4%	1.73σ	2.0
$> 10^4$	0.8 ± 0.9 (0.9 ± 0.1)	9.69	-14 ± 63 (-31 ± 8)	66.5%	0.43σ	2.7

Table 6.5: Characteristics of the first harmonic in sidereal time obtained for a time bin width of 20 min in the three energy ranges. The values in parentheses represent the direct fitting of the reconstructed true intensity in relative value. The last column gives the 99% CL UL for the amplitudes.

Significance	P	N
3σ	2.70×10^{-3}	86×10^6
5σ	5.74×10^{-7}	210×10^6

Table 6.6: Number of events required to achieve 3σ and 5σ statistical significance using the Rayleigh probability.

where I_0 represents the modified Bessel function of the first kind with order 0. The results obtained are shown in the last column of Table 6.5.

In addition, we derived the amplitudes and phases of the first harmonic from directly fitting the reconstructed true intensity in relative value. As shown in Table 6.5, the results from both methods are statistically compatible within their uncertainties.

The true muon intensity I detected by ARCA21 can be obtained by integrating equation (2.14):

$$I(t) = \langle I \rangle + \frac{1}{\delta t} \int_0^t D(t)\, \mathrm{d}t \tag{6.10}$$

where $\langle I \rangle$ denotes the average value of observed intensity. This equation can then be solved numerically with the use of the following relation:

$$I(t_k) \approx \langle I \rangle + \frac{\Delta t}{\delta t} \sum_{i=1}^{n_k} D(t_k) \tag{6.11}$$

Δt represents the time bin width (= 20 min) and t_k denotes the center of time bin k. n_k takes the values from 1 to 72 (corresponding to 72 time bins).

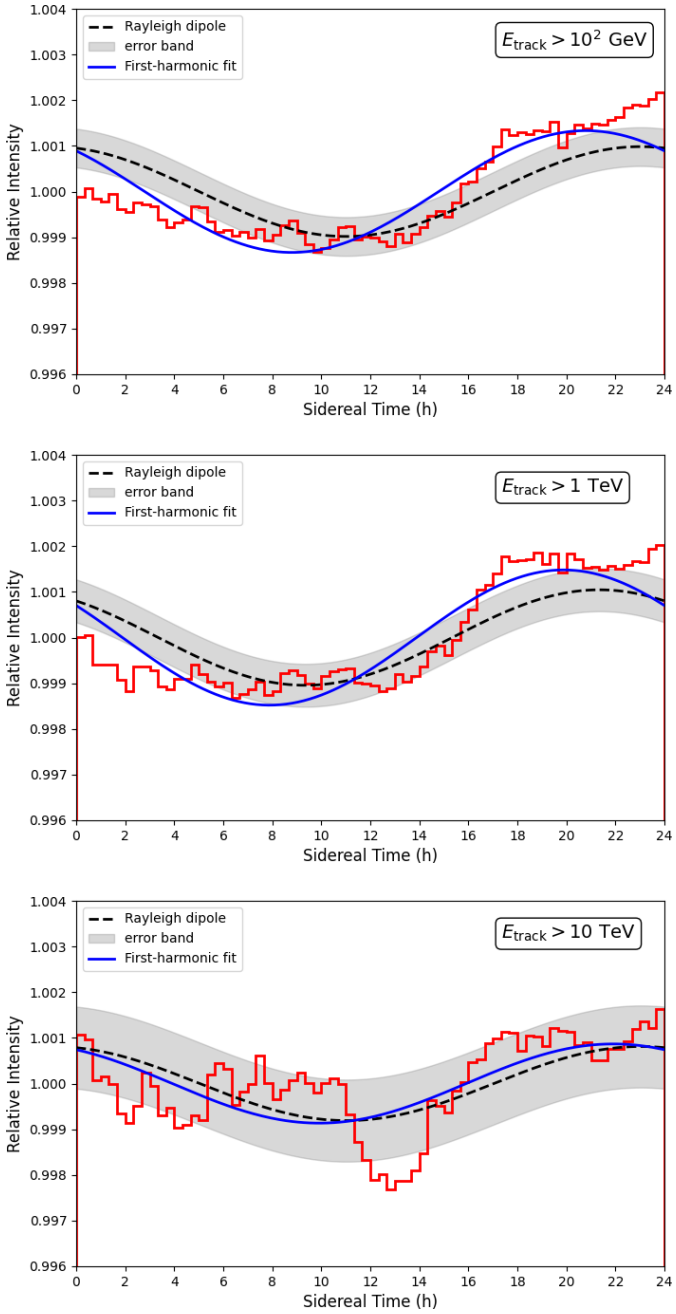

Fig. 6.7: Sidereal time variation of the reconstructed relative true intensity obtained using the East-West method with a time bin width of 20 min for the three energy ranges [2].

Fig. 6.7 illustrates the variation in sidereal time of the relative reconstructed true intensity obtained using the East-West method. The dashed curve represents the dipole obtained with the Fourier coefficients; the blue curve is the direct fit to the results. As shown, we can observe a clear sidereal modulation with peaks occurring at about 21–23 h. This pattern suggests the presence of a dipolar galactic anisotropy in the distribution of cosmic-ray arrival directions observed with ARCA21. To better evaluate the accuracy of these results, it is important to examine the systematic effects.

6.5 Systematic effects

To demonstrate that there are no significant unaccounted systematics effects, we analyzed the first harmonic in solar and anti-sidereal time frames. In each case, we followed the same procedure as we did for the sidereal time frame, using the East-West method along with the azimuthal correction.

To calculate the local solar time (ST) of the selected events, we first converted Unix time to Julian date (JD) using equation (6.4). Next, we extracted the fraction of the day since local midnight:

$$\text{day\_fraction} = JD \pmod 1 \tag{6.12}$$

and converted it to degrees:

$$ST\ (^\circ) = \text{day\_fraction} \times 360 \tag{6.13}$$

Then, we adjusted to ARCA longitude λ to get the local solar time (ST_{local}) and corrected for Earth orbit and axis tilt by applying the equation of time (EoT) [3]:

$$ST_{\text{local}} = ST + \lambda + \text{EoT} \pmod{360} \tag{6.14}$$

It bears noting that these calculations give pure-solar time that does not include time zone corrections.

Anti-sidereal time is a timekeeping system defined as the mirror opposite of sidereal time in relation to solar time [4]. It is based on a day length of 24.07 h, instead of the standard 23.93 h sidereal day. Thus, a sidereal year is about 365.25 days, and an anti-sidereal year is about 364.25 days. Unlike sidereal anisotropy, anti-sidereal variations are not expected in primary cosmic rays and often result from systematic effects in data processing.

To calculate the local anti-sidereal time of the selected events, we first converted Unix time to Julian date (JD) using equation (6.4). Next, we calculated the number of days since J2000.0:

$$\text{days\_since\_j2000} = JD - 2451545 \tag{6.15}$$

Then, we computed anti-sidereal time (AST) in degrees:

$$AST = \text{days\_since\_j2000} \times \frac{364.25}{365.25} \times 360 \pmod{360} \tag{6.16}$$

	Amplitude ($\times 10^{-3}$)	Phase ($^\circ$)	Rayleigh probability	E_{track} (GeV)
Sidereal time	1.0 ± 0.4	-15 ± 25	6.8% (1.8σ)	
Solar time	0.9 ± 0.4	-104 ± 27	10.2% (1.6σ)	$> 10^2$
Anti-sidereal time	0.7 ± 0.4	44 ± 34	23.7% (1.2σ)	
Sidereal time	1.0 ± 0.5	-40 ± 26	8.4% (1.7σ)	
Solar time	0.6 ± 0.5	-117 ± 44	42.2% (0.8σ)	$> 10^3$
Anti-sidereal time	0.6 ± 0.5	35 ± 42	39.2% (0.9σ)	
Sidereal time	0.8 ± 0.9	-14 ± 63	66.5% (0.4σ)	
Solar time	1.3 ± 0.9	171 ± 40	36.0% (0.9σ)	$> 10^4$
Anti-sidereal time	1.3 ± 0.9	-8 ± 40	36.3% (0.9σ)	

Table 6.7: Amplitude, phase, and Rayleigh probability of the first harmonic in sidereal, solar, and anti-sidereal time for the three energy ranges.

Then, we adjusted to ARCA longitude λ to get the local anti-sidereal time ($LAST$):

$$LAST = AST + \lambda \qquad (\text{mod } 360) \tag{6.17}$$

Table 6.7 gives the amplitude, phase, and Rayleigh probability of the first harmonic in sidereal, solar, and anti-sidereal time for the three energy ranges. For the first energy range ($E_{\text{track}} > 10^2$ GeV), the dipole amplitudes and the Rayleigh probabilities are comparable in both sidereal and solar times. We conclude that the observed cosmic-ray anisotropy in this energy range can be either local or of galactic origin. In the third energy range ($E_{\text{track}} > 10^4$ GeV), the dipole amplitudes are similar in all three time frames, but the Rayleigh probability is highest in sidereal time. This suggests that the observed anisotropy is either local or influenced by systematic effects, making the galactic origin the least likely explanation. The second energy range ($E_{\text{track}} > 10^3$ GeV) is the most interesting case. In this range, the dipole amplitude is at its highest, while the Rayleigh probability is at its lowest in sidereal time, indicating a potential genuine signal. In contrast, the solar and anti-sidereal modulations show higher Rayleigh probabilities, corroborating the argument that the sidereal anisotropy is most likely of galactic origin rather than being a local effects or an artefact of the detector. Although the statistical significance of this observation is currently small (about 2σ), it is expected to improve in the coming years as ARCA expands and the statistical data increase.

Fig. 6.8 presents the variation in solar time and anti-sidereal time of the relative reconstructed true intensity obtained using the East-West method with a time bin width of 20 min for the three energy ranges. The dashed line represents the dipole calculated by means of the Fourier coefficients.

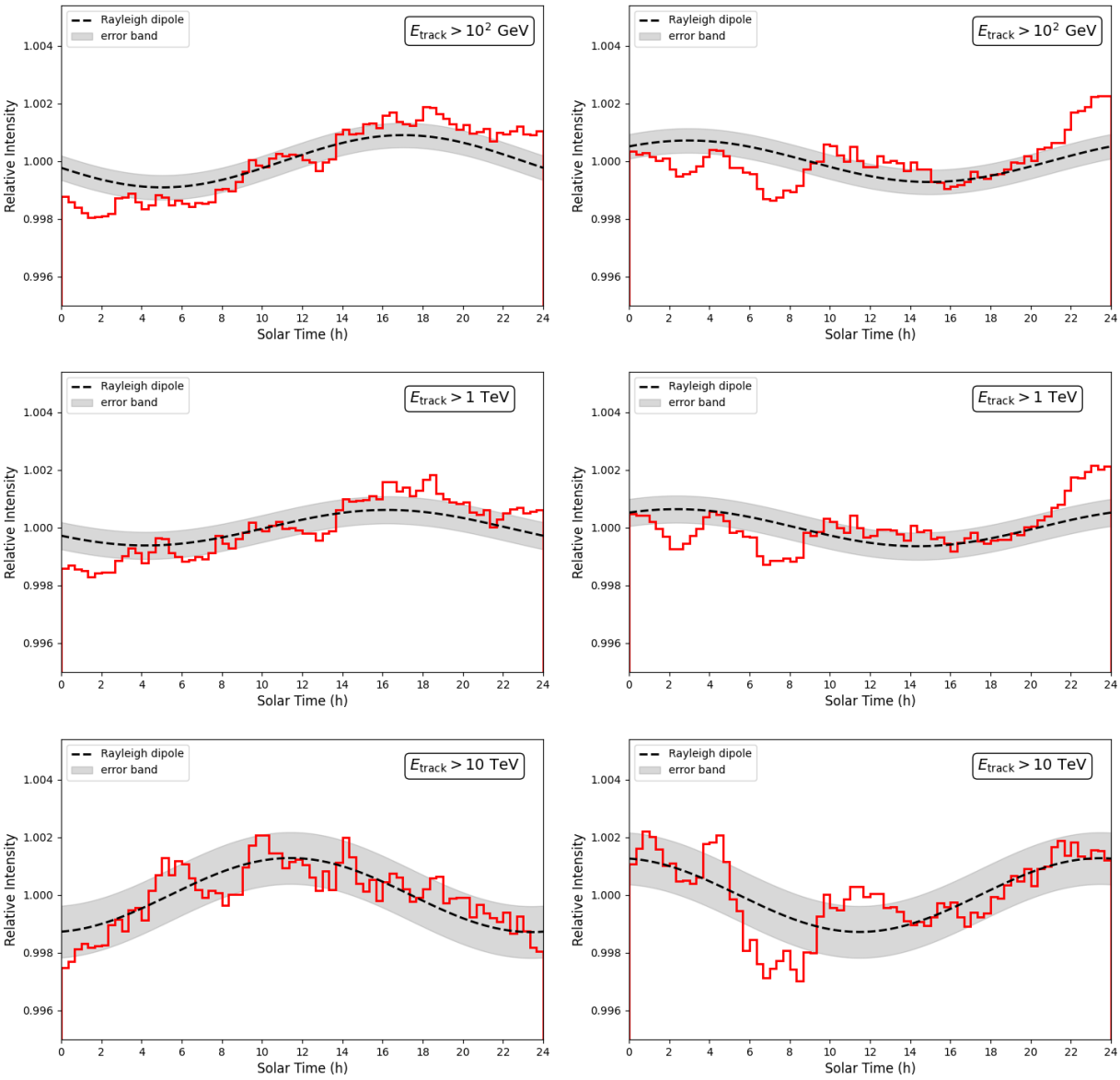

Fig. 6.8: Solar time and anti-sidereal time variation of the reconstructed relative true intensity obtained using the East-West method with a time bin width of 20 min for the three energy ranges.

6.6 Data/Simulation comparison

In order to further validate the presence of a large-scale anisotropy in the arrival direction distribution of cosmic rays, we have compared the observed data with the reconstructed events from Monte Carlo simulations. Of interest in this case are the events whose reconstructed track energies exceed 1 TeV, for which the signature of anisotropy will be better observed and statistically significant. Most notably, the comparison is within the three various time intervals: sidereal time; solar time and anti-sidereal time. As seen in table 6.7, the sidereal time analysis of the data indicates a statistically significant and clear deviation from isotropy. The first harmonic amplitude in this reference frame is

determined to be $(1.0 \pm 0.5) \times 10^{-3}$, with phase $-40° \pm 26°$, and corresponding Rayleigh probability of 8.4% which indicates a local significance of 1.7σ. This result suggests the presence of a dipolar modulation in the arrival directions of cosmic rays, and statistically distinguishable from a uniform distribution. By contrast, the amplitudes obtained from solar and anti-sidereal time are much smaller each $(0.6 \pm 0.5) \times 10^{-3}$ and with Rayleigh probabilities of 42.2% and 39.2%, respectively. They are consistent with statistical fluctuations due to an underlying isotropic flux, i.e., the modulation observed in sidereal time is not present in time scales that could be subject to atmospheric or diurnal effects. The provided Monte Carlo simulations (table 6.8), which were constructed run by run to mimic the actual detector conditions and time-dependent performance, show no evidence of anisotropy in any of the time frames examined. In sidereal time, the first harmonic amplitude extracted from the simulated events is only $(0.3 \pm 0.4) \times 10^{-3}$ with a Rayleigh probability of 73.7%, clearly within the range expected from isotropic random fluctuations. We observe comparable behavior in solar and anti-sidereal time, with amplitudes of $(0.2 \pm 0.4) \times 10^{-3}$ and $(0.1 \pm 0.4) \times 10^{-3}$ and probabilities greater than 86%. The variation with sidereak time in this case is shown in Figure 6.9. The result is of utmost importance it demonstrates that the full analysis chain from reconstruction to event selection and exposure modeling does not artificially mimic anisotropic patterns. This provides a robust null hypothesis baseline with which the data can be confidently compared. Additionally, the Tables 6.8 present a comparison of the first harmonic amplitude, phase, and Rayleigh probability for both data and Monte Carlo events with $E_{track} > 0.1TeV$ and $E_{track} > 10TeV$, respectively, evaluated in sidereal, solar, and anti-sidereal frames.

Taken together, the clear identification of a dipolar modulation in the sidereal frame in real data and the fact that such effects do not occur within Monte Carlo runs and within solar or anti-sidereal frames strongly supports the hypothesis that the anisotropy observed is of astrophysical origin. The sidereal modulation, in particular, aligns with expectations for a cosmic-ray dipole arising from either large-scale Galactic magnetic field structures or propagation effects in the interstellar medium. The fact that no such modulation is observed in solar or anti-sidereal coordinates further indicates that instrumental effects, detector instabilities, or atmospheric modulations are unlikely to be responsible. The high compatibility of the simulation with isotropy across all frames serves as a stringent test of systematics and reinforces the robustness of our analysis framework.

$E_{\text{track}} > 0.1$ TeV	Amplitude ($\times 10^{-3}$)	Phase (°)	Rayleigh probability	
Sidereal time	1.0 ± 0.4	-15 ± 25	6.8% (1.8σ)	
Solar time	0.9 ± 0.4	-104 ± 27	10.2% (1.6σ)	Data
Anti-sidereal time	0.7 ± 0.4	44 ± 34	23.7% (1.2σ)	
Sidereal time	0.1 ± 0.4	236 ± 173	94.67% (0.07σ)	
Solar time	0.7 ± 0.4	94 ± 32	19.86% (1.29σ)	Monte Carlo
Anti-sidereal time	0.39 ± 0.4	48 ± 58	61.71%(0.50σ)	

$E_{\text{track}} > 1$ TeV	Amplitude ($\times 10^{-3}$)	Phase (°)	Rayleigh probability	
Sidereal time	1.0 ± 0.5	-40 ± 26	8.4% (1.7σ)	
Solar time	0.6 ± 0.5	-117 ± 44	42.2% (0.8σ)	Data
Anti-sidereal time	0.6 ± 0.5	35 ± 42	39.2% (0.9σ)	
Sidereal time	0.3 ± 0.4	-49 ± 73	73.7% (0.3σ)	
Solar time	0.2 ± 0.4	51 ± 108	86.9% (0.2σ)	Monte Carlo
Anti-sidereal time	0.1 ± 0.4	84 ± 142	92.2% (0.1σ)	

$E_{\text{track}} > 10$ TeV	Amplitude ($\times 10^{-3}$)	Phase (°)	Rayleigh probability	
Sidereal time	0.8 ± 0.9	-14 ± 63	66.5% (0.4σ)	
Solar time	1.3 ± 0.9	171 ± 40	36.0% (0.9σ)	Data
Anti-sidereal time	1.3 ± 0.9	-8 ± 40	36.3% (0.9σ)	
Sidereal time	0.3 ± 0.7	-16 ± 116	88.61% (0.14σ)	
Solar time	0.5 ± 0.7	50 ± 70	71.89% (0.36σ)	Monte Carlo
Anti-sidereal time	0.4 ± 0.7	268 ± 99	84.70%(0.19σ)	

Table 6.8: Comparison of the first harmonic amplitude, phase, and Rayleigh probability for data and Monte Carlo events with $E_{\text{track}} > 0.1$ TeV, $E_{\text{track}} > 1$ TeV and $E_{\text{track}} > 10$ TeV respectively evaluated in sidereal, solar, and anti-sidereal time.

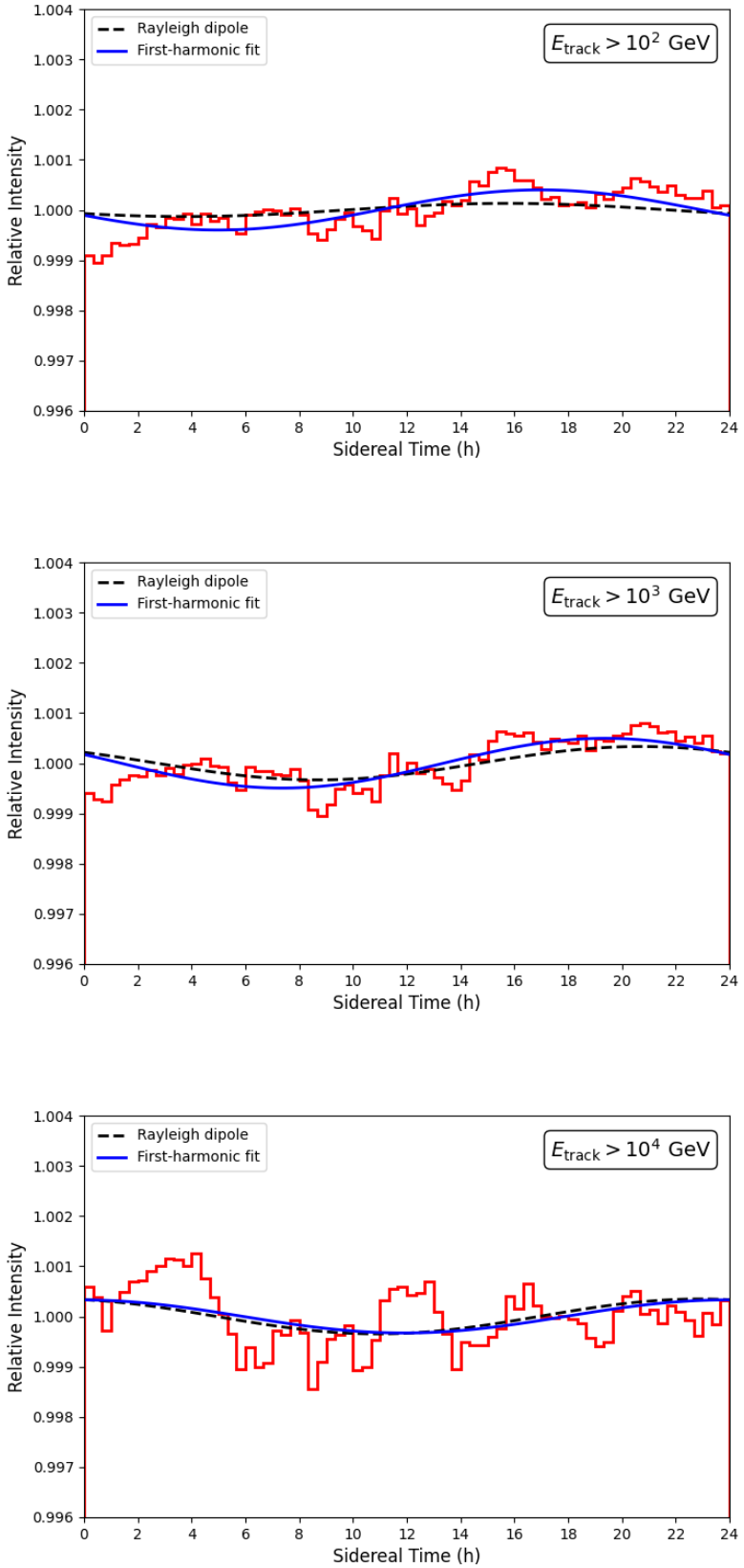

Fig. 6.9: Monte Carlo sidereal time variation of the reconstructed relative true intensity obtained using the East-West method with a time bin width of 20 min for the three energy ranges using.

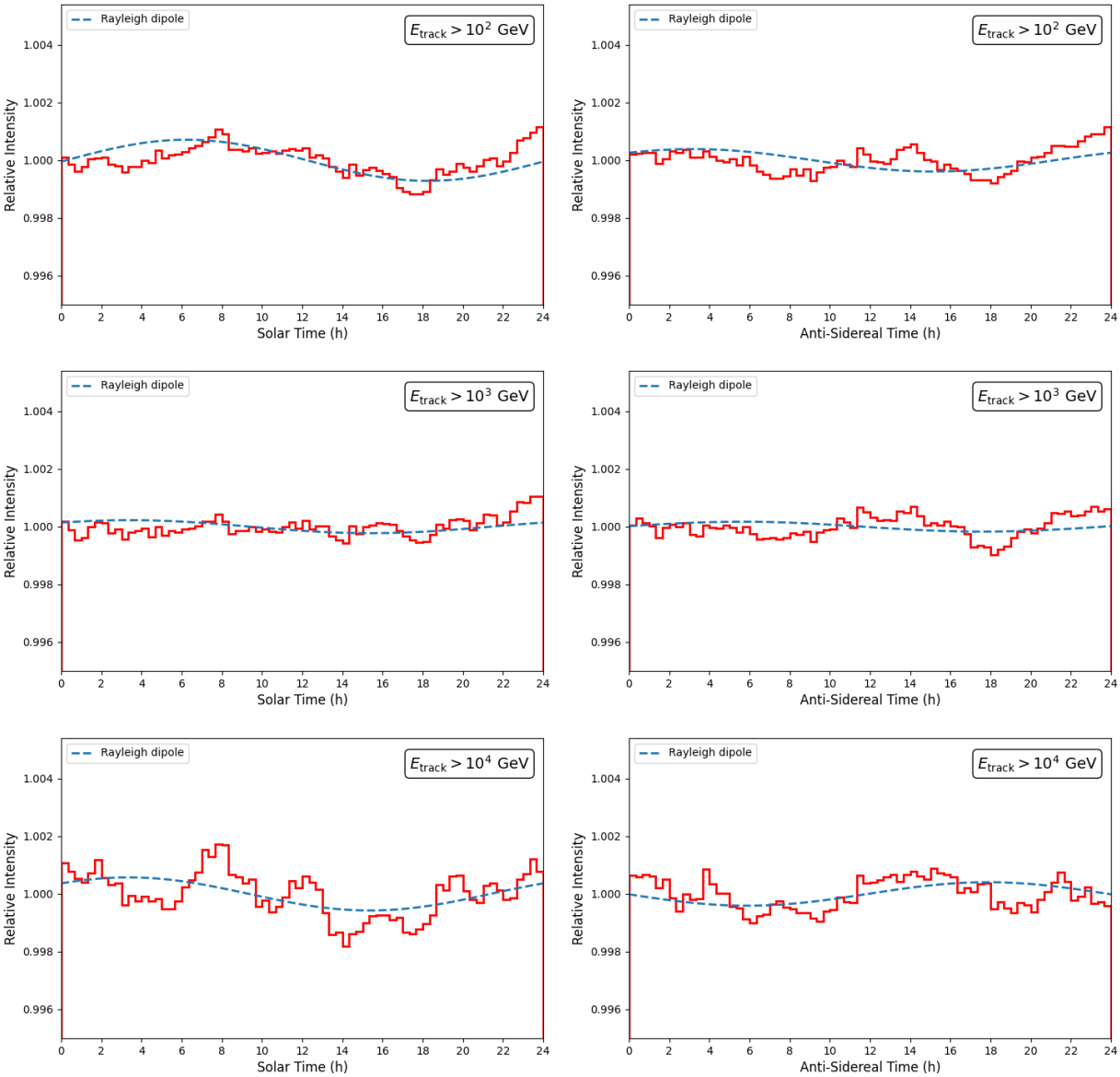

Fig. 6.10: Monte Carlo solar time and anti-sidereal time variation of the reconstructed relative true intensity obtained using the East-West method with a time bin width of 20 min for the three energy ranges.

6.7 Comparison with other experiments

Different experiments often report the amplitude and phase of the first-harmonic of cosmic-ray anisotropy as a function of the primary cosmic-ray median energy. To estimate the primary median energies for our three energy ranges without relying to extensive Monte Carlo simulations, we used the approximation relation that a muon energy at sea level (E_μ^0) is about 5 to 10% of the energy of it primary particle. This estimate is valid for primaries up to PeV energies. We determined the muon energy at sea level by adding the reconstructed track energy to the energy lost during the propagation to ARCA, estimated at roughly 1 TeV. This value accounts for highly inclined muon trajectories. From this, we estimated the two corresponding primary energies E_0:

$$E_0^{(1)} = \frac{E_\mu^0}{0.1} = 10\, E_\mu \qquad\qquad E_0^{(2)} = \frac{E_\mu^0}{0.05} = 20\, E_\mu \tag{6.18}$$

Next, we calculated the primary median energy (E_m) by taking into account the cosmic ray differential energy spectrum, which decreases with energy following a power law ($\propto E^{-\gamma}$) with a spectral index $\gamma = 2.7$ in the TeV–PeV energy region:

$$E_\mathrm{m} = \left(\frac{E_\mathrm{max}^{1-\gamma} + E_0^{1-\gamma}}{2}\right)^{\frac{1}{1-\gamma}} \approx 1.5\, E_0 \qquad (E_\mathrm{max} \gg E_0) \tag{6.19}$$

There are two values of the primary median energy for each track threshold energy. We then calculated the average value and defined the uncertainty as half the interval between the two values:

$$\overline{E}_\mathrm{m} = \frac{E_\mathrm{m}^{(1)} + E_\mathrm{m}^{(2)}}{2} \qquad \Delta E_\mathrm{m} = \frac{E_\mathrm{m}^{(2)} - E_\mathrm{m}^{(2)}}{2} \tag{6.20}$$

The resulting values (in TeV) of the median energy for our three energy intervals are:

$$25 \pm 8 \qquad 45 \pm 15 \qquad 248 \pm 83$$

Fig. 6.11 compares the results of this work (indicated by the red circle) with those from other experiments. The plot presents the amplitude and phase of the first harmonic as a function of primary median energy. Fig. 6.12 shows the most significant of our results, which corresponds to the median energy of 45 TeV. As can be seen, the upper limit of the dipole anisotropy observed by ARCA21 is consistent with measurements from other experiments. It should be noted that in the present estimate, uncertainties in the reconstructed muon track energy have not been taken into account. These arise from the finite resolution of the track reconstruction algorithms, variation in detector response

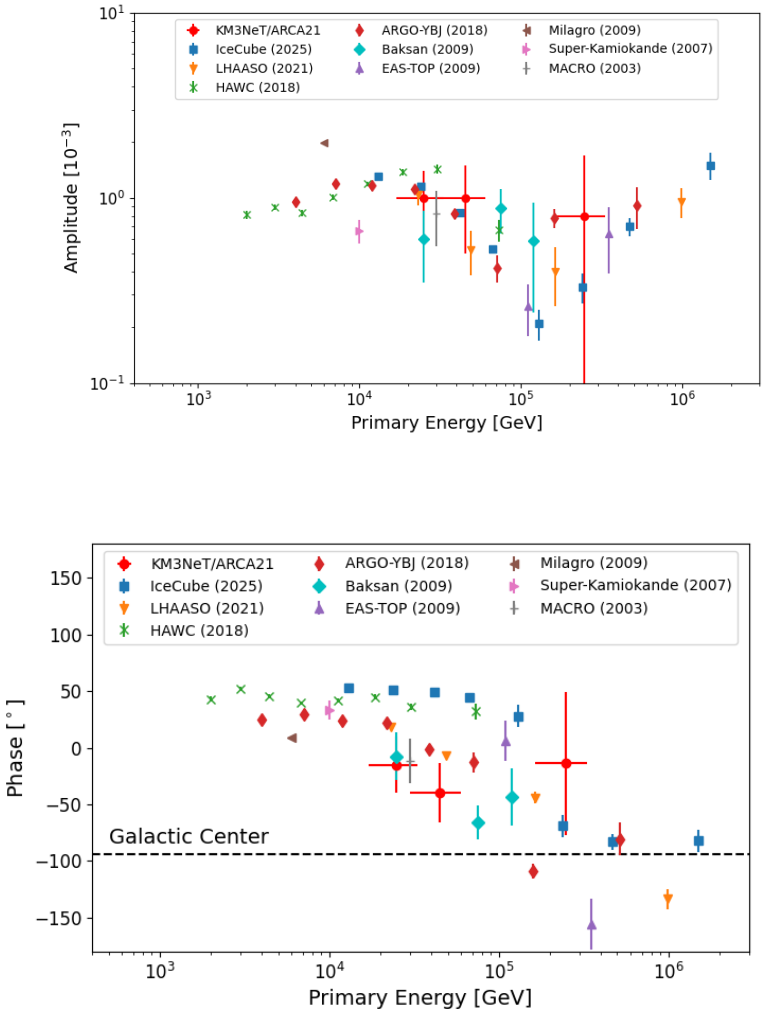

Fig. 6.11: Comparison of the amplitude and phase of the first harmonic obtained with ARCA21 in the TeV-PeV energy range to experimental data from IceCube [5], LHAASO [6], HAWC [7], ARGO-YBJ [8], Baksan [9], EAS-TOP [10], Milagro [11], Super-Kamiokande [12], and MACRO [13].

(PMT efficiencies and optical background), uncertainties in the optical properties of water, which affect the propagation of Cherenkov light. This will be addressed in future works to improve the estimation of primary median energies and their associated uncertainties.

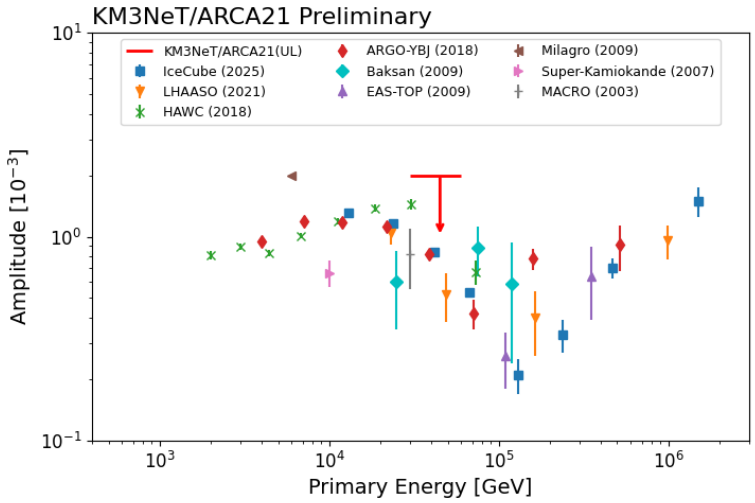

Fig. 6.12: Amplitude upper limit of the most significant energy range [2].

References

[1] J. Linsley, *Phys. Rev. Lett.*, vol. 34, p. 1530, 1975. DOI: 10.1103/PhysRevLett.34.1530.

[2] A. B. Bouasla and R. Attallah, *Proc. 39th Int. Cosmic Ray. Conf.*, vol. PoS(ICRC2025)202, DOI: 10.22323/1.501.0202.

[3] J. Meeus, *Astronomical algorithms*. Willmann-Bell; 2nd Edition, 1998.

[4] F. J. M. Farley and J. R. Storey, *Proc. Phys. Soc. A*, vol. 67, p. 996, 1954. DOI: 10.1088/0370-1298/67/11/306.

[5] R. Abbasi *et al.*, *Astrophys. J.*, vol. 981, p. 182, 2025. DOI: 10.3847/1538-4357/adb1de.

[6] W. Gao *et al.*, *Int. Cosmic Ray Conf.*, vol. (ICRC2021), p. 351, 2021. DOI: 10.22323/1.395.0351.

[7] A. U. Abeysekara *et al.*, *Astrophys. J.*, vol. 865, no. 1, p. 57, 2018. DOI: 10.3847/1538-4357/aad90c.

[8] B. Bartoli *et al.*, *Astrophys. J.*, vol. 861, p. 93, 2018. DOI: 10.3847/1538-4357/aac6cc.

[9] V. V. Alekseenko *et al.*, *Nucl. Phys. B - Proc. Suppl.*, vol. 196, p. 179, 2009. DOI: 10.1016/j.nuclphysbps.2009.09.032.

[10] M. Aglietta *et al.*, *Astrophys. J. Lett.*, vol. 692, p. L130, 2009. DOI: 10.1088/0004-637X/692/2/L130.

[11] A. A. Abdo *et al.*, *Astrophysical Journal*, vol. 698, p. 2121, 2009. DOI: 10.1088/0004-637X/698/2/2121.

[12] G. Guillian *et al.*, *Phys. Rev. D*, vol. 75, no. 6, p. 062 003, 2007. DOI: 10.1103/PhysRevD.75.062003.

[13] M. Ambrosio *et al.*, *Phys. Rev. D*, vol. 67, p. 042 002, 2003. DOI: 10.1103/PhysRevD.67.042002.

Conclusion

In this thesis, we started by studying the properties of atmospheric muons at sea level, where we measured their flux and charge ratio. These measurements are fundamental importance as they provide insights into the interaction of primary cosmic rays with the atmosphere. Since muons are the most abundant charged particles reaching underground/underwater detectors, their flux and charge ratio encode valuable information about the energy spectrum and mass composition of the primaries that initiated them. In addition, these results serve as an essential reference point for interpreting signals observed in deep underwater detectors like ARCA as the muons detected in ARCA originate from the same atmospheric interactions. By understanding their behaviour at sea level, we gain a complementary perspective that strengthens our interpretation of muon background recorded in ARCA and this is valuable for cosmic-ray anisotropy studies where even small systematic effects in the muon flux can mimic or obscure real astrophysical signals.

The second part of the thesis was dedicated to cosmic ray anisotropy. We were able to extract for the first time a large-scale dipole anisotropy with KM3NeT using data frol 21 detection units ARCA21. This is a milestone result. Even though the dataset was still limited, the analysis shows that anisotropy measurements are still feasible using an underwater detector.
At the present stage, the analysis can be further improved in several directions. The limited statistics of the ARCA21 dataset constrain the robustness of the harmonic analysis. Moreover, subtle detector asymmetries and the sudden variation in the number of working PMTs require careful treatment to prevent artificial signals from contaminating the measurement. With increasing statistics and further investigations on these effects, future analysis will be able to refine the measurement, reduce systematic uncertainties and provide more precise estimate of the amplitude and phase of the dipole anisotropy. Looking ahead, the prospects are highly promising. As ARCA continues to expand, the number of detection units will steadily increase and with it the statistical power. Larger statistics will not only will not only enhance the significance of the large-scale dipole measurement, but will also open the door to the exploration of smaller angular scale fea-

tures providing complementary information to other cosmic-ray experiments. ARCA will become a powerful tool for probing the anisotropy in the arrival direction of high energy cosmic-rays. In parallel, KM3NeT/ARCA continues to fulfil its mission as a world leading neutrino observatory, already highlighted by the detection of the most energetic neutrino ever observed.